Lawrence Berkeley National Laboratory

Title
Evaluation of the performance of the oceanic hydrate accumulation at site NGHP-02-09 in the Krishna-Godavari Basin during a production test and during single and multi-well production scenarios

Permalink

Authors
Moridis, GJ
Reagan, MT
Queiruga, AF
et al.

Publication Date
2018

DOI

Peer reviewed

1

4

5   George J. Moridis[1,2], Matthew T. Reagan[1*], Alejandro F. Queiruga[1], and Ray Boswell[3]

6

7   [1]: *Energy Geosciences Division, Lawrence Berkeley National Laboratory, Berkeley, CA*
8   *94720, USA*
9   [2]: *Petroleum Engineering Department, Texas A&M University, College Station, TX*
10   *77843, USA*
11 [3]: *U.S. Department of Energy, National Energy Technology Laboratory, Pittsburgh PA*
12   *15236, USA*
13   **: Corresponding author.*

14

17**Abstract**

18The objective of this study is to quantify, by means of numerical simulation, the response
19of the complex system of gas hydrate accumulations at Site NGHP-02-09, Krishna-
20Godavari Basin, Indian Ocean, to different production conditions, and to determine the
21technical feasibility of gas production through depressurization-induced dissociation. The
22study assesses the suitability of the site for a long-term production test involving a single
23vertical well, and the long-term potential of the deposit under full-field production using
24a system of multiple vertical wells. We simulate gas and water flow, estimate the
25production performance of the accumulation and separately investigate the corresponding
26geomechanical response of the system. Results indicate that production from Site NGHP-
2702-09 under the conditions of a long-term field test involving a single vertical well is
28technically feasible and can yield high gas production rates. However, an inability to fully
29isolate the water bearing zones results in production that is largely from dissolved gas
30rather than hydrate dissociation and is thus burdened by excessive water production.
31Given the estimated physical properties of the reservoir system, Site NGHP-02-09 does
32not appear to be a promising location for a single-well field test of gas production, but
33may be a promising production target for full-field production operations using a multi-
34well system in which exterior wells can mitigate water inflows to allow interior wells to
35more effectively depressurize the formation and capture methane from gas hydrate
36dissociation. Geomechanical issues need to be carefully considered as significant
37displacements are possible, which can be challenging to well construction and stability.

38

39**1. Introduction**

40**1.1. Background**

41The present study focuses on the analysis of a particular oceanic hydrate accumulation in
42the Krishna-Godavari Basin (hereafter referred to as the KG Basin) off the eastern coast
43of India, and its evaluation as a potential energy source and a hydrocarbon gas production
44target. More specifically, the hydrate deposit under investigation is located at Site NGHP-
4502-09 in the KG Basin that was recently drilled and cored during the National Gas
46Hydrate Program Expedition 02 (NGHP-02) that was conducted from 3-March-2015 to
4728-July-2015 (Figure 1).

48The NGHP-02 expedition involved participation and support by a large international team
49representing several government and private organizations and included a wide range of
50investigations. NGHP-02 downhole logging, coring and formation pressure testing
51confirmed the presence of large, highly saturated, gas hydrate accumulations in coarse-
52grained sand-rich depositional systems throughout the KG Basin within the regions
53defined during NGHP-02 as Area-B, Area-C, and Area-E (Figure 1). The existence of a
54fully developed gas hydrate petroleum system was established in Area-C of the KG Basin
55with the discovery of a large slope-basin interconnected depositional system, including a
56sand-rich, gas-hydrate-bearing channel-levee prospect at Sites NGHP-02-08 and -09
57(*Collett et al., this issue*: Figure 2). The elevation (measured from the ocean surface) of
58the upper surface of a system of Hydrate-Bearing Sediments (HBS) in the vicinity of
59these sites is described in the contour plots of Figure 3. Further analysis of cores and
60geophysical data collected at these sites yielded important information on the system

61stratigraphy and hydrate occurrence, revealing a very complicated geology that involved

62a HBS sequence consisting of alternating layers of high-porosity hydrate bearing sandy

63layers, hydrate-free intervals of the same water-saturated sandy medium and mud/clay

64interlayers (Figure 4). Investigation of all available data showed that the gas hydrates at

65these sites have very desirable reservoir properties, i.e., high gas hydrate saturation S_H

66and high intrinsic and effective permeability (k and k_{rel}, respectively), making these

67accumulations ideal candidate sites for consideration of future gas hydrate production

68testing. The present study focuses its effort on Site NGHP-02-09.

69**1.2. Objectives**

70The objective of this study is to quantify, by means of numerical simulation, the response

71of the complex system of hydrate accumulations at Site NGHP-02-09 to different

72production conditions in an effort to determine: a) the technical feasibility of gas

73production through depressurization-induced dissociation, b) the suitability of the site for

74a production test of several months duration involving a single vertical well, and c) the

75long-term potential of the deposit as a hydrocarbon resource in a full-field production

76operation using a system of multiple vertical wells. The study predicts fluid (gas and

77water) flow and production performance of the accumulation through the analysis of the

78coupled flow, thermal and phase-change processes that occur during the course of

79production. These production estimates do not incorporate the effects of progressive

80reservoir compaction during depressurization. The corresponding geomechanical

81response of the geologic system is calculated separately, using one-way coupling to draw

82 inputs from the production model at certain moments in time to provide estimates of the

83 in situ stress fields, formation compaction and seafloor subsidence.

84

85 **1.3. Cases investigated in this study and general approach**

86 We investigated a total of 4 different cases that involved different geometries and

87 production scenarios. These were the following:

88 (1) The reference case, hereafter referred to as *Case R,* which describes production

89 from a radially infinite-acting (*open*) system using a single vertical well during a

90 long-term (about 180 days) field test. The infinite-acting nature of this system is

91 defined by radial boundaries located at a sufficiently large distance from the

92 single vertical well called by the test design that their conditions and properties

93 remain time-invariant during the test period. Through scoping calculations, we

94 determined that a cylindrical system with a radius $r = 2000$ m satisfies these

95 conditions. Case R is designed to address the issue of suitability of Site NGHP-

96 02-09 as the location for the planned long-term field test of gas production from

97 the hydrate accumulations of the KG Basin.

98 (2) *Case C1*, which describes production operations involving a system of vertical

99 wells on a regular grid. The effect of multiple wells on a regular pattern creates

100 conditions that approach no-flow boundaries of the drainage area of individual

101 wells in the *interior* of the pattern. Here we provide production estimates by

102 assuming no-flow boundaries exist, meaning we model a single interior well as a

103   closed system with no external source of fluid or heat. In Case C1, the distance

104   between wells is 1000 m, the radius of the domain (drainage area) of each interior

105   well is r = 500 m. Case C1 is designed to evaluate the potential of the hydrate

106   deposit at Site NGHP-02-09 as a target for full-field reservoir development

107   through multiple wells.

108   (3) *Cases C2* and *C3* are similar in concept to Case C1, from which they differ in the

109   domain radius (r = 100 m and 75 m, respectively). The reason for investigating

110   the three cases is to evaluate the effect of well spacing on the gas production

111   performance from the NGHP-02-09 hydrate deposits under multi-well production

112   operations.

113All the simulations were conducted using a single set of flow, thermal, and

114geomechanical properties as reported in companion papers in this Special Volume (*ex.,*

115*Yoneda et al., this issue-a,b; Waite et al., this issue*). Thus, the present study does not

116include a parametric sensitivity analysis of the system production performance and

117overall behavior in response to variations in the values of key flow, thermal and

118geomechanical conditions and properties and does not consider heterogeneity in any of

119these parameters. The enormous execution time requirements (hundreds of thousands of

120supercomputer hours and months of wall-clock time – see later discussion) needed to

121complete the study of the four cases using the standard set of properties and conditions

122precluded such an activity within the time frame of this study. As a result of the

123computational costs, it was infeasible to perform fully coupled simulations including

124geomechanics, and the geomechanical response was estimated by post-processing the

125results of the costly multiphase flow simulations.

126

127**2. System Description and Production Strategy**

128The discussion and analysis in this section is based on the data provided by the entire

129multinational team involved in the NGHP-02 scientific expedition and the subsequent

130study (as summarized in *Collett et al., this issue; Boswell et al., this issue; Kumar et al.,*

131*this issue*). The methods used for the measurement and derivation of these data—and in

132the estimation of the relevant parameters, where direct measurements were not possible—

133are beyond the scope of this study and are not discussed in detail. Although a very large

134number of data were obtained in the course of the NGHP-02 expedition and the

135subsequent associated work, in the present modeling study we include and discuss only

136the data used in the simulations. The interested reader is directed to other relevant papers

137associated with the NGHP-02 expedition.

138**2.1. System description and geometry**

139The water depth at Site NGHP-02-09 of the KG Basin (see Figure 5) is 2,219.5 m. The

140available information at the time of the study indicated that the hydrate accumulation at a

141promising location at that site is buried under a relatively thin layer of 214.9 m of mud

142below the sea floor (Figures 3, 4, and 5). The complex, 53.6 m-thick system of the HBS

143sequence is characterized by 49 alternating layers of (a) hydrate-rich sands, (b) clays

144(muds) that are nearly devoid of hydrates, and (c) hydrate-free sands. Figure 5 shows a

145sketch of this system (based on the most recent data), and provides some basic

146information on the geology and geometry of the system such as the stratification, the

147thickness of the various layers and the texture of the corresponding sediments. The base

148of the gas hydrate stability zone (BGHSZ) is estimated to be well below the base of the

149hydrate accumulation, i.e., this is a thermodynamically stable system.

150This complex, 53.6 m-thick hydrate-bearing system is overlain and underlain by very

151low-permeability boundaries, i.e., the mud overburden and assumed underburden,

152respectively (Figure 5). Based on experience gained in earlier studies (Moridis and

153Reagan, 2007a,b; Moridis et al., 2007; 2009a; 2013) and preliminary scoping

154calculations, the simulation domain extends from the ocean floor (the upper boundary of

155the domain) to a depth of 600 mbsf (Figure 5). This was necessary because the

156consideration of coupled flow, thermal, chemical and the one-way coupling to the

157geomechanical processes in this numerical study have effects that extend beyond the

158narrow confines of the hydrate-bearing sediments. The resulting dimensions of the

159simulation domain provided a representative reservoir description that (a) allowed heat

160and fluid exchanges between the deposit and its boundaries during the production period

161and (b) were shown to be sufficiently large to act as true boundaries for all processes

162considered in this study.

163**2.2. Classification of the hydrate deposit at Site NGHP-02-09**

164The analysis here hews very close to that of Moridis et al. (2013). Based on the geology

165and stratification indicated by Figure 5, the layered structure of the hydrate accumulation

166at Site NGHP-02-09 appears to be a combination of Class 2 and 3 systems, but can be

167better considered a hybrid of two hydrate classes (Moridis and Reagan, 2007a; 2007b

168Moridis et al., 2011; 2013): (a) Class 2, comprising a hydrate-bearing layer (HBL)

169overlying a zone of mobile water, and (b) Class 3, involving HBLs confined between two

170strata of near-zero permeability. Near the top of the HBL sequence, the features of a

171typical Class 2 deposit are dominant because of alternating HBL and hydrate free sands.

172The same can be said about the deeper mud interlayers (Figure 5), which are not

173impermeable. However, because of the very low permeability of the muds in the

174overburden, underburden and in the interlayers, the characteristics of a near-Class 3

175deposit are evident toward the bottom of the 53.6 m-thick system. Note that, although the

176water mobility in the mud layers is limited, it is not zero, and this has implications in the

177course of production that will be discussed later.

178**2.3. Method of production and well design**

179Gas production necessitates hydrate dissociation. Because of the geology at Site NGHP-

18002-09 (involving the low-permeability overburden, underburden and 14 mud layers in

181contact with HBLs), depressurization is the most effective dissociation strategy for

182reasons explained in detail by Moridis and Reagan (2007a) and Moridis et al. (2009b).

183This is accomplished by constant-pressure production (involving a constant bottomhole

184pressure P_w at the well), which is desirable because of its simplicity, its technical and

185economic effectiveness, the fast response of hydrates to the rapidly propagating pressure

186wave, the near-incompressibility of water, and the large heat capacity of water. Because

187of the high initial hydrate saturation S_H in the HBL and the very low permeability of the

188muds in the interlayers, the effective permeability k_{eff} at the onset of gas production can

189be very low, and constant-rate production is impractical because the associated pressure

190drop is rapid, large, and very difficult to control, with a near certainty of ice formation

191and severe restriction (or even blockage) of flow to the well. On the other hand, pure

192thermal stimulation is an unattractive option because of its limited and ever decreasing

193effectiveness and efficiency (Moridis and Reagan, 2007a).

194The use of horizontal wells was deemed impractical for the planned long-term field

195production test in the KG Basin due to the presence of alternating layers of highly

196permeable hydrate-free sand lenses and low intrinsic permeability mud interlayers, and

197the considerable cumulative thickness of the three types of units. Thus, vertical wells

198were used exclusively in the study. The simple well design uses a perforated interval that

199covers the entire 53.6 m-thickness of the hydrate-bearing interval. Alternative well

200completions were investigated and rejected that will be discussed later. A significant

201advantage of constant-P_w production is the elimination of the possibility of ice formation

202(with its consequent detrimental effects on permeability and gas production) through the

203selection of an appropriate $P_w > P_Q$ (where P_Q is the quadruple point pressure, 2.56 MPa).

204The use of vertical wells and the absence of any information on heterogeneity at the site

205(in particular) and in the KG Basin (in general) led to the use of a cylindrical domain in

206(r,z) that can be modeled as a 2D axisymmetric problem. In all studies, the well was

207located at $r = 0$ with radius $r_w = 0.1$ m. For the various cases of production we

208investigated, scoping calculations indicated that the domain radii and a total thickness of

209$\Delta z = 600$ m were sufficient to provide constant condition boundaries by confirming that

210the pressure, thermal and geomechanical disturbance caused by the bottomhole pressure

211did not reach these boundaries for the duration of the study period.

212

213**3. The Numerical Models and Simulation Approach**

214**3.1. Numerical methodology and codes**

215The simulations are performed using the TOUGH+Millstone suite, comprised of the

216integral finite difference method simulator TOUGH+HYDRATE and the finite element

217method simulator Millstone. The TOUGH+HYDRATE code (T+H) can model all the

218known processes involved in the system response of natural CH_4-hydrates in complex

219geologic media (Moridis et al., 2014; Moridis and Pruess, 2014). T+H is a fully

220compositional simulator, descended directly from the TOUGH2 family of codes (Pruess

221et al., 1999; Pruess, 2003), and it accounts for heat and up to four mass components (i.e.,

222H_2O, CH_4, CH_4-hydrate, and water-soluble inhibitors such as salts) that are partitioned

223among four possible phases (gas, aqueous liquid, ice, and hydrate). It can describe 15

224possible thermodynamic states (phase combinations) of the CH_4+H_2O system and can

225handle the phase changes, state transitions, strong nonlinearities and sharp fronts that are

226typical of hydrate dissociation problems. Because of the very large computational

227requirements that are the norm in hydrate problems, both a serial and a parallel version

228(Zhang et al., 2008) of the code were used in this study. The T+H code has been used for

229a wide range of investigations of gas production from hydrates in both oceanic deposits

230and in accumulations associated with the permafrost that cover the entire spectrum of

231hydrate types, i.e., Class 1 (Moridis et al., 2007), Class 2 (Moridis and Reagan, 2007b;

232Moridis et al., 2011a; 2011b), Class 3 (Moridis and Reagan, 2007a; Moridis et al.,

2332011c), and Class 4 (Moridis and Sloan, 2007; Li et al., 2010; Moridis et al., 2011d). In

234addition, the code has been used extensively to model natural hydrates and environmental

235impacts (Thatcher et al., 2013; Marin-Moreno et al., 2015; Stranne et al., 2016). For this

236study, we activated 3 components, 4 phases, and 4 equations to model systems containing

237water, methane, and salt partitioned over gas, liquid, hydrate, and ice phases.

238Geomechanical analysis of the new set of hydrate reservoirs is enabled by a new

239geomechanical simulation framework, Millstone (Moridis et al., 2017). Millstone solves

240the incremental stress formulation using the Finite Element Method with the standard

241Galerkin formulation with bilinear-quad nodal shape functions for displacement fields

242and Gauss point-centered stresses. A small-deformation linearized strain assumption is

243used at each increment, with elastic moduli that are functions of the flow variables. This

244code introduces two new key features: (1) use of a separate mesh for the mechanical

245solution, alleviating the frequent problem of the ill-conditioned linear systems; and, (2)

246formulations for plane-strain and axisymmetry using 2D elements (in addition to standard

2473D Cartesian formulations). The Millstone code yields significant speed improvements

248by reducing system unknowns and improving the stability, conditioning and accuracy of

249the solution compared to earlier used geomechanical solvers based upon 3D formulations

250using one-volume-to-one-element coupling schemes. Millstone is typically operated

251embedded inside of the TOUGH+Hydrate simulation loop, wherein it solves the

252quasistatic balance of momentum inside of the nonlinear solution loop of the flow solver.

253The solver iterates between solving displacements and flow primary variables,

254performing interpolations of required fields back-and-forth between the two meshes, until

255convergence for each time step.

256The computational cost of the highly-detailed system precluded the use of the complete

257two-way coupling between the flow and geomechanics, in which both systems are solved

258at every step of the Jacobian system until convergence. Beyond adding more unknowns,

259the inclusion of geomechanics in a coupled simulation greatly increases the cost by both

260increasing the number of iterations per time step (the staggered scheme does not have

261quadratic convergence) and decreasing the size of viable time steps due to the increased

262difficulty of solving the nonlinear equations. A time step sequential scheme, in which the

263geomechanics is solved only once per time step, performs worse due to smaller time step

264requirements.

265Motivated by this problem, a two-stage simulation process was developed to estimate the

266geomechanical response with only one-way coupling. The time-varying pressure and

267saturation fields at snapshots from the flow simulation are used to solve the total stress

268and displacements. The complete analysis procedure has four stages:

2691. Preprocessing to generate meshes and input files,

2702. Running TOUGH+Hydrate on HPC resources to solve multiphase, multicomponent

271   flow,

2723. Running Millstone on workstation to solve displacements and stresses resulting from

273   depressurization and hydrate dissociation, and

2744. Postprocessing to calculate additional quantities of interest and generate plotting and

275   visualization formats.

276In this methodology, there is no feedback from the stress distributions to the flow

277problem, and as a result, the production values do not reflect potential reduction in

278production rates due to progressive reservoir consolidation (see Boswell et al.-b, this

279issue). The solution of the mechanics is linear and quasistatic in absence of the flow

280effects, and thus each case can be solved in only ten minutes on a desktop workstation

281given the flow fields to provide the estimates presented here. The open source

282tough_convert post-processing utility (Queiruga, 2018) is used in a standalone script for

283the Millstone simulator in this system.

284A saturation dependent poroelastic constitutive response is used. The stress update is

285linear elastic with respect to the displacements, and the bulk and shear modulus depend

286on the hydrate saturation linearly by the relations $K(S)=K_0 S+K_1(1-S)$ and

287 $G(S)=G_0 S+G_1(1-S)$ (Rutqvist and Moridis, 2009). The values K_0 and G_0

288correspond to the hydrate-free moduli of the sediments, and K_1 and G_1 are

289calculated based on the *in situ* saturation and field-determined elastic moduli. Plastic

290yielding is not included in the stress integration, but the value of the Drucker-Prager yield

291criteria is calculated as an estimate of possible geoemechanical failure.

292**3.2. Domain dimensions and discretization**

293Very fine grids were used in the simulation of production from the vertical well in all

294cases of this study. The 2D cylindrical (axisymmetric) domains of the single vertical well

295problems in the four cases were discretized as follows:

296 ● Case R (Reference, r = 2000 m): 452 x 525 in (r,z) = 2.37×10^5 gridblocks

297 ● Case C1 (r = 500 m): 351 x 525 in (r,z) = 1.84×10^5 gridblocks

298 ● Case C2 (r = 100 m): 239 x 525 in (r,z) = 1.25×10^5 gridblocks

299 ● Case C3 (r = 75 m): 219 x 525 in (r,z) = 1.15×10^5 gridblocks

300 The meshes are aligned with the *r-z* axes. Drawing on past experience, the discretization 301 along the z-axis within the 53.6 m of the HBS sequence had a maximum subdivision size 302 Δz = 0.1 m, and ensured that each layer was subdivided in at least 3 segments regardless 303 of the layer thickness (thus providing sufficient description of thermal gradients, and of 304 heat and fluid flows). The same fine discretization along the z-axis was maintained in the 305 first few subdivisions of the overburden and the underburden in contact with the HBS 306 sequence (necessary to describe fluid and heat exchanges between the hydrate-bearing 307 system and its boundaries during the endothermic dissociation process that feeds gas 308 production). The discretization was non-uniform (with Δz increasing) in the mud of the 309 overburden and underburden away from the top and bottom hydrate interfaces, i.e., near 310 the top and bottom of the domain.

311 Particular emphasis was given to fine discretization in the first 50 m along the r-axis, with 312 0.1 m radial subdivisions to 5 m, then linearly increasing Δr to 0.5 m at 50 m. 313 Discretization past that point in the *x*- and *y*-directions was non-uniform, increasing 314 logarithmically using a starting value of Δr = 0.5 m to 2,000 m (452 elements total). Past 315 experience has indicated that such fine discretizations are necessary when steep thermal 316 and pressure gradients are involved (Moridis et al., 2007). This high degree of refinement 317 provided the level of detail needed to capture important processes near the wellbore and

318in the entire hydrate-bearing zone, and especially in the thin interlayers that characterize

319the NGHP-02-09 systems.

320Treating hydrate dissociation as an equilibrium reaction (Kowalsky and Moridis, 2007)

321and accounting for the effect of the salinity on hydrate dissociation, resulted in a system

322of about 9.48×10^5, 7.36×10^5, 5.0×10^5 and 4.6×10^5 equations for Cases R, C1, C2, and C3,

323respectively. The size of the problem precluded the use of desktop computational

324platforms (except for scoping calculations) and necessitated the use of the parallel version

325of T+H (pT+H) and high-performance computing resources. The full two-way coupling

326between flow and geomechanics was intractable as the coupled simulation requires a

327smaller timestep size and more iterations per timestep. The complexity of the geology of

328the system and of the coupled processes involved were so extreme that the flow

329simulations alone required between 900,000 to 2,000,000 timesteps (total) to cover the

330study periods of the various cases, and required hundreds of thousands of CPU-hours.

331The resources of LBNL Lawrencium cluster farm were used to perform the pT+H

332simulations in this paper using 256 to 1,024 cores per submission.

333The dual-mesh algorithm enables a coarser mesh to be used for the geomechanical

334response, where Millstone automatically handles the interpolation between the structured

335finite difference grid and unstructured finite element mesh. The final geomechanical

336results were solved on an unstructured quadrilateral mesh with 48,954 nodes and 48,777

337elements, resulting in a system of 97,908 equations for displacement updates and 195,108

338additional stress degrees of freedom. The mesh was structured near the well in the

339hydrate bearing layer with square elements of side length of approximately 0.25 m to

340capture the fine scale deformation. The post-processing-based one-way coupling

341algorithm allowed the geomechanical results to be calculated in approximately ten

342minutes for each case, for which only considering the one-way effects allowed us to only

343use 20 intermediate snapshots to compute the quasi-static deformation path.

 344

345**3.3. Baseline system properties and well description**

346Key baseline hydraulic and thermal properties of the various geological media in the

347various layers of the geologic model in Figure 5 were provided from studies conducted

348by other members of the NGHP-02 expedition and are listed in Table 1. The

349corresponding geomechanical properties are listed in Table 2. These values were used in

350the simulation of all four cases. In the absence of relevant information, the relative

351permeability and capillary pressure relationships and corresponding parameters were

352approximations based on similarly textured media or calculated from estimated effective

353permeabilities. Note the relatively low thermal conductivity values measured from

354samples from Site NGHP-02-09. A possible explanation for the low values was the

355"watery" texture of the samples, as indicated by their very high porosity. Reasonable

356specific heat values were used for all the geologic media because data from direct

357measurements were unavailable.

358The same layer geometry is applied to the finite element mesh for the geomechanical

359properties. In this study, material is modeled using a rate-based formulation that does not

360consider plastic behavior. We considered two material groups: a sandy (hydrate-bearing

361or hydrate-free) medium, and a clay (mud) medium of the overburden, underburden and

362of the interlayers between the sandy HBS. The relevant geomechanical properties

363(Young's modulus, Poisson's ratio, and skeletal grain density for each medium) are listed

364in Table 2. We used values of the Young's modulus that are linear functions

365(interpolations) of S_H in the hydrate-bearing media. Based on Rutqvist and Moridis

366(2009) and Rutqvist et al. (2009), a constant Poisson's ratio was used, and the Biot

367coefficient was $b = 0.99$.

368Based on earlier studies that confirmed the validity of the approach (Moridis and Reagan,

3692007a,b; Liu et al., 2017), we approximated wellbore flow by Darcian flow through a

370pseudo-porous medium describing the interior of the well. This pseudo-medium had $\varphi =$

3711, a very high $k = 5 \times 10^{-9}$ m^2 (= 5,000 Darcies), a capillary pressure $P_c = 0$, a relative

372permeability that was a linear function of the phase saturations in the wellbore, and a low

373(but nonzero) irreducible gas saturation $S_{irG} = 0.005$ to allow for the emergence of a free

374gas phase in the well. While discretely treating the wellbore is required to solve the flow,

375the structure is neglected in the mechanical analysis and the coarser size of the mesh

376elements extends to the center axis of the domain, using only the mechanical properties

377of the sediments.

378**3.4. Initial and boundary conditions**

379We determined the initial conditions in the reservoir by following the initialization

380process described by Moridis and Reagan (2007a,b). Based on initial measurements at the

381site, the geothermal gradient at the site was $dT/dz = 5.82$ °C/100 meter with a seafloor

382temperature of $T = 3.46$ °C (later updated—see *Waite et al. this issue*). The uppermost and

383lowermost gridblock layers (i.e., at the top of the overburden at the ocean floor, and at the

384bottom of the simulated domain) were treated as constant-condition boundaries

385(maintaining constant P and T). Knowing that a) the pressure P = 25.45 MPa at the ocean

386floor and b) the pressure distribution with depth was hydrostatic (as is almost universally

387the case in hydrate accumulations), we determined the pressure P_T using the P, T- and

388salinity-adjusted water density. Then, using P_T and the boundary temperatures T_T and T_B,

389the hydrostatic gradient and representative thermal conductivity values, we determined

390the vertical P- and T-profiles in the domains by means of a 1-D column simulation.

391The numerical representation of a constant bottomhole pressure P_w involves imposing a

392constant P_w at the topmost element of the well in the manner used to impose other

393constant-condition boundaries. In our study, the system behavior and performance was

394evaluated at a single value of P_w (= 3.0 MPa). Based on the results of the Moridis et al.

395(2014) study, this bottomhole pressure was the most desirable (although not necessarily

396practical or attainable under the conditions of the Site NGHP-02-09 deposit), and useful

397in providing the upper estimate of production. This P_w value is larger than the CH_4-

398hydrate quadruple point pressure P_Q = 2.56 MPa, eliminating the possibility of ice

399formation and the corresponding adverse effect on k_{eff}, flow and production.

400The boundary conditions of the geomechanical system include an assumption of no-

401horizontal displacement at both sides along the r-axis, and a no-vertical displacement

402boundary at the bottom. The overburden pressure (at the top of the first HBL) is set at

40327.70 MPa. The initial stress state of the geomechanical system is determined by solving

404for a set of discarded displacements that solve the static equilibrium of the domain given

405the mechanical loading conditions, the spatially-variably material properties, and the

406initial fluid pressures and saturations used for the flow simulation.

407

408**4. Results and Discussion**

409**4.1. Production performance in the reference Case R**

410Figure 6 shows the expected evolution of the hydrate dissociation (overall rate of gas

411release into the reservoir from hydrate dissociation) rate Q_D and of the gas production rate

412at the well, Q_P, as a result of the depressurization caused by the operation of a single

413vertical well at the center of the cylindrical infinite-acting domain. Although Q_P rises

414very fast to a high level (exceeding 5 MMSCFD in less than a month), even a cursory

415inspection of Figure 6 reveals a problem: Q_D is substantially smaller than Q_P, throughout

416the period of the test, indicating that hydrate dissociation is not the dominant source of

417the produced gas in this timeframe. Hydrate deposits that are promising targets for

418production are characterized by Q_D exceeding Q_P early in the production period, and their

419desirability increases with an increasing gap between the two. In the absence of free gas

420zones in the system, the only possible alternative source of gas is exsolution of CH_4

421dissolved in the aqueous phase of the deposit. Given the very small solubility of CH_4 in

422H_2O, this indicates that very large amounts of H_2O need to be produced to provide the

423significant level of Q_P estimated by the simulation, raising significant questions about the

424viability of such an endeavor. The semi-log plot in Figure 7 shows the same Q_D and Q_P

425results, but focused on the early-time behavior. It shows net hydrate formation (denoted

426by the negative Q_D values) in the reservoir for the first 20 days of production. This means

427that CH_4 dissolved in the aqueous phase forms hydrate on the way to the well at a rate

428that exceeds the hydrate dissociation at elsewhere in the reservoir. An even more

429worrisome feature in Figures 6 and 7 is the declining trend in Q_D as time advances: this is

430the opposite of what would be expected in a desirable production target and is an

431indication of ineffective depressurization.

432Review of the composition of the produced fluids in Figure 8 provides further evidence

433of the problem with this production test: gas dissolved in the produced water amounts to

434almost 50% of the total methane produced at the well. This means a very large water

435production rate is needed to achieve the rate of methane production predicted by the

436simulation. The cumulative volumes of methane produced and hydrate-originating

437methane in the reservoir (V_D and V_P, respectively) in Figure 9 depict clearly the

438increasing discrepancy between hydrate dissociation and gas production at the well (with

439$V_D << V_P$). Further evidence of the challenges facing a long-term production test at Site

440NGHP-02-09 is provided by the free gas volume V_F in Figure 10, which reaches a plateau

441within 50 days from the onset of production, and actually appears to decline slowly after

442this time (hinting at the possibility of secondary hydrate formation capturing free gas

443within the reservoir). Hydrate deposits that are desirable production targets are

444characterized by an increasing V_F over time (at least until a large part of the resource is

445exhausted) that acts as the primary source of gas for production. The inability of V_F to

446increase with time (in addition to the low Q_D) is further evidence of ineffective

447depressurization.

448The water production results (Q_W and M_W) in Figure 11 confirm these problems and

449indicate the significant technical and economic challenge of moving the very large and

450increasing volumes of H_2O that are necessary to maintain the depressurization needed to

451support the production rate Q_P, mainly through transport of aqueous CH_4 in the produced

452water. The high level of Q_W and its non-declining (actually increasing) value with time

453even after t > 180 days is an indication of continuous inflow of H_2O from the boundaries.

454The water-to-gas ratio (WGR), $R_{WG} = M_W/V_P$, and the salt mass fraction X_S in the

455produced water (Figure 12) confirm the earlier observations, deductions and conclusions.

456WGR appears practically constant over time at a very high level (about 170 kg of H_2O

457per standard m^3 of CH_4) that is economically unsustainable and technically challenging

458(although perhaps feasible). The high and persistent WGR level during the duration of the

459test period is an additional indication of continuous inflow of H_2O from the boundaries.

460The evolution of X_S over time provides further support to the initial Q_D behavior—its

461value exceeding the natural salinity of ocean water (0.035) is a clear evidence and

462confirmation of the net hydrate formation identified in Figure 7, as hydrate formation in

463saline water results in localized salinity increases as the hydrate crystal does not admit

464salt. The fact that X_S remains above the 0.035 level indicates a combination of limited

465hydrate dissociation, hydrate formation at other locations, and inflow of ocean water from

466the boundaries, all of which point toward ineffective depressurization.

467

468**4.2. Spatial distributions of important parameters in the reference Case R**

469The pressure distributions in Figure 13 provide direct evidence of the indications of

470ineffective depressurization surmised from the analysis of the figures in Section 4.1.

471Thus, there appears to be practically no change in the P-distribution past $t \geq 56$ days.

472Note the relatively thin depressurization zone, indicative of a higher effective

473permeability compared to its adjacent units. The depressurization band, however, does

474not expand beyond the range seen at $t = 17$ days, thus further supporting the conclusion

475of ineffective depressurization. As expected, the largest pressure drop in the domain

476(depicted by the yellow-blue range of color) occurs close to the vertical well at $r = 0$ and

477corresponds to hydrate dissociation there.

478The T-distributions in Figure 14 are different in pattern than the P-distributions in Figure

47913, but it is these differences that confirm the observations and conclusions drawn from

480the P-profile analysis and from the earlier results. At $t = 17$ days, there is a narrow band

481of lower temperature in the upper part of the HBS sequence (within layers 1 through 28

482as shown on Figure 5), which indicates cooling caused by active hydrate dissociation.

483However, this temperature disturbance is attenuated at $t = 56$ days, and practically

484disappears after that time. This is an indication of water inflows from the infinite-acting

485radial boundaries, which counters the initial cooling and at the same time provides the

486pressure support observed in Figure 13. The limited dissociation discussed in Case R is

487further indicated by the absence of any noticeable change in the T-distributions for $t > 56$

488days.

489The evolution of the S_H and S_G distributions are shown in Figures 15 and 16, respectively.

490The hydrate saturation appears practically unchanged after $t \geq 56$ days, as does the

491distribution of gas, S_G. The limited occurrence of free gas (derived from dissociation) is

492consistent with the V_F results of Figure 10 and confirms both the observations of limited

493dissociation and its stagnation as time advances. In addition to poor dissociation

494performance, some localized formation of hydrate occurs in the uppermost layers,

495resulting in hydrate saturations that exceed the initial saturation (indicated by arrows in

496Figure 15). Further proof is provided by the X_S distribution in the aqueous phase that is

497shown in Figure 17: the absence of significant freshening of the water and the limited

498footprint of the areas where X_S is different from the background level are consistent with

499limited (or non-occurring) dissociation, and is in agreement with all previous

500observations.

501Figure 18 describes the pressure profile inside the well (i.e., along z at $r = 0$) and provides

502clear evidence of the culprit for the ineffectiveness of depressurization and the

503consequent limited hydrate dissociation. Although there is no resistance to flow within

504the well casing (being in essence an "infinite permeability" system, leading to an

505expectation of a near-linear pressure decline in the well), there is no significant pressure

506drop at any time below about $z = -241$ m. The obvious inference is that there is a source

507of water at and above this level that can easily replenish the water produced by the well,

508thus preventing any pressure drop below this point. This source of water is the hydrate-

509free sandy layers Aqu01 through Aqu10 (see Figure 5), which have very high

510permeability (on the order of $k_r = 10^{-11}$ m^2 = 10 D, Yoneda et al. (this issue-b)), thus

511having enough capacity to resupply all the water withdrawn by the well and preventing a

512pressure drop below the $z = -241$ m (with Aqu10, at $z = -248$ m and with a thickness of

513nearly 7 m, capable of contributing significant flows) . In addition, the low-permeability

514layers Mud01 through Mud05 (-230 m < z < -226 m) separate the upper hydrate and

515aquifer layers and are reflected by the near step-change in pressure within the reservoir

516below -226 m seen in Figure 13. Consequently, effective depressurization is not possible

517below this level.

5184.3. Conclusions drawn from the production performance in Case R

519The results of the study indicate that gas production from Site NGHP-02-09 under the

520conditions of a long-term field test involving a single vertical well is technically feasible

521and can yield high gas production rates. However, the high gas production is based

522mainly on exsolution of dissolved gas rather than hydrate dissociation and thus

523necessitates excessively large water production, the management of which appears to be a

524technical challenge.

525The conclusion from this analysis is that Site NGHP-02-09 is not a promising location for

526a field test of gas production from the hydrate deposits of the KG Basin. Despite

527encouraging conditions (high permeability and hydrate saturation) and ample hydrate

528resources at the site (with a combined thickness of HBLs in excess of 36 m and an

529excellent permeability regime of these units), the presence and attributes of the hydrate-

530free and extremely permeable aquifer layers are sufficient to singlehandedly short-circuit

531the depressurization process and preclude the consideration of Site NGHP-02-09 as a

532possible test location. In essence, such a test would be a demonstration of production

533more of exsolution of dissolved gas rather than of dissociation of hydrates. Note that

534attempts to isolate the Aqu10 layer by modifying the location of the perforated interval of

535the well (e.g., confining it to intervals above and below this layer) in several scoping

536simulations had no practical effect, with production behavior very similar to that of the

537fully perforated HBS sequence as there are still many sources of water inflow.

538**4.4. Production performance in Cases C1, C2 and C3**

539The importance of the assumed no-flow radial boundaries in Cases C1, C2 and C3 is

540amply demonstrated by the evolution of the corresponding gas release rates Q_D in Figure

54119, which also includes the Q_D for Case R for comparison. The differences in both pattern

542and performance are notable. In all three cases, we observe an early surge of gas release

543at rates that are between 3 and 3.3 m^3/s (9 and 10 MMSCFD) and are caused by the large

544initial driving force of depressurization, i.e., the difference ΔP between the bottomhole

545and the reservoir pressure in the vicinity of the well that is at its maximum at the

546beginning of production. Because the Aqu10 unit is now unable to function as a

547practically infinite source of water, depressurization is effective and leads to the large

548initial Q_D that occurs almost immediately after the onset of production in the limited

549volumes of the domains in Cases C2 and C3. In this first gas release, Q_D is higher for the

550cases with reduced domain volumes because of stronger response to depressurization,

551although the lack of enhancement from Case C2 to C3 suggests there is a practical limit

552to tighter well spacing. The response in the larger-volume domain of Case C1 is slower

553because of the correspondingly larger mass of water in the Aqu10 unit. This is the reason

554why the Q_D for Cases R and C1 initially coincide, with the point of deviation at about $t =$

55520 days marking the first effect of the closed boundaries.

556The initial spike in Q_D is followed by longer periods of large Q_D that peak at similar

557levels of about 3 MMSCFD for Cases C2 and C3, but are larger (peaking at about 4 m^3/s

558or 12 MMSCFD by t = 300 d) in the larger system of Case C1. In this second gas release,

559Q_D increases with an increasing domain volume because of an increasing mass of

560dissociating hydrate. Although the driving force difference ΔP is smaller, the effect of

561dewatering of the system leads to an effective depressurization of the hydrate over a large

562volume of the reservoir, significant dissociation and gas release. The peak in this second

563phase of hydrate dissociation is followed by a continuous decline in Q_D that is attributed

564to the reduction in the reservoir temperature (caused by the endothermic nature of

565dissociation, which inhibits dissociation) and in the driving force of dissociation, i.e., the

566difference between wellbore and reservoir P). The same behavior is more evident in

567Cases C2 and C3.

568The evolution of the gas production rate Q_P in cases C1, C2, and C3 (Figure 20) follows a

569similar pattern as Q_D, and differs substantially from that in Case R in terms of pattern,

570magnitude and relationship to Q_D. Q_P also exhibits the two-lobe pattern of Q_D in the C1,

571C2, and C3 cases (Figure 20), with similar relationships of the relative magnitudes

572between the cases. Thus, the first surge of production peaks at about Q_P = 4.5, 6, and 6.5

573MMSCFD in Cases C1, C2, and C3, respectively. The second (long term) surge of

574production peaks at about Q_P = 8, 3.5, and 3 MMSCFD in Cases C1, C2, and C3,

575respectively. The effective hydrate dissociation in these closed systems is demonstrated in

576the analysis of the origin of gas in Cases C1 and C3 (Figure 21), which now shows a far

577smaller contribution to Q_P from methane dissolved in the produced water than in Case R.

578Both the Q_P and Q_D results are positive indicators of the potential of the site as a target for

579multi-well production rather than as a test site. Note that these enhancements assume a

580degree of uniformity across the larger multi-well reservoir system and that these results

581reflect the performance of *inner wells* shielded from water inflow by outer wells in the

582pattern. Interference between wells due to unknown pathways or heterogeneities in

583hydrate dissociation could reduce the effectiveness of a multi-well pattern.

584The cumulative volumes of produced gas V_P in Figure 22 indicate (a) similar initial

585production in all closed-system cases, with deviations marking the beginning of

586exhaustion of the different hydrate masses (or severe reduction in dissociation) in the 3

587systems, and (b) V_P that are consistently lower than that for Case R during the initial 200

588days of the simulation. The evolution of free gas volume V_F in the three domains (Figure

58923) also shows a striking difference from that in Case R and explains some of the V_P

590observations: V_F are now much larger by orders of magnitude, as released gas is stored in

591the reservoir, and is used as a source of gas for production. The severe reduction in

592hydrate dissociation (attributed to the causes discussed earlier) is evident in Cases 2 and

5933, but has not yet begun during the production period in the larger system of Case 1. As

594expected, both V_P and V_F increase with an increased volume of the closed domain of the

595cases.

596The evolution of water production (rates Q_W and cumulative mass M_W in Figures 24 and

59725, respectively) shows the clear production superiority of closed systems compared to

598Case R. Following an initial surge of very short duration, Q_W decreases continuously in

599all three cases (in contrast to the increasing Q_W in Case R), leading to M_W that are much

600smaller than those in Case R and posing a much easier water management problem that

601becomes easier as the reservoir volume corresponding to each well in the closed systems

602decreases. Thus, the attractiveness of the larger V_P in Case R is negated by the much

603larger M_w, but Cases C1, C2, and C3 emerge as possible production options. This is

604further confirmed by the WGR in Figure 26, which indicates a generally improving gas

605vs. water regime in all three closed-system cases, and is consistent with promising

606production targets. Note the slight increase in the WGR for Cases 2 and 3 at late times,

607which is attributed to water inflows from the top (overburden and ocean floor) and

608bottom (deep subsurface) boundaries that are enhanced by the depressurized interior of

609the reservoir. This is confirmed by the pattern of X_S evolution in Figure 27, which

610exhibits the effect of active hydrate dissociation in the initial X_S decline (water

611*freshening*) that is caused by the release of salt free water from the hydrate dissociation.

612The X_S decline is faster where hydrate dissociation is at its most intense, i.e., it is

613enhanced in decreasing system volumes. However, in the smaller volumes of Cases 2 and

6143, there is a pattern reversal and an increase in X_S for $t > 300$ days (when hydrate

615dissociation is at its minimum and the system pressure is at its lowest), which is an

616indication of saline water inflows, as well as of hydrate regeneration in the reservoir.

617**4.5. Spatial distributions of important parameters in the Cases C1, C2, and C3**

618In Case C1, the pressure distributions in Figure 28 clearly indicate a more effective

619depressurization than in Case R. The thin band identified in Figure 13 is clearly

620discernible initially, but the lack of inflows from the radial boundaries results in pressure

621drops over the entire reservoir depth interval that, as expected, continuously expand

622radially with time and are a positive indicator of production potential. The effective

623depressurization and its positive impact on hydrate dissociation in Case C1 is further

624demonstrated in the evolution of the *T*-distribution of Figure 29, which shows a

625continuous cooling of the system beyond the immediate wellbore and is another indicator

626of occurrence of the endothermic process of hydrate dissociation. Further confirmation of

627the enhanced hydrate dissociation in Case C1 (compared to that in Case R) is provided by

628the evolution of the S_H, S_G and X_S spatial distributions in Figures 30, 31 and 32,

629respectively. The footprint/occurrence of S_H indicates a continuously shrinking hydrate

630mass, which is by no means near exhaustion at the end of the 360-day production period.

631However, some localized hydrate reformation (indicated by arrows) still occurs, with

632local $S_H > S_{H,initial}$. This is accompanied by ever-expanding footprints of increasing S_G and

633decreasing X_S in the reservoir, as well as by increasing S_G and decreasing X_S levels,

634providing direct evidence of enhanced dissociation.

635In Case C2, the system behavior is similar to that in Case C1, but far more intense. Thus,

636the pressure distributions in Figure 33 indicate a continuous and an even more effective

637depressurization, as depicted by larger pressure drops over a larger system volume.

638Similarly, the evolution of the T-distribution in Figure 34 shows a continuous and faster

639(than in case C1) cooling of the system that affects a larger portion of the system volume,

640and is an indicator of intense hydrate dissociation. Further confirmation of intense

641hydrate dissociation in Case C2 (compared to that in Cases R and C1) is provided by the

642evolution of the S_H, S_G, and X_S spatial distributions in Figures 35, 36 and 37, respectively.

643The footprint/occurrence of S_H indicates a continuously shrinking hydrate mass.

644However, given the production behavior discussed in the previous section, there is no

645indication of hydrate exhaustion (only of mass reduction) at the end of the 540-day

646production period. This explains the production behavior and eliminates the possibility of

647exhaustion of hydrate as a possible reason for the near-cessation of dissociation and the

648consequent severe reduction in production at later times.

649This explanation can be further strengthened by an inspection of the spatial distributions

650in Figures 33 to 37, in addition to a re-evaluation of the production results. Once again,

651closer inspection of the S_H distribution at $t = 540$ days indicates localized increases in S_H

652(arrows). The S_G distribution indicates gas exhaustion, as indicated by the reduction in the

653S_G levels at t = 540 days, and is consistent with the V_F results in Figure 23. At the same

654time, the footprints of X_S in the reservoir, as well as the increasing X_S levels, providing

655direct evidence of continuing (albeit localized) dissociation. All these results taken

656together indicate that there is no hydrate exhaustion in Case C2, and the reason for the

657significant reduction in gas release and production is that (a) the driving force of

658dissociation, i.e., the ΔP between well and reservoir, is now at a minimum and (b) the

659system temperature has fallen so much that further hydrate dissociation is not only

660severely reduced, but can also lead to localized hydrate reformation. This can also partly

661explain the increase in the salinity of the produced water observed in Figure 27.

662The evolutions over time in the spatial distributions of the same key parameters in Case

663C3 are very similar to those in Case C2, and will not be discussed in detail.

664

665**4.6. Conclusions drawn from the production performance in Cases C1, C2, and C3**

666The conclusion from the analysis of the closed systems in Cases C1 to C3 is that Site

667NGHP-02-09 may be a promising production target for full production operations despite

668its unsuitability as a location for a single vertical well test. However, this requires

669controlling the water inflows from the radial boundaries to increase the productivity of

670interior wells. For those interior wells of the multi-well pattern, depressurization can

671induce significant hydrate dissociation and gas production while water production can be

672manageable. The hydrate accumulations at this site seem to meet both an absolute

673criterion of high gas production and a relative criterion of manageable/low water

674production. Confounding costs and challenges include the need for installing lower-

675performing wells at the boundaries of the pattern that serve to control water influx at a

676single interior well. Larger arrays, though more expensive to construct, would offer more

677interior wells per exterior well.

678

679**5. Geomechanical system behavior**

680The geomechanical response was calculated for each of the cases discussed in the

681previous section using the one-way coupling process. The maximum strains found in the

682simulation domain for each of the cases is plotted in Figure 38. The evolution of the

683vertical displacements u_z along the z-axis (indicating uplift or subsidence) at the seafloor,

684top of the reservoir, and bottom of the reservoir are plotted in Figures 39. Snapshots of

685the displacement fields for each of the cases at three times are presented in Figures 40 to

68642. The snapshots are zoomed in at the production zone clearly indicate increasing

687magnitudes as time advances, as well as a progressive contraction ("squeezing") of the

688reservoir as the top subsides and the bottom is uplifted in response to depressurization.

689This is clearly demonstrated in Figure 39, which shows the evolution of the maximum

690and minimum u_z displacements in the vicinity of the vertical wells in cases R, C1 and C2.

691The displacements in Case R are minimal: practically zero at the ocean floor, a slight

692uplift at the base of the accumulation because of the effect of the Aqu10 layer that

693prevents depressurization, and a slight subsidence at the top of the accumulation in

694response to the proximity of the location of the maximum pressure drop near the top of

695the well operating at a constant P_w.   This minimal impact allows for the de-coupling of

696the geomechanical and production flow simulations that allow for tractable production

697simulations to be accomplished given the requirement for exceedingly fine reservoir

698discretizations. We recognize that in many systems with other characteristics, most

699notably more aggressive hydrate dissociation, full two-way coupling will be required to

700achieve more reliable production simulations.

701The displacements in the closed systems in cases C1 and C2 are far more substantial, and

702increase with a decreasing radius (and volume of the reservoir portion served by the

703individual wells). The depressurization of the system is primarily isolated to the reservoir

704layers, and consequently the reservoir sediments exhibit the most pronounced

705deformation. Because the overburden does not deform significantly, the subsidence at the

706ocean floor in these cases for the interior wells closely follows that at the top of the

707accumulation, and reaches about 4 m and almost 9 m at the end of their production

708periods in Cases C1 and C2, respectively, at which levels they appear to stabilize. The

709underburden is pulled up towards the well from the fixed based, so that the uplift at the

710base of the Case C1 reservoir is about 0.55 m, which, when combined with the

711subsidence at the top, indicated clear contraction "squeezing" of the reservoir at the well.

712These results indicate that production simulations for these alternative cases will be

713optimistic in comparison to fully-coupled simulations of these multi-well cases, should

714such simulations become practically possible in the future.

715The u_z displacements at the base of the accumulation in Case 2 follow a different pattern.

716There is an initial uplift that reaches a maximum of about 0.55 m, but the severe and

717progressing depressurization in the case leads to a pattern reversal after about $t = 30$ days

718and a continuous decline in the uplift, ending in subsidence that begins at about $t = 270$

719days and reaches very modest levels (0.2 m) at the end of the 540-production period. The

720displacement behavior in Cases C1 and C2 may have important implications for the

721construction, completion and stability of the well, and may impose specific material

722requirements in order to meet the mechanical challenges posed by such behavior.

723Obviously, the situation can change significantly if production from Cases C1 and C2

724ceases earlier than the production period of this study, and this is entirely possible

725because of the low (and declining, and eventually uneconomical) Q_P level after a certain

726point (see Figure 20).

727Plasticity was not incorporated in the one-way calculations of the geomechanical

728response, but the important stress factors were post-processed to estimate regions of

729possible failure. In Figures 43 to 45, the value of the Drucker-Prager yield criterion, a

730smooth version of the Mohr-Coulomb yield criterion, is plotted in the reservoir case for

731each region. Yield would be indicated by a criterion that is less than zero, where zero is

732the yield surface itself. We do not use a hydrate-dependent yield criterion and use only

733the cohesion of the hydrate-less sediment everywhere to serve as a lower bound for the

734estimates. Because of ineffective depressurization in Case R, the stresses are limited.

735This not the case in cases C1 and C2, which show increasing stress as depressurization

736becomes more effective with a decreasing volume of the domain under investigation. In

737case C2 with the most extreme depressurization, the hydrate-less sediments deform

738significantly, with one region indicated yielding in the second layer from the top, marked

739by a red circle in Figure 45. This is clearly demonstrated in Figure 38, which shows the

740evolution of the maximum and minimum ε_{zz} and ε_{rr} strains (over the reservoir volumes)

741over time. The strains are minimal in Case R, but can be significant (and possibly severe)

742in Case C2 where maximum depressurization and hydrate dissociation occurs.

743The conclusion drawn from these results is that full-field production from the hydrate

744accumulations at Site NGHP-02-09 site needs to carefully consider geomechanical issues

745that can be challenging. The authors of this study are unable to authoritatively proffer an

746opinion on whether the geomechanical criterion of the reservoir desirability as a

747production target can be met because of lack of the required well construction expertise

748to address the issue, and because other issues (e.g., when production should cease,

749decision that can be driven by both Q_P and economic considerations) can affect the

750maximum displacements experienced during production. As noted, to render these

751simulations tractable, progressive compaction in the reservoir, and the implied decrease

752in permeability, were not incorporated into the estimates of gas and water flow rates.

753Thus, the overall production values estimated in this study should be a first order review

754of a highly complex system.

755

756 6. Overall conclusions

757 The following conclusions can be drawn from this study:

758 ● Gas production from Site NGHP-02-09 under the conditions of a long-term field
759   test involving a single vertical well is *technically feasible* and can yield high gas
760   production rates. However, the high gas production is based mainly on exsolution
761   of dissolved gas rather than hydrate dissociation and is thus burdened by an
762   excessively large water production.

763 ● Given the properties and the geological model used in this study, Site NGHP-02-
764   09 does not appear to be a promising location for a field test of gas production
765   from the hydrate deposits of the KG Basin because of the presence and attributes
766   of the hydrate-free and extremely permeable Aqu10 layer short-circuit the
767   depressurization process.

768 ● Site NGHP-02-09 may be a more promising production target for a multi-well
769   operation despite its unsuitability as a single-well test location because the control
770   of the water inflows by the multi-well system promotes more effective
771   depressurization while keeping the water production within manageable limits.
772   These results suggest merit in further evaluation of economics of full-field
773   production of this reservoir. Such evaluation will need also to incorporate the
774   potentially significant geomechanical effects on production for the system.

775 ● The geomechanical issues associated with production from the hydrate
776   accumulations at Site NGHP-02-09 need to be carefully considered as significant
777   displacements are possible, which can be challenging to well construction and

778   stability. Note that other considerations (such as the point at which cessation of

779   production should occur, as dictated by economic and/or technical reasons) can

780   change significantly the severity of the geomechanical challenges.

781

782

797

73

798References

799 Boswell, R., Yoneda, J., Waite, W., this issue-a: India National Gas Hydrate Program

800   Expedition 02 summary of scientific results: Evaluation of natural gas hydrate-

801   bearing pressure cores.

802 Boswell, R., Myshakin, E., Moridis, G., Konno, Y., Collett, T., Reagan, M., Ajayi, T.,

803   Seol, Y., this issue-b: India National Gas Hydrate Program Expedition 02 summary of

804   scientific results: Numerical simulation of reservoir response to depressurization.

805 Collett, T., et al., this issue, India National Gas Hydrate Program Expedition 02 –

806   scientific results.

807 Kowalsky, M. B., and G.J. Moridis, 2007. Comparison of kinetic and equilibrium

808   reactions in simulating the behavior of gas hydrates, *Energy Conversion and*

809   *Management*, **48**, 1850, doi:10.1016/j.enconman.2007.01.017.

810 Kumar, P., et al., this issue, India National Gas Hydrate Program Expedition 02 –

811   operational and technical summary.

812 Li, G., G.J. Moridis, K. Zhang and X.-S. Li, Evaluation of Gas Production Potential from

813   Marine Gas Hydrate Deposits in Shenhu Area of the South China Sea, *Energy &*

814   *Fuels*, **24**, 6018-6033, 2010 (doi: 10.1021/ef100930m).

815 Liu, N., Pan, L., Cheng, J., 2017. Numerical Modeling of CO_2 and Brine Leakage

816   through Open Fracture in a Fault Zone: Open Channel Flow or Darcy Flow**,**

817   *Geofluids*, 2017, https://doi.org/10.1155/2017/9035032.

818 Marın-Moreno, H., T. A. Minshull, G. K. Westbrook, and B. Sinha 2015, Estimates of

819　future warming-induced methane emissions from hydrate offshore west svalbard for a

820　range of climate models, Geochemistry, Geophysics, Geosystems, 16(5), 1307–1323.

821 Moridis, G.J. and E.D. Sloan, 2007. Gas Production Potential of Disperse Low-Saturation

822　Hydrate Accumulations in Oceanic Sediments, *J. of Energy Conversion and*

823　*Management*, **48(**6)**, 1834-1849, doi: 10.1016/j.enconman.2007.01.23.

824 Moridis, G.J., Kowalsky, M.B., Pruess, K., 2007. Depressurization-induced gas

825　production from Class 1 hydrate deposits. *SPE Res. Eval. Eng.* **10** (5): 458-481.

826 Moridis, G.J., and Reagan, M.T., 2007a. Strategies for Gas Production From Oceanic

827　Class 3 Hydrate Accumulations, *OTC-18865*, 2007 Offshore Technology Conference,

828　Houston, Texas, 30 April − 3 May 2007.

829 Moridis, G.J., and Reagan, M.T., 2007b. Gas Production From Oceanic Class 2 Hydrate

830　Accumulations, *OTC 18866*, 2007 Offshore Technology Conference, Houston, Texas,

831　U.S.A., 30 April–3 May 2007.

832 Moridis, G.J., Kowalsky, M.B., and Pruess, K., 2008. TOUGH+HYDRATE v1.0 User's

833　Manual: A Code for the Simulation of System Behavior in Hydrate-Bearing Geologic

834　Media, Report LBNL-00149E, Lawrence Berkeley National Laboratory, Berkeley,

835　CA.

836 Moridis, G.J., M.T. Reagan, S.-J. Kim, Y. Seol and K. Zhang, 2009a. Evaluation of the

837 Gas Production Potential of Marine Hydrate Deposits in the Ulleung Basin of the

838 Korean East Sea, *SPE Journal*, **14**(4): 759-781, doi: 10.2118/110859-PA.

839 Moridis, G.J., T.S. Collett, R. Boswell, M. Kurihara, M.T. Reagan, E.D. Sloan and C.

840 Koh. Toward production from gas hydrates: assessment of resources and technology

841 and the role of numerical simulation, *SPE Reservoir Evaluation & Engineering*,

842 **12**(5): 745-771, 2009b (doi: 10.2118/114163-PA).

843 Moridis, G.J., and M.T. Reagan, 2011a. Estimating the Upper Limit of Gas Production

844 From Class 2 Hydrate Accumulations in the Permafrost, 1: Concepts, System

845 Description and the Production Base Case, *J. Petr. Sci. Eng.*, 76, 194-201,

846 (doi:10.1016/ j.petrol.2010.11.023).

847 Moridis, G.J., and M.T. Reagan, 2011b. Estimating the Upper Limit of Gas Production

848 From Class 2 Hydrate Accumulations in the Permafrost, 2: Alternative Well Designs

849 and Sensitivity Analysis, *J. Petr. Sci. Eng.*, 76, 124-137, 2011b (doi: 10.1016/j.petrol.

850 2010.12.001).

851 Moridis, G.J., Silpngarmlert, S., Reagan, M.T., Collett, T., Zhang, K., 2011c. Gas

852 production from a cold, stratigraphically bounded hydrate deposit at the Mount Elbert

853 site, North Slope, Alaska. *J. Marine Petr. Geol*., **28**, 517-534 (doi:

854 10.1016/j.marpetgeo.2010.01.005)

855 Moridis, G.J., M.T. Reagan, K.L. Boyle, and K. Zhang, 2011d. Evaluation of the Gas

856   Production Potential of Challenging Hydrate Deposits, *Transport in Porous Media*,

857   **90**, 269-299 (doi: 10.1007/s11242-011-9762-5).

858 Moridis, G.J. and Pruess, K. 2014. User's manual of theTOUGH+ Core code v1.5:A

859   general-purpose simulator of non-isothermal flow and transport through porous and

860   fractured media, LBNL Report 6871E, *https://pubarchive.lbl.gov/islandora/object/ir*

861   *%3A1005566.*

862 Moridis, G.J. 2014. User's manual for the HYDRATE v1.5 option of TOUGH+ v1.5:A

863   code for the simulation of system behavior in hydrate- bearing geologic media, LBNL

864   Report 6869E, *https://pubarchive.lbl.gov/islandora/object/ir%3A1005569.*

865 Moridis, G.J., A.F. Queiruga and M.T. Reagan, The T+H+M Code for the Analysis of

866   Coupled Flow, Thermal, Chemical and Geomechanical Processes in Hydrate-Bearing

867   Geologic Media, Paper 1195, Proceedings of the 9th International Conference on Gas

868   Hydrates, Denver, Colorado, 25-30 June 2017.

869 Pruess, K., Oldenburg, C.M., Moridis, G.J., 1999. TOUGH2 Users Guide, Version 2.0,

870   LBNL Report 43134,

871   *http://tough.lbl.gov/assets/docs/TOUGH2_V2_Users_Guide.pdf.*

872 Pruess, K., 2003. The TOUGH Codes – A Family of Simulation Tools for Multiphase

873   Flow and Transport Processes in Permeable Media, LBNL Report 53630,

874   *https://pubarchive.lbl.gov/islandora/object/ir%3A121930.*

875 Queiruga, A.F. and M.T. Reagan. (2018, February 2). tough_convert: Version 1.0.

876   Zenodo. http://doi.org/10.5281/zenodo.1164418

877 Rutqvist J. and G.J. Moridis, 2009. Numerical studies on the geomechanical stability of

878   hydrate-bearing sediments, *Soc. Pet. Eng. J.,* **14**(2), 267–282 (doi: 10.2118/126129-

879   PA).

880 Rutqvist J., Moridis G.J. and T. Grover, 2009. Geomechanical response of permafrost-

881   associated hydrate deposits to depressurization-induced gas production, *J. Pet. Sci.*

882   *Eng.,* **67**, 1-12.

883 Shukla, K.M., et al., this issue, Gas hydrate reservoir identification, characterization and

884   delineation in Krishna-Godavari Basin using surface and subsurface data from

885   Expedition NGHP-02, offshore India.

886 Stranne, C., O'Regan, M., Jakobsson M., 2016, Overestimating climate warming-induced

887   methane gas escape from the seafloor by neglecting multiphase flow dynamics,

888   *Geophys. Res. Lett.,* 43, doi:10.1002/ 2016GL070049.

889 Thatcher, K.E., Westbrook, G.K., Sarkar, S., Minshull, T.A., 2013, Methane release from

890   warming-induced hydrate dissociation in the West Svalbard continental margin:

891   Timing, rates, and geological controls, *J. Geophys. Res. Solid Earth*, 118(1), 22-38.

892 Waite, W., Jang, J., Collett, T., Kumar, P., this issue, Downhole physical property-based

893   description of gas hydrate petroleum system in NGHP-02 Area C: a channel, levee,

894   fan complex in the Krishna-Godavari basin offshore eastern India.

83

895 Yoneda, J., Oshima, M., Kida, M., Kato, A., Konno, Y., Jin, Y., Jang, J., Waite, W.,

896   Kumar, P., Tenma, N., this issue-a, Pressure-core based onshore laboratory analysis

897   on mechanical properties of hydrate-bearing sediments recovered during India's

898   National Gas Hydrate Program Expedition (NGHP) 02.

899 Yoneda, J., Oshima, M., Kida, M., Kato, A., Konno, Y., Jin, Y., Kumar, P., Tenma, N., this

900   issue-b, Permeability variation and anisotropy of gas hydrate-bearing pressure-core

901   sediments recovered from the Krishna-Godavari basin, offshore India.

902 Zhang, K., and Moridis, G.J., 2008. A Domain Decomposition Approach for Large-Scale

903   Simulations of Coupled Processes in Hydrate-Bearing Geologic Media, paper

904   presented at the 6th International Conference on Gas Hydrates, Vancouver, British

905   Columbia, Canada, July 6-10, 2008.

906

907
908
909
910
911
912
913
914
915
916

Table 1. Reservoir Conditions and Porous Media Properties in the Site NGHP-02-9 Study	
Hydrate dissociation model	Equilibrium
Overburden thickness	214.9 m
Underburden thickness	331.5 m
Initial pressure at top of domain/seafloor (P_T)	25.45 MPa
Pressure distribution with depth	Hydrostatic

Initial temperature at top of domain/seafloor (T_T)	3.46 $^{\circ}$C
Initial temperature at base of domain (T_B)	38.4 $^{\circ}$C
Temperature distribution with depth	Geothermal gradient (as affected by $k_{\Theta C}$)
Gas composition	100% CH_4
Water salinity	3.5%
Hydrate saturation in hydrate-bearing sands (HBS) S_H	0.75
Porosity (all formations) ϕ	0.45
Intrinsic permeability of the HBS layers k_r	10^{-11} m^2 (= 10.0 D)
Initial effective permeability of the HBS layers $k_{r,eff}$	10^{-15} m^2 (= 1 mD)
Intrinsic permeability of the other sand layers k_r	10^{-11} m^2 (= 10.0 D)
Intrinsic permeability of the mud layers k_r	10^{-17} m^2 (= 0.01 mD)
Intrinsic permeability of overburden/underburden k_r	10^{-17} m^2 (= 0.01 mD)
k_r/k_v	1 (all media)
Pore compressibility of sand layers	1.3×10^{-8} Pa^{-1}
Pore compressibility of mud layers	8.3×10^{-8} Pa^{-1}
Grain density ρ_R	2750 kg/m^3 (overburden)
	2700 kg/m^3 (all other formations)
Media specific heat (C_R)	1000 J/kg/K (all formations)
Wet thermal conductivity ($k_{\Theta RW}$)	1.76 W/m/K (all formations)
Dry thermal conductivity ($k_{\Theta RD}$)	0.3 W/m/K (all formations)
Composite (water, hydrate, ice, rock) thermal conductivity model (Moridis et al., 2014)	$k_{\Theta C} = k_{\Theta RD} + (S_A^{1/2} + S_H^{1/2})\,(k_{\Theta RW} - k_{\Theta RD}) + \phi\,S_I\,k_{\Theta I}$
Capillary pressure model (van Genuchten, 1980)	$$P_{cap} = -P_0 \left[\left(S^*\right)^{-1/\lambda} - 1 \right]^{-\lambda}$$ $$S^* = \frac{(S_A - S_{irA})}{(S_{mxA} - S_{irA})}$$
λ	0.45 (sand); 0.25 (clay/mud)
P_0	10^4 Pa (sand); 10^6 Pa (clay/mud)
Relative permeability model (Moridis et al., 2014)	$k_{rA} = (S_A^*)^n$
	$k_{rG} = (S_G^*)^m$
	$S_A^* = (S_A - S_{irA})/(1 - S_{irA})$
	$S_G^* = (S_G - S_{irG})/(1 - S_{irA})$
$n; m$	3.855; 2.5 (sand)
	3.5; 2.5 (clay/mud)
Irreducible gas saturation S_{irG}	0.01 (sand); 0.03 (clay/mud)
Irreducible water saturation S_{irA}	0.10 (sand); 0.90 (clay/mud)
Constant bottomhole pressure BHP (P_w)	3.0 MPa

917
918
919

920
921

Table 2. Material Geomechanical Properties in the Site NGHP-02-9 Study						
Layers	Young's modulus	Skeletal density	Poisson ratio	Shear modulus	Cohesion	Friction Angle
Mud zones: Overburden	E=109 MPa	2750 kg/m^3	0.30	6 MPa	0.5 MPa	30°
Sand zones	E=50 MPa (at S_H=0) E=199 MPa (at S_H=1)	2700 kg/m^3	0.40	16 MPa	0.5 MPa	30°
Underburden	E=109 MPa	2700 kg/m^3	0.30	8 MPa	0.5 MPa	30°
Interlayer mud zones	E=109 MPa	2700 kg/m^3	0.30	7 MPa	0.5 MPa	30°

922
923
924
925

926
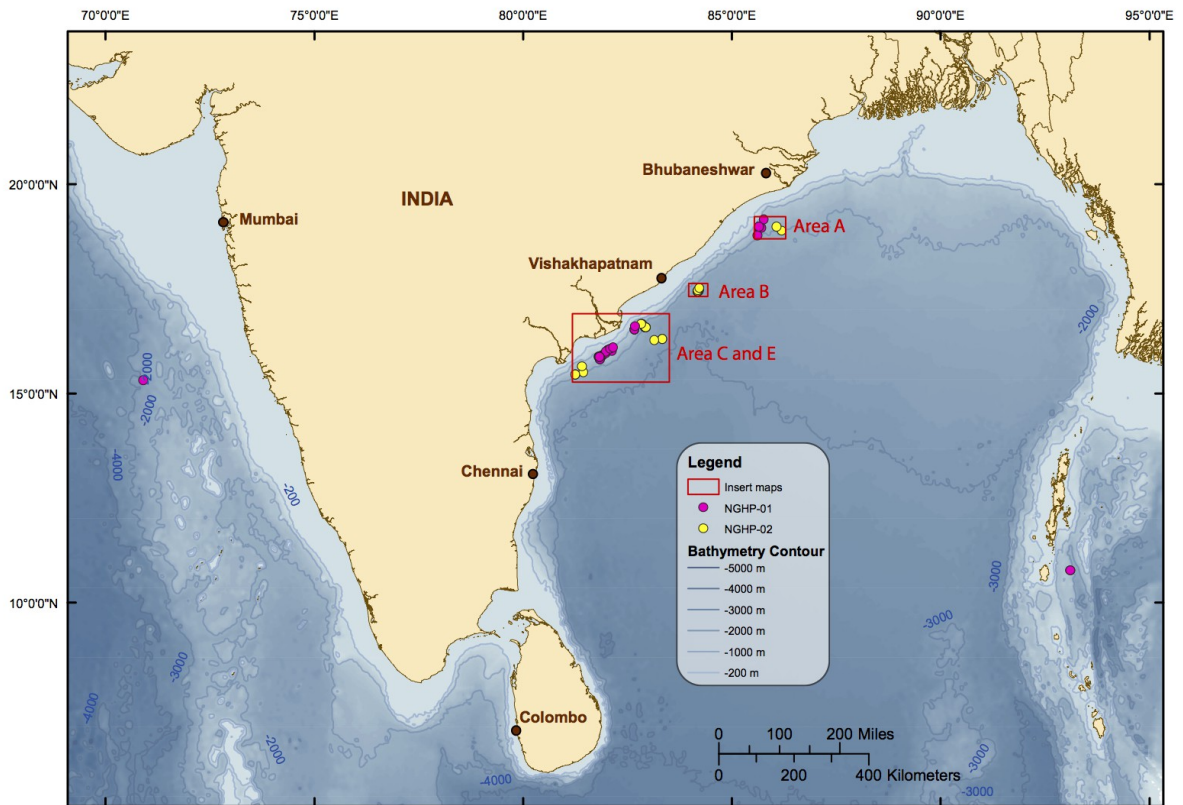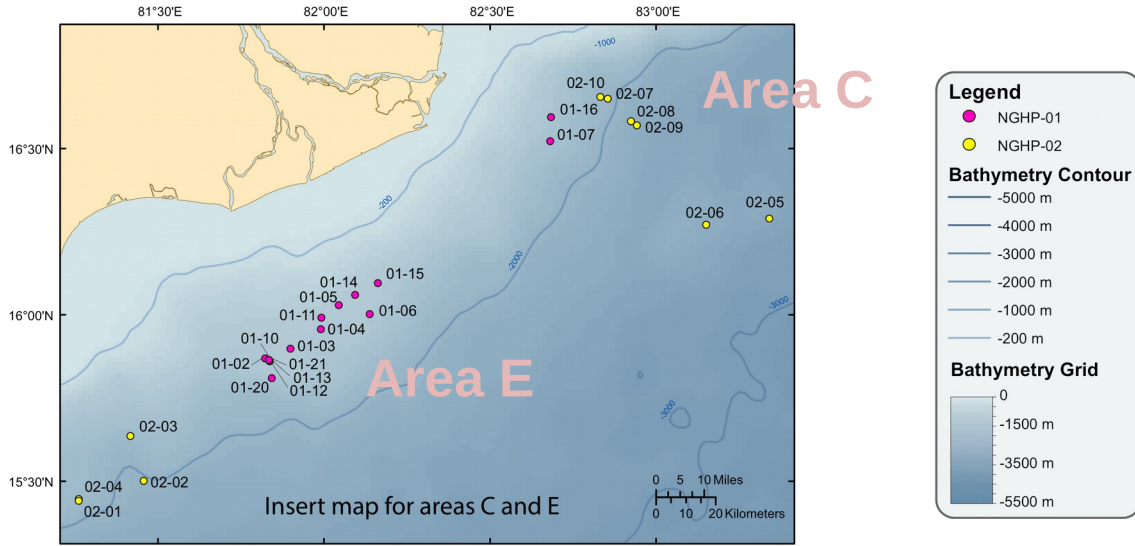
929**Figure 1.** Physiographic map of the Krishna-Godavari (KG) Basin, areas of investigation during the NGHP-
93002 scientific cruise, and location of Site NGHP-02-09 (NGHP-02 Expedition Scientific Party).

931

932
933
934
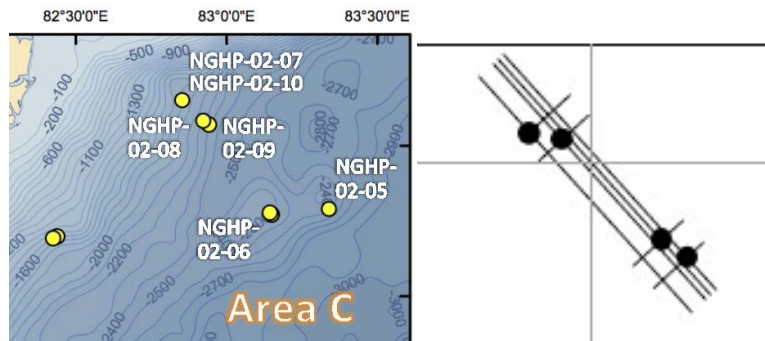
935
936

Seismic profile showing slope sediment with channel-levee system in Area C, NGHP Expedition 02.

937

NGHP-02-10 NGHP-02-07   NGHP-02-08 NGHP-02-09
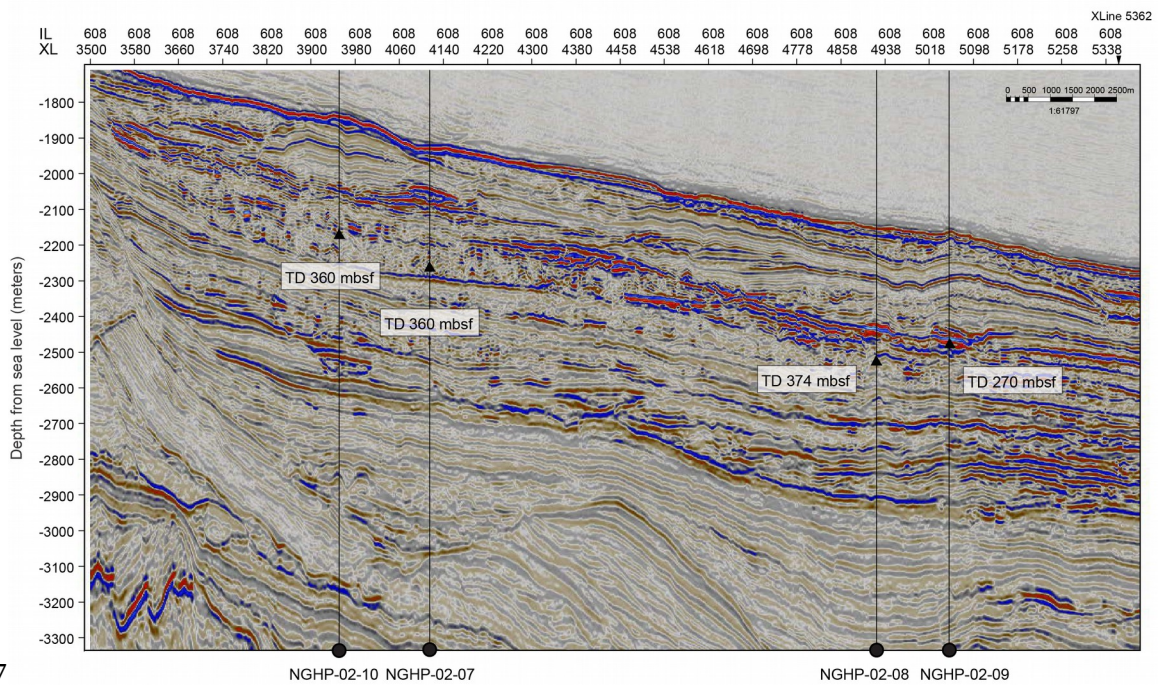
938**Figure 2 –** The gas hydrate petroleum system in the KG Basin, seismic profile showing the slope-rise
939channel-levee system in Area C. Sites NGHP-02-08 and -09 penetrate levee deposits on either side of the
940channel near the toe of the continental slope (Collett et al., this issue).

941

942

944

945
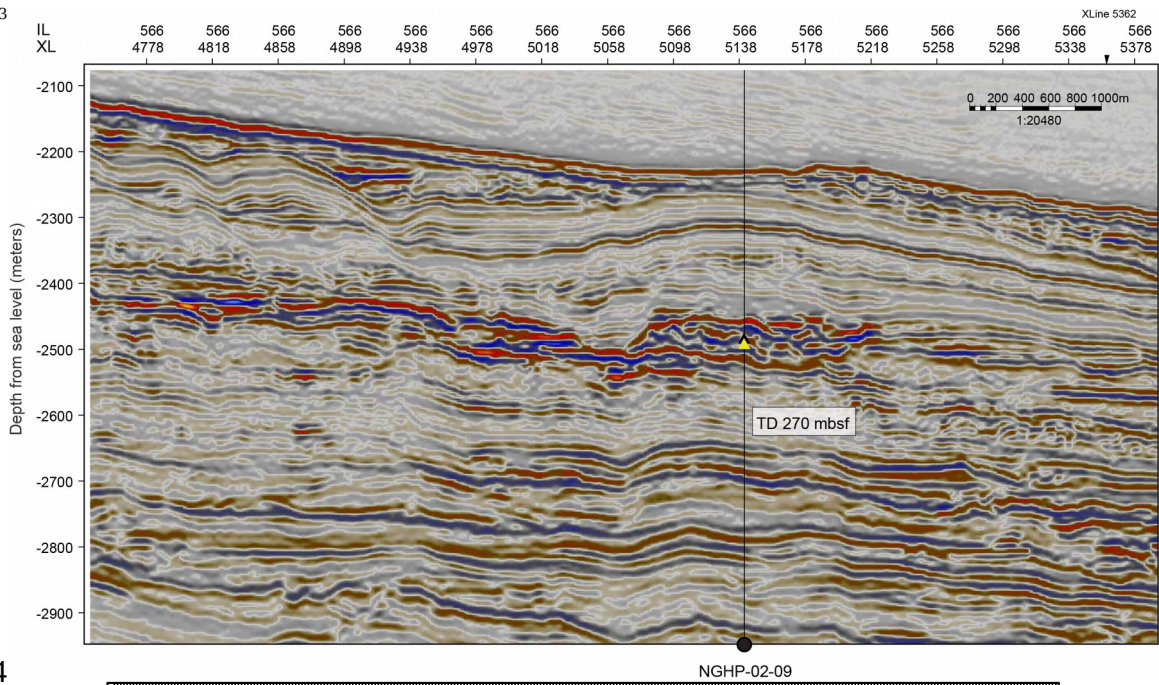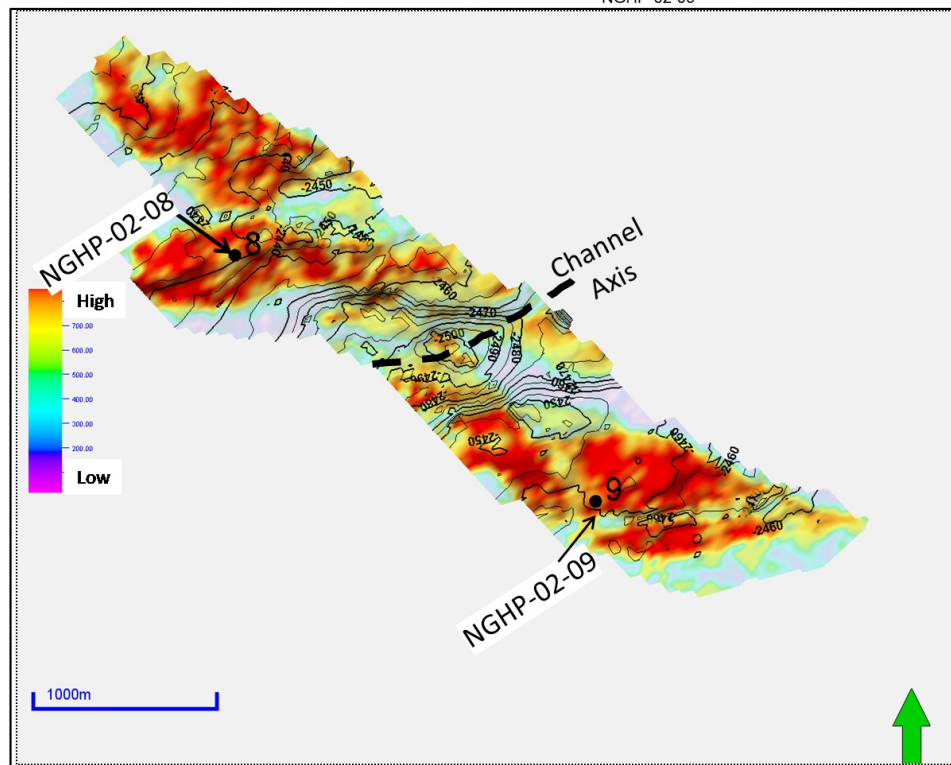
Figure 3. (a) Seismic profile through Site NGHP-02-09 (Collett et al., this issue), showing an image of the slope-rise channel-levee system in Area C.(b) Seismic amplitude distribution at 40 ms (TWT) close to the top of the gas hydrate reservoir at Sites NGHP-02-08 and NGHP-02-09 in Area C (Shukla et al., this issue).

949

950

951

952
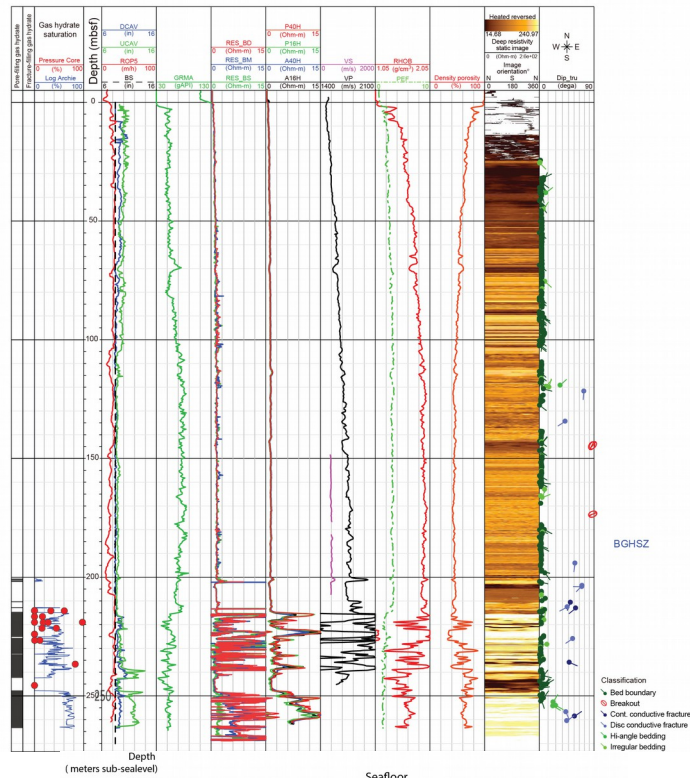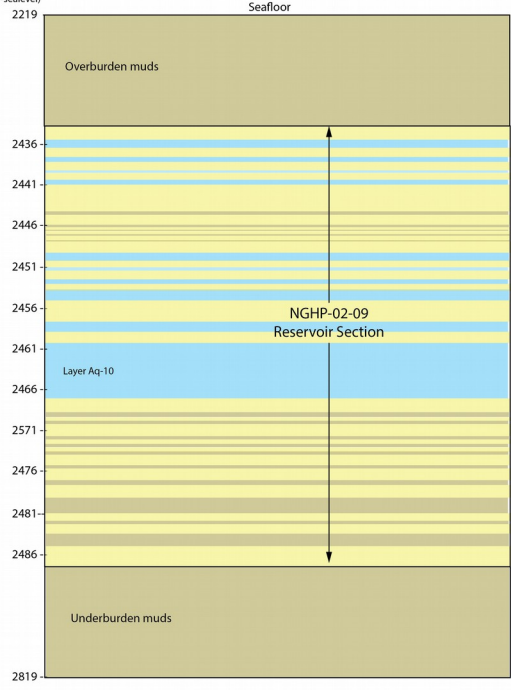
Figure 4. (a) Composite LWD log data display for Hole NGHP-02-09-A. BS =bit size, ROP5 =rate of penetration averaged over the last 5 ft, UCAV = ultrasonic caliper, DCAV = density caliper, GRMA = natural gamma radiation, RES_BD = deep button resistivity, RES_BS = shallow button resistivity, RES_BM = medium button resistivity, P40H/P16H = phase-shift resistivity, A40H/A16H = attenuation resistivity, VS = shear velocity, VP = compressional velocity, PEF = photoelectric factor, RHOB = bulk density (Collett et al.,

958 this issue). (b) Interpreted layered reservoir geology at Site NGHP-02-09 (Area C) in the KG Basin (Collett et
959 al., this issue).
960
961
962

963
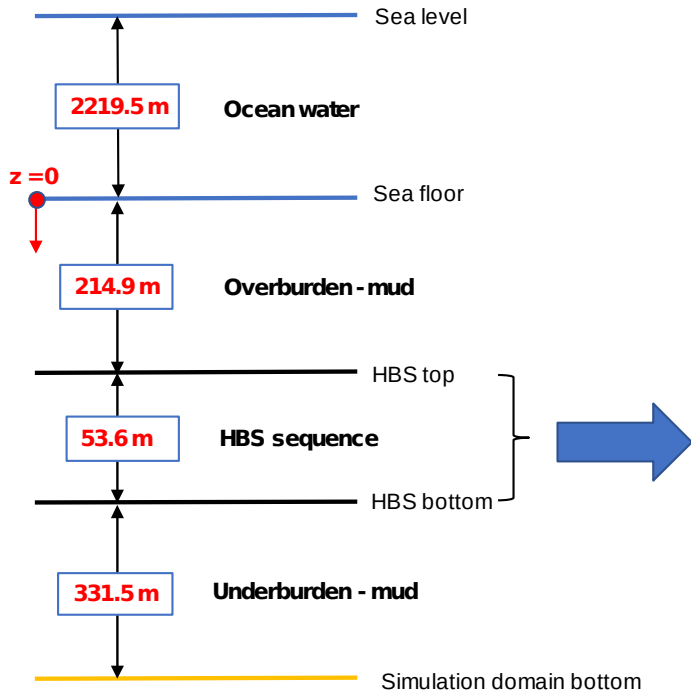
Layer #	Layer Name	Δz (m)	Z$_b$ (m)
1	Hyd01	1.8	-216.7
2	Aqu01	0.8	-217.5
3	Hyd02	1.3	-218.8
4	Aqu02	0.5	-219.3
5	Hyd03	1.1	-220.4
6	Aqu03	0.2	-220.6
7	Hyd04	0.8	-221.4
8	Aqu04	0.6	-222.0
9	Hyd05	3.3	-225.3
10	Mud01	0.5	-225.8
11	Hyd06	1.3	-227.1
12	Mud02	0.4	-227.5
13	Hyd07	0.3	-227.8
14	Mud03	0.2	-228.0
15	Hyd08	0.4	-228.4
16	Mud04	0.2	-228.6
17	Hyd09	0.5	-229.1
18	Mud05	0.2	-229.3
19	Hyd10	1.3	-230.6
20	Aqu05	1.1	-231.7
21	Hyd11	0.8	-232.5
22	Aqu06	0.3	-232.8
23	Hyd12	1.1	-233.9
24	Aqu07	0.4	-234.3
25	Hyd13	0.7	-235.0
26	Aqu08	1.3	-236.3
27	Hyd14	2.6	-238.9
28	Aqu09	1.2	-240.1
28	Hyd15	1.3	-241.4
30	Aqu10	6.9	-248.3
31	Hyd16	1.7	-250.0
32	Mud06	0.6	250.6
33	Hyd17	2.3	-252.9
34	Mud07	0.4	-253.3
35	Hyd18	0.5	-253.8
36	Mud08	0.4	-254.2
37	Hyd19	0.5	-254.7
38	Mud09	0.4	-255.1
39	Hyd20	1.2	-256.3
40	Mud10	0.4	-256.7
41	Hyd21	1.4	-258.1
42	Mud11	0.6	-258.7
43	Hyd22	1.5	-260.2
44	Mud12	2.0	-262.2
45	Hyd23	0.8	-263.0
46	Mud13	0.4	-263.4
47	Hyd24	1.2	-264.6
48	Mud14	1.4	-266.0
49	Hyd25	2.5	-268.5

964

965

966 **Figure 5**. A simple representation (not to scale) of the geology, stratification, texture and dimensions in the 967 subsurface at at Site NGHP-02-09 of the KG Basin, as used in the description of the simulation domain. 968 The "Hyd", "Aqu" and "Mud" prefixes in the layer description indicate hydrate-bearing sand, hydrate-free 969 sand and mud, respectively. The origin of the z-axis used in the simulation grid coordinates is also clearly 970 shown.

971
972

973
974

975
976
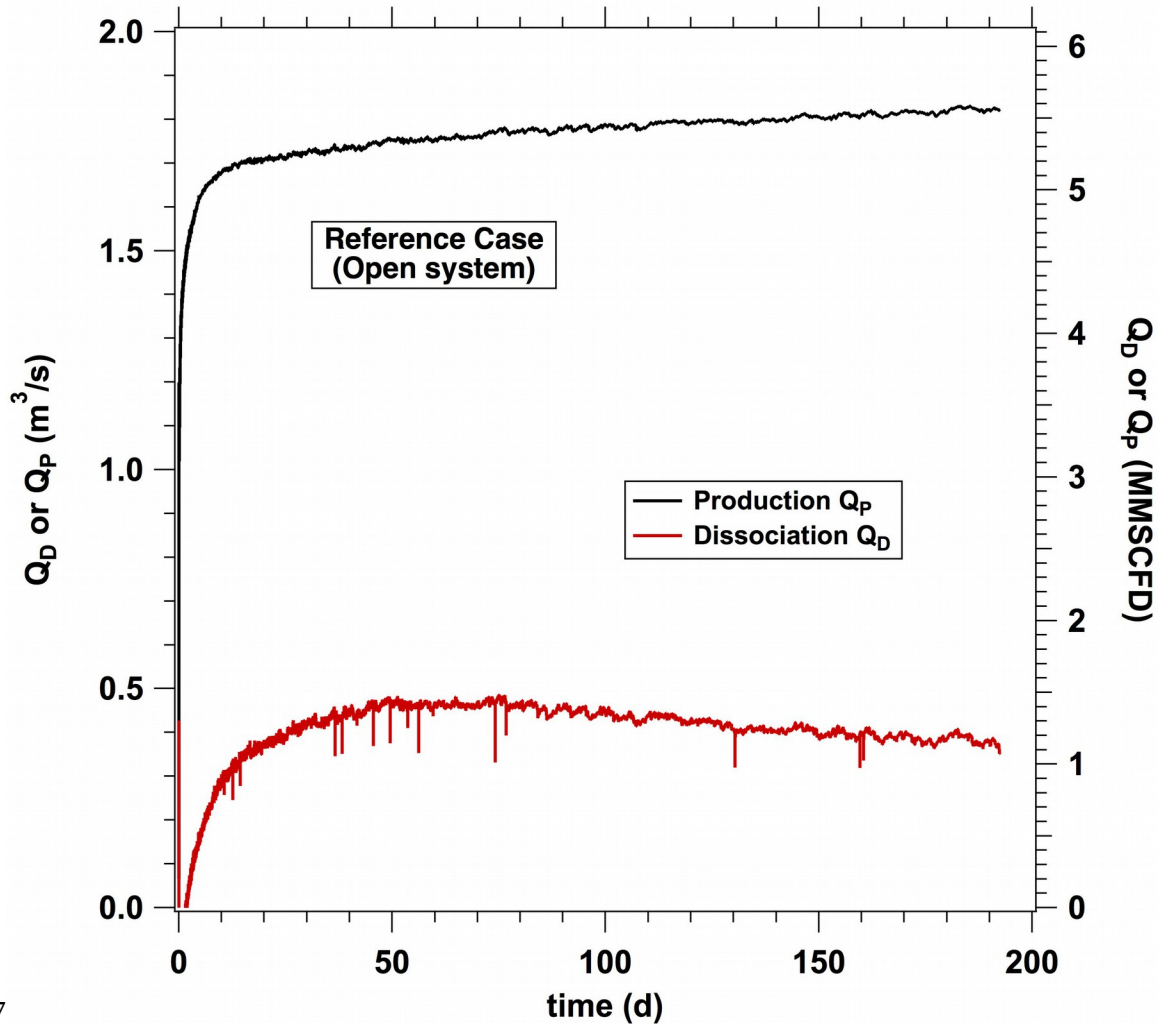
978

979**Figure 6.** Reference Case R (open system, infinite-acting boundaries): expected evolution of the rate of gas 980release from dissociation (Q_D) and the rate of gas production (Q_P) over time during the planned long-term 981field test at Site NGHP-02-09 of the KG Basin. Note that Q_D is consistently (and substantially) lower than Q_P. 982
983

984
985
986

987
988
989
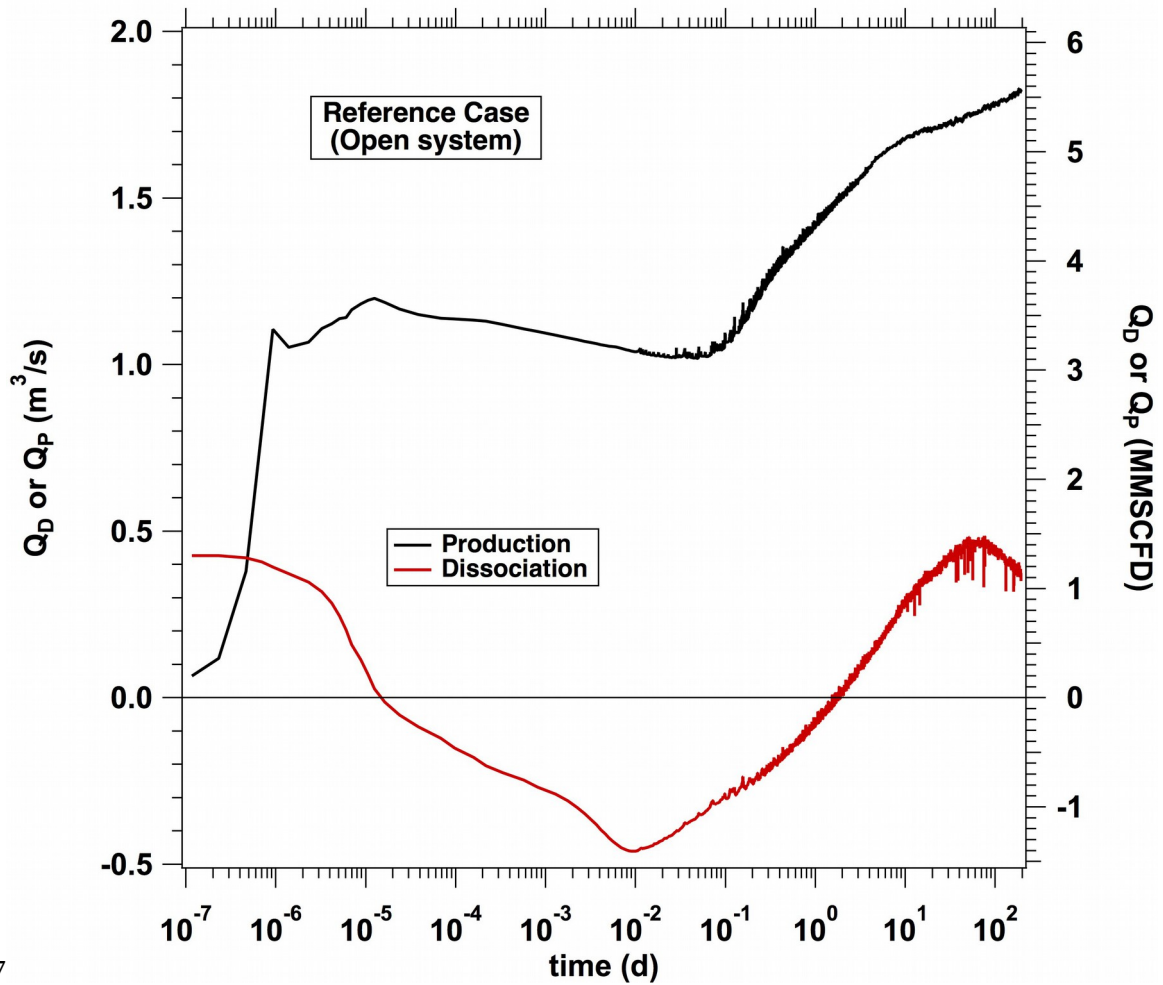
990**Figure 7.** Semi-log plot of the expected evolution of Q_D and Q_P of the reference Case R (shown in **Fig. 6**)
991that captures the early time behavior of the system. The negative Q_P immediately after the initiation of
992production is attributed to secondary hydrate formation involving gas released from exsolution in the water.
993
994

995
996
997
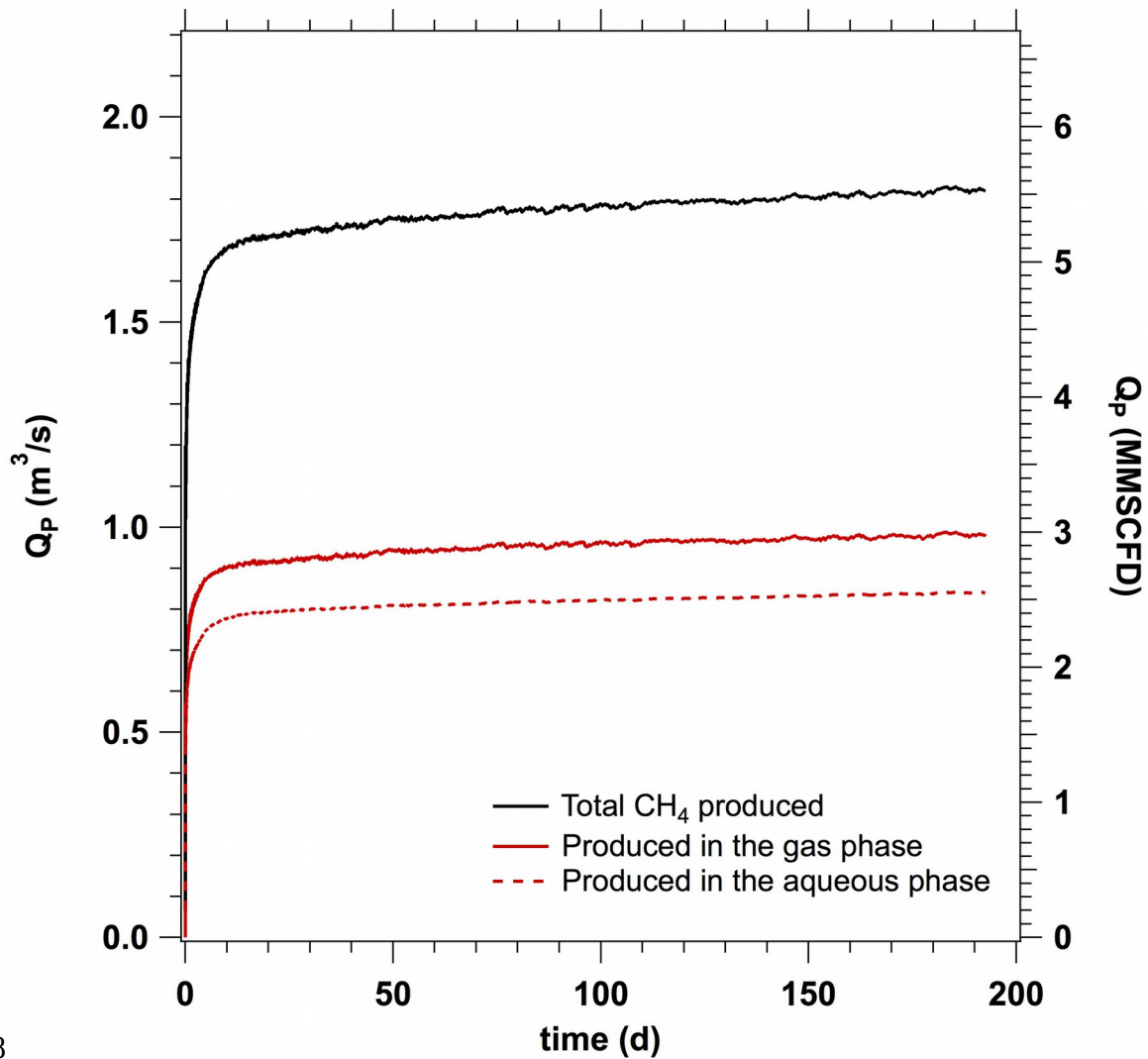
998
999
1000
1001**Figure 8.** Provenance of gas in the produced fluids for Case R. **E**xsolution of dissolved gas from the
1002produced water provides almost as much gas as as derived from hydrate dissociation to the total produced
1003methane, Q_P, seen in Figure 6.
1004
1005

1006
1007
1008
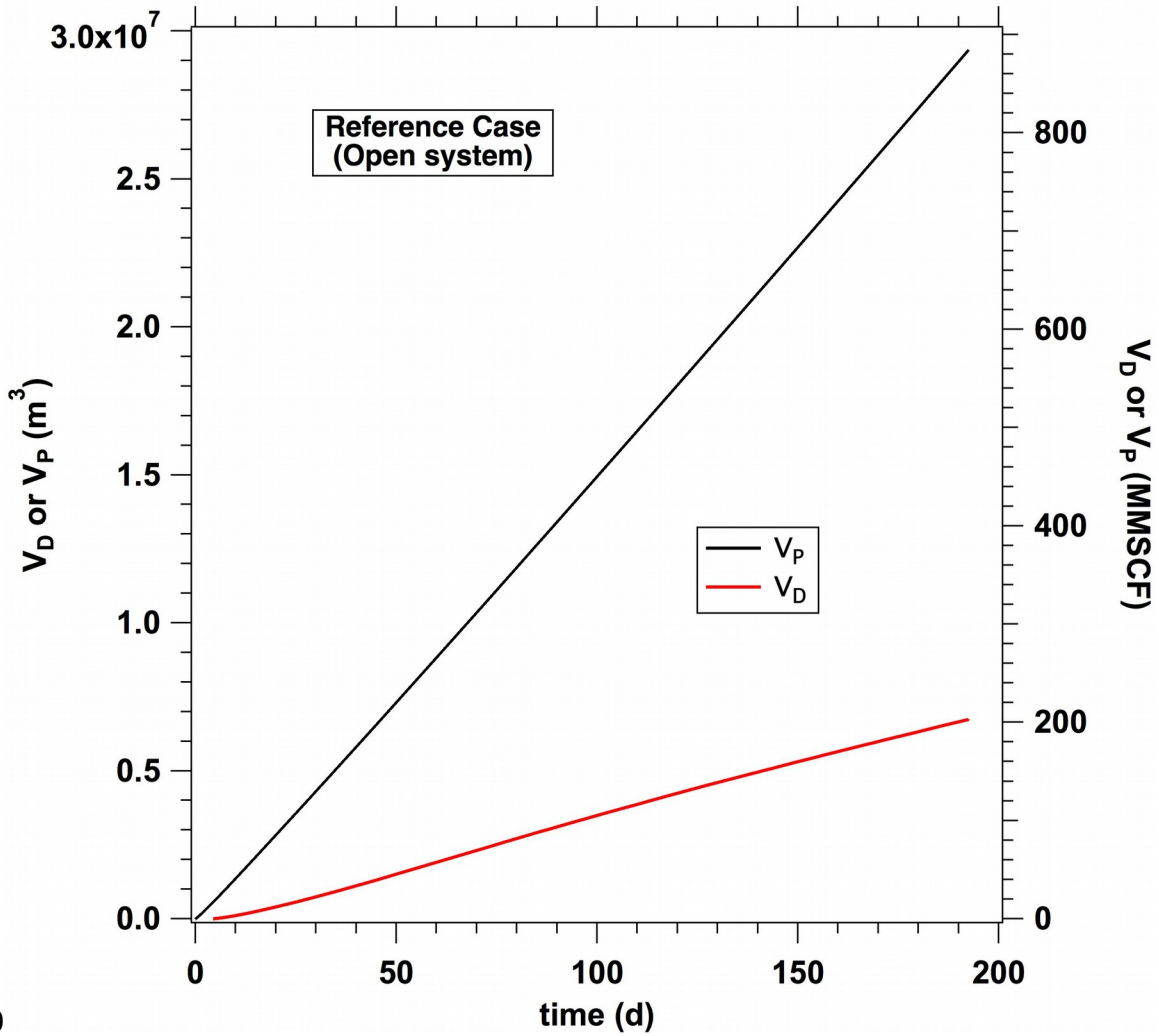
1009
1010
1011
1012**Figure 9.** Reference Case R (open system): Cumulative volumes of released and produced gas (V_D and V_P,
1013respectively) over time during the planned long-term test at Site NGHP-02-09 of the KG Basin. Note that V_D
1014< V_P at all times.
1015
1016

1017
1018
1019

Figure 10. Reference Case R (open system): evolution of the volume of the free gas phase in the reservoir (V_F) over time during the planned long-term test at Site NGHP-02-09 of the KG Basin. Note the modest V_F magnitude and its relative stability for t > 50 days.
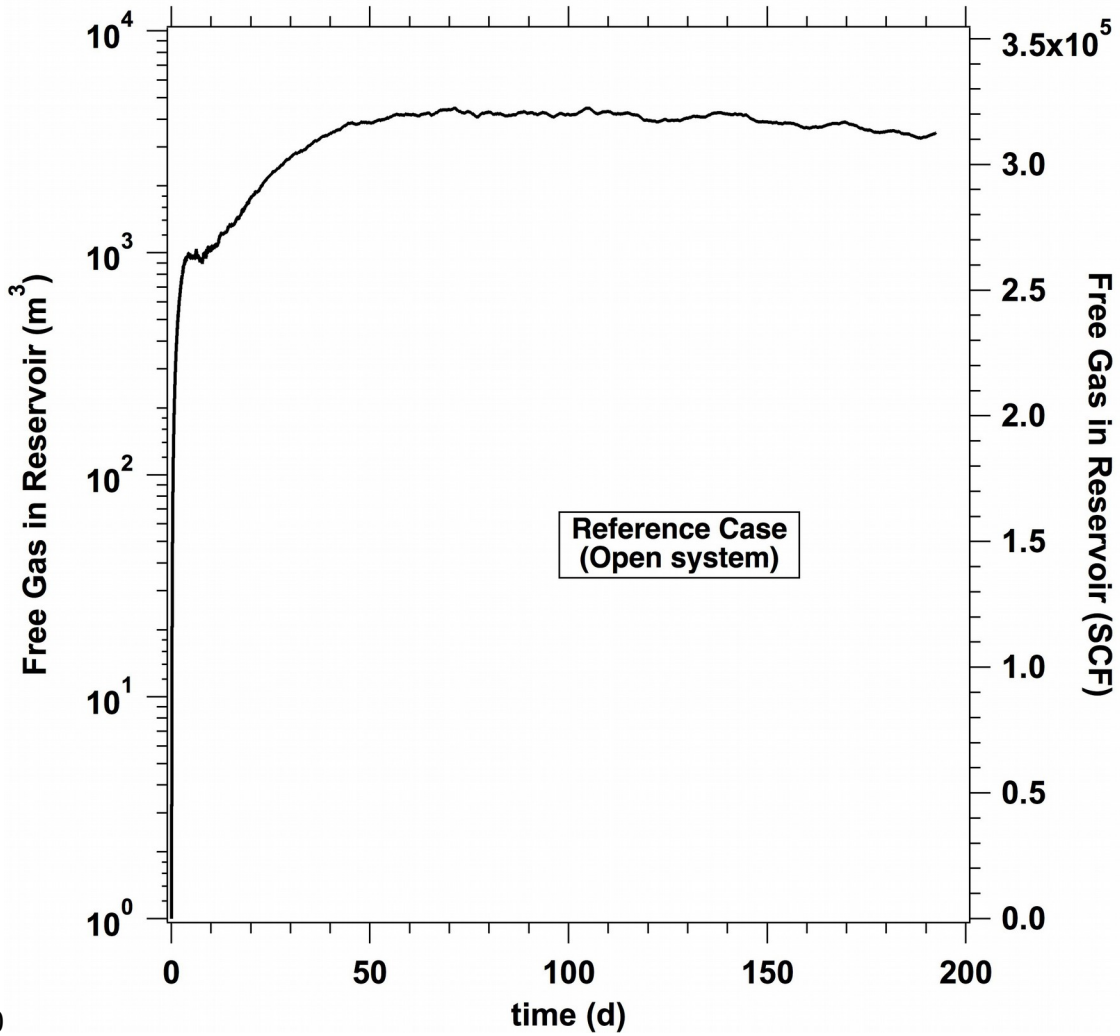
1020
1021
1022
1023
1024
1025
1026
1027

111

1028
1029
1030
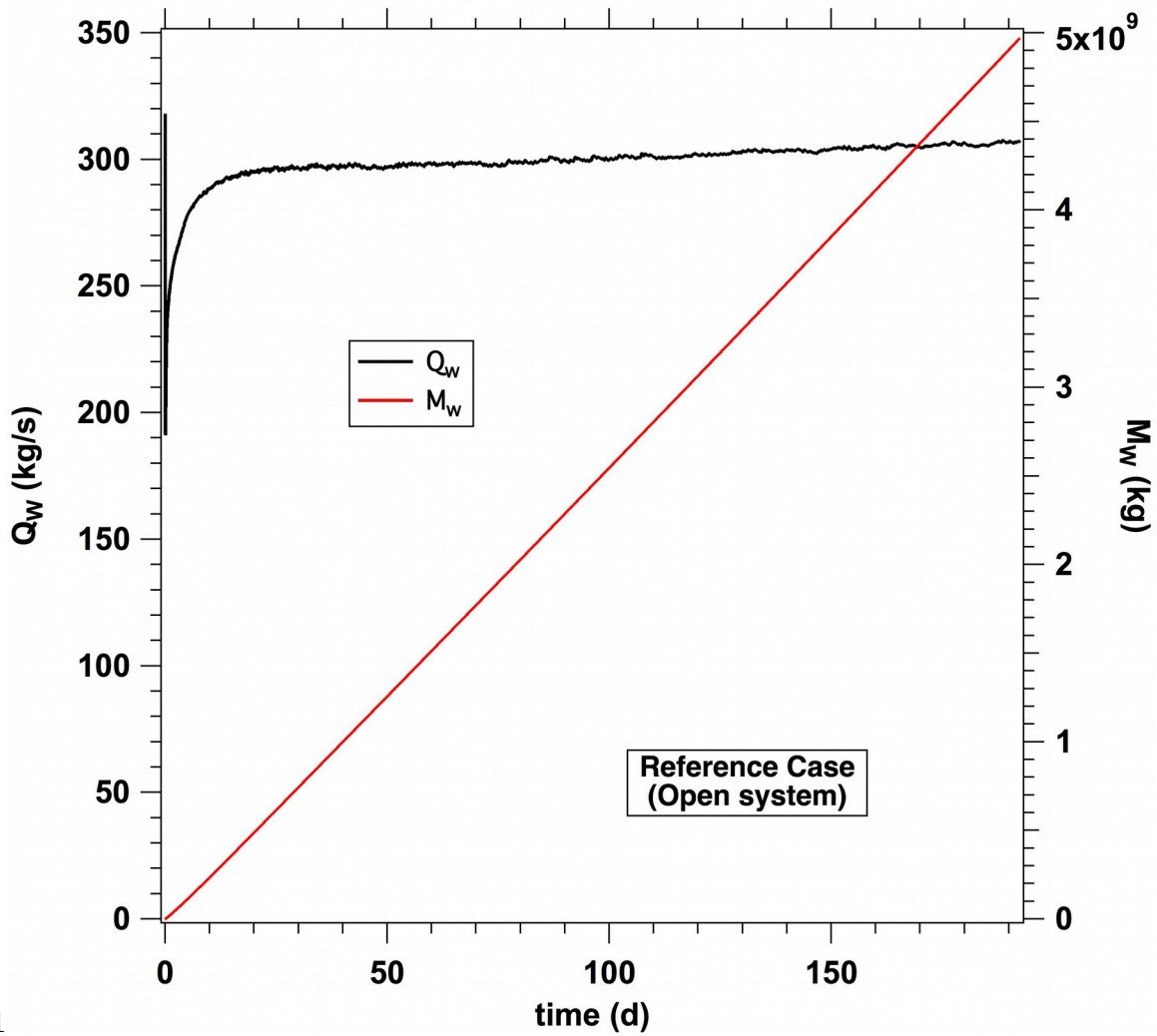
1031
1032
1033
1034**Figure 11.** Reference Case R (open system): evolution of (a) the rate of water production (Q_w) and (b) the
1035cumulative mass of water (M_w) over time during the planned long-term test at Site NGHP-02-09 of the KG
1036Basin. Note the non-declining Q_w for practically the entire test period.
1037
1038

113

1039
1040
1041
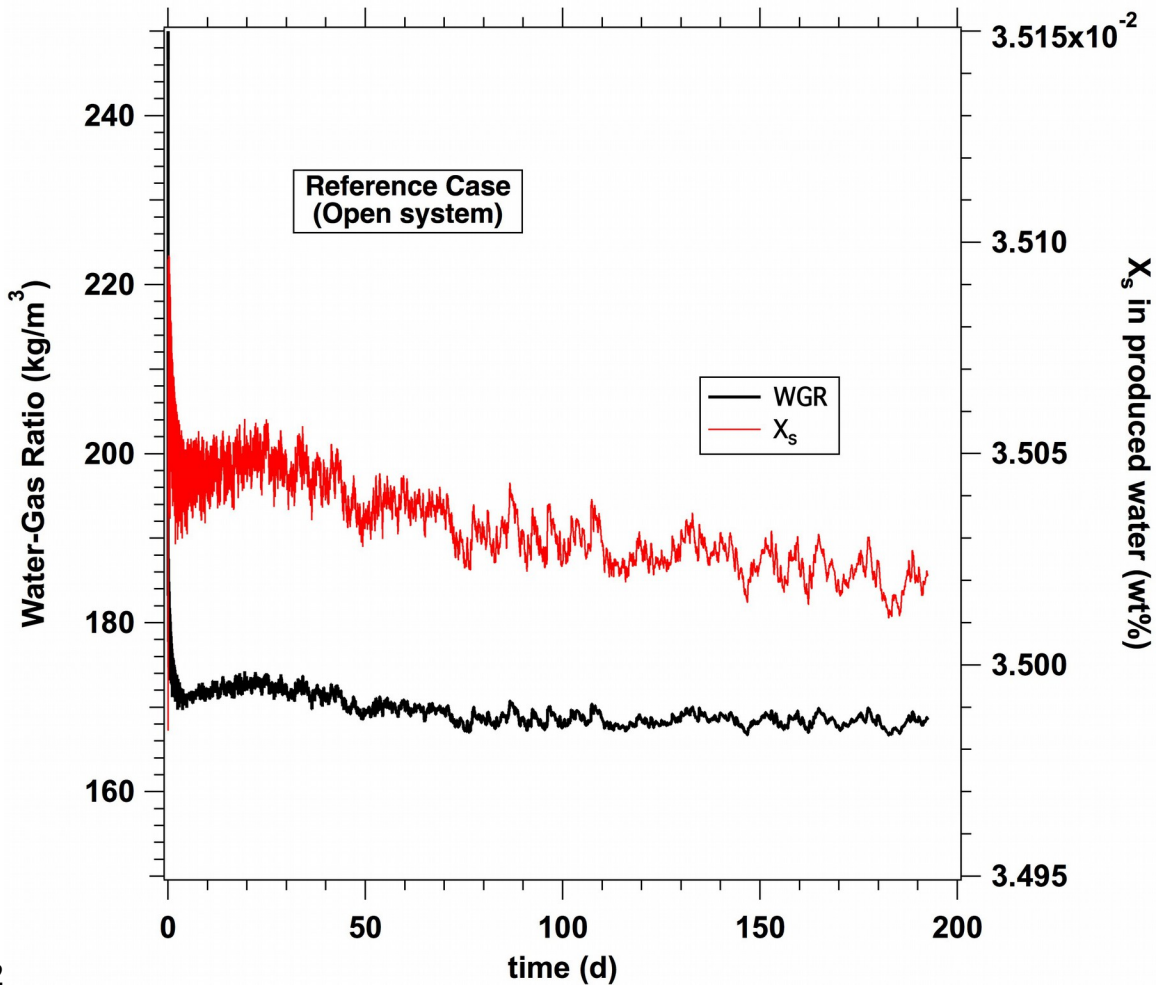
1042
1043
1044
1045**Figure 12.** Reference Case R (open system): evolution of (a) the water-to-gas ratio (*WGR*) and (b) the salt
1046mass fraction X_s in the produced water during the planned long-term test at Site NGHP-02-09 of the KG
1047Basin. Note the high-value (and stability) of WGR during the test period, and the high level of X_s.
1048
1049

1050
1051
1052
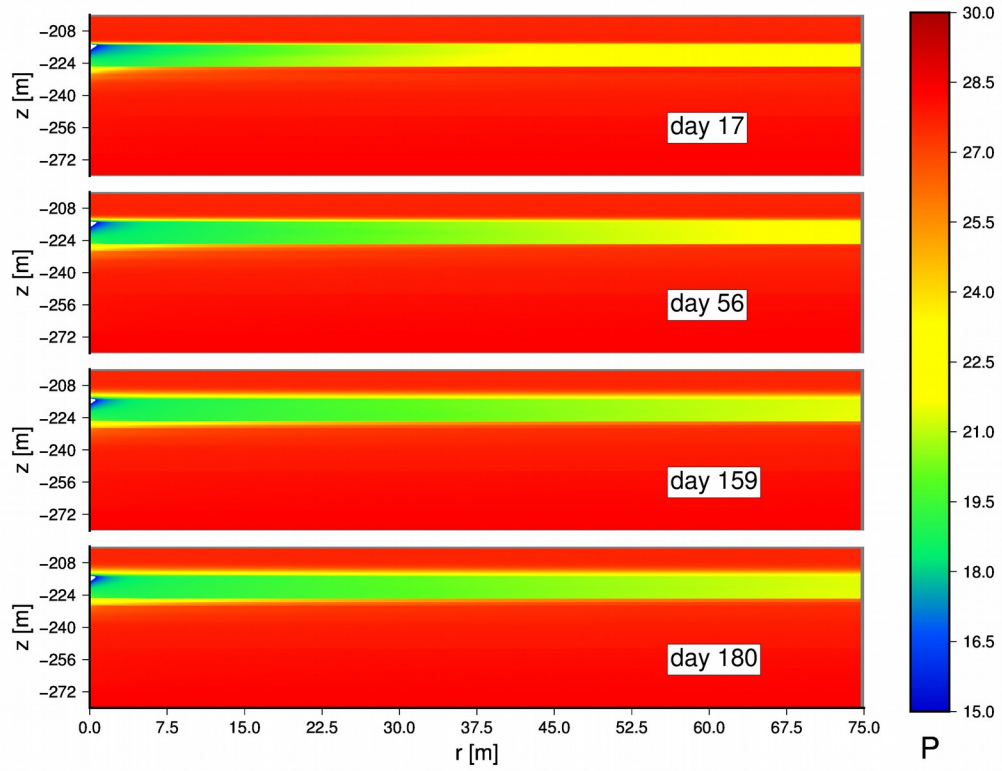
1053
1054
1055**Figure 13.** Case R: Evolution of pressure (in MPa) distribution in the system during the long-term production
1056test at Site NGHP-02-09 of the KG Basin (P_w = 3 MPa).
1057
1058
1059

1060
1061
1062
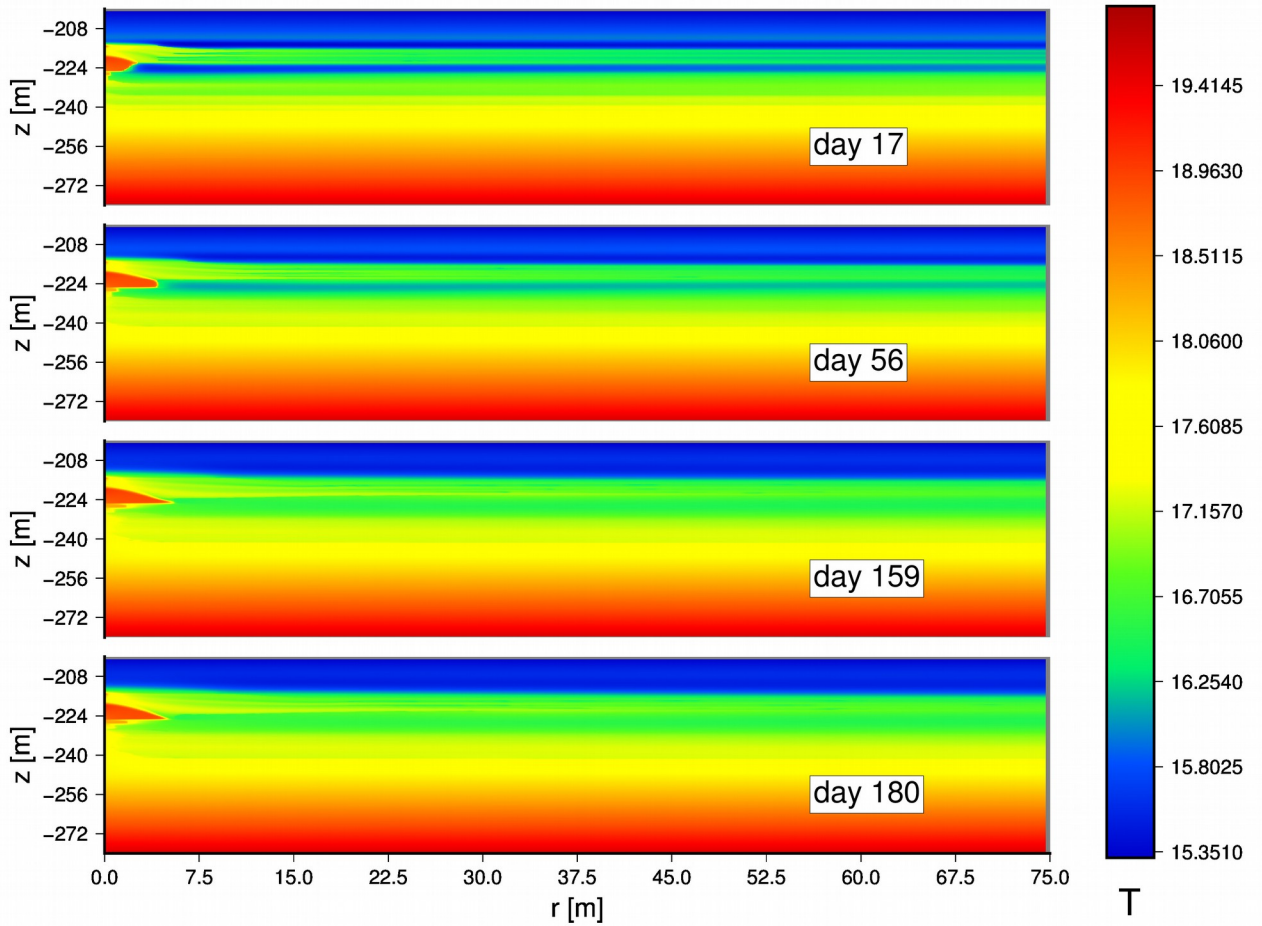
1063
1064
1065**Figure 14.** Case R: Evolution of temperature (in ^{o}C) distribution in the system during the long-term
1066production test at Site NGHP-02-09 of the KG Basin (P_w = 3 MPa).

1067
1068
1069

1070
1071
1072
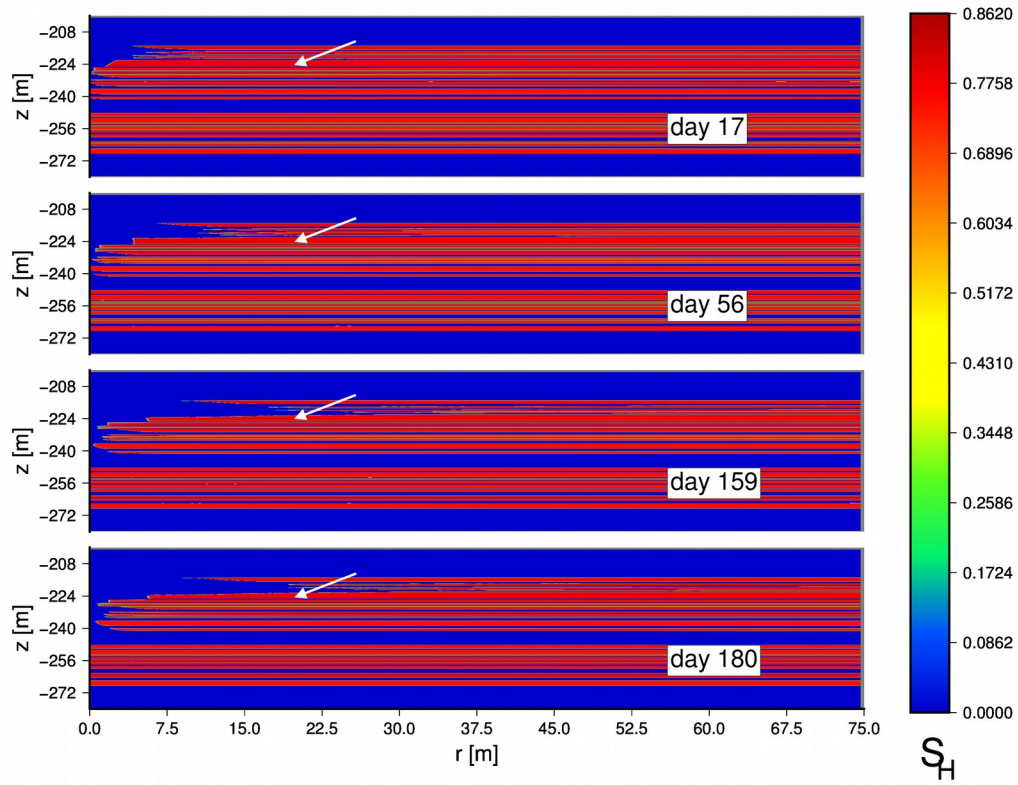
1073
1074
1075**Figure 15.** Case R: Evolution of the hydrate saturation S_H distribution in the system during the long-term
1076production test at Site NGHP-02-09 of the KG Basin (P_w = 3 MPa). Arrows indicate layers where S_H > 0.75.
1077
1078
1079

1080
1081
1082
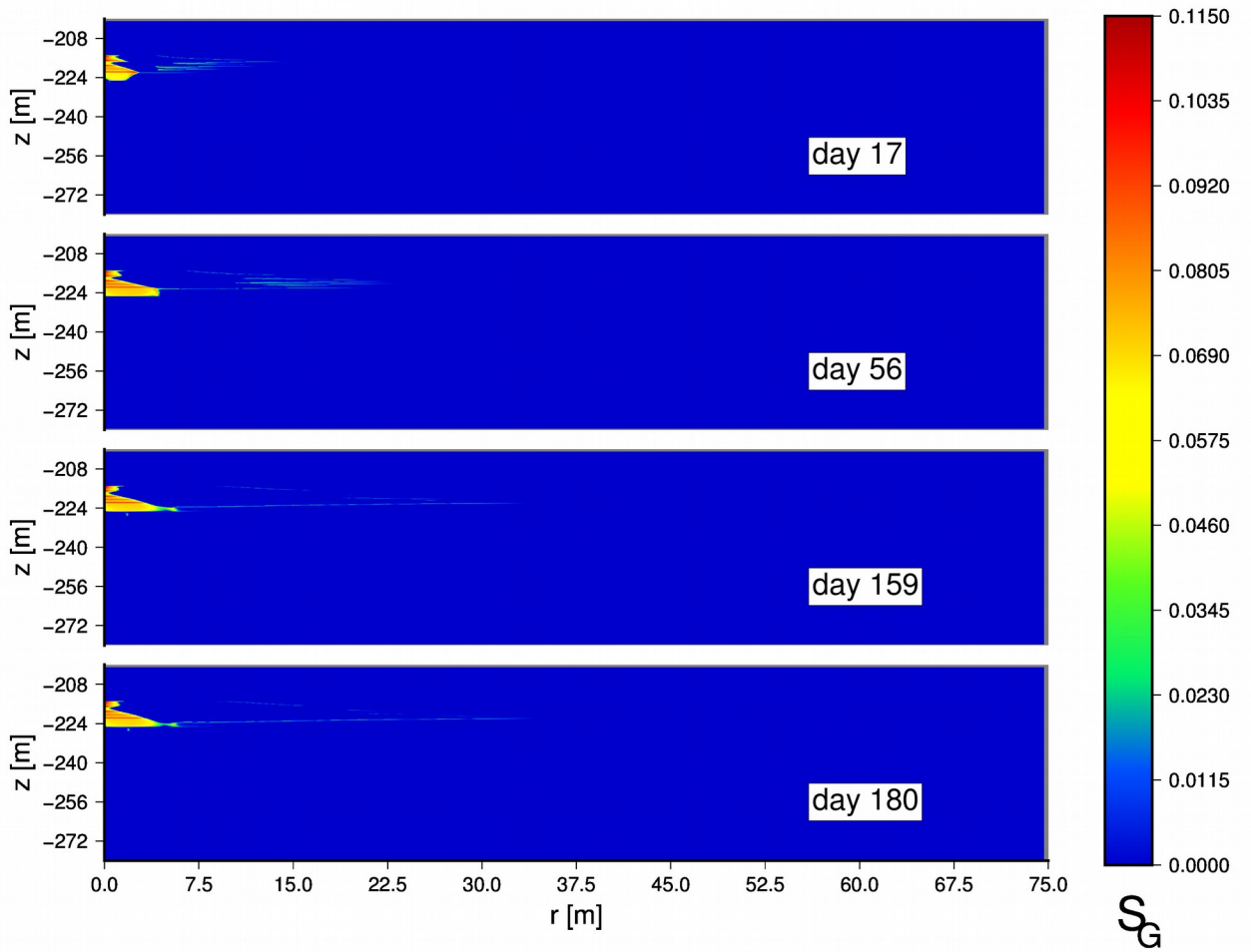
1083
1084
1085**Figure 16.** Case R: Evolution of the gas saturation S_G distribution in the system during the long-term 1086production test at Site NGHP-02-09 of the KG Basin (P_w = 3 MPa).

1087
1088
1089

1090
1091
1092
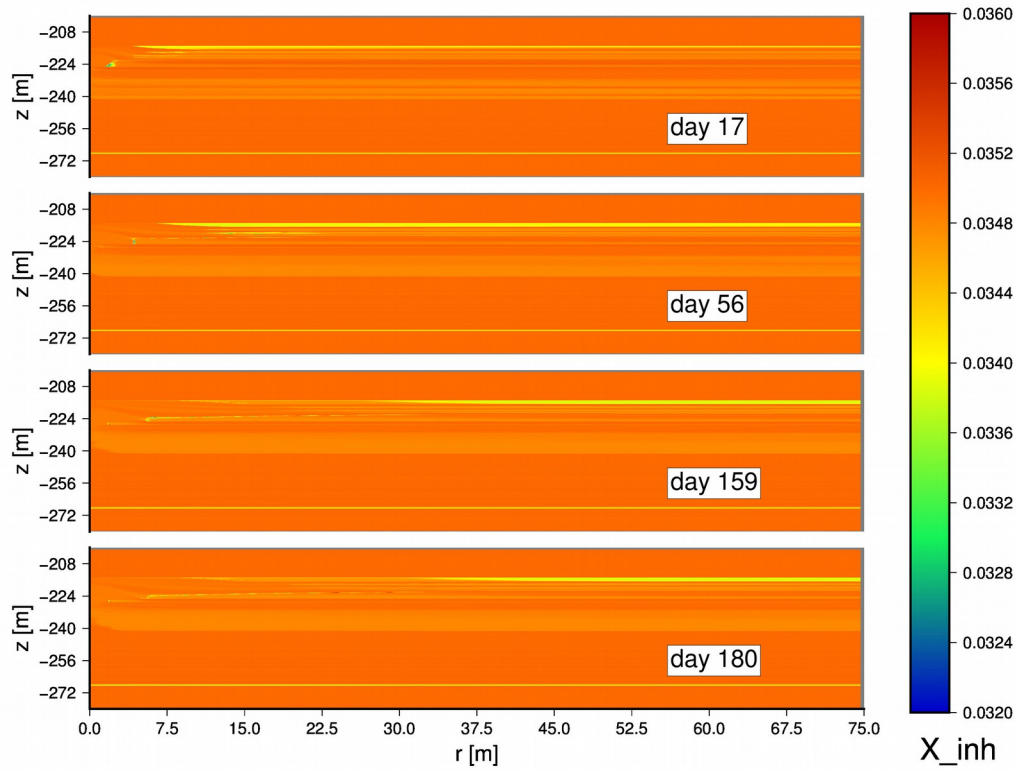
1093
1094
1095**Figure 17.** Case R: Evolution of the distribution of the salt mass fraction X_S in the aqueous phase of the
1096system during the long-term production test at Site NGHP-02-09 of the KG Basin.
1097

1098
1099
1100
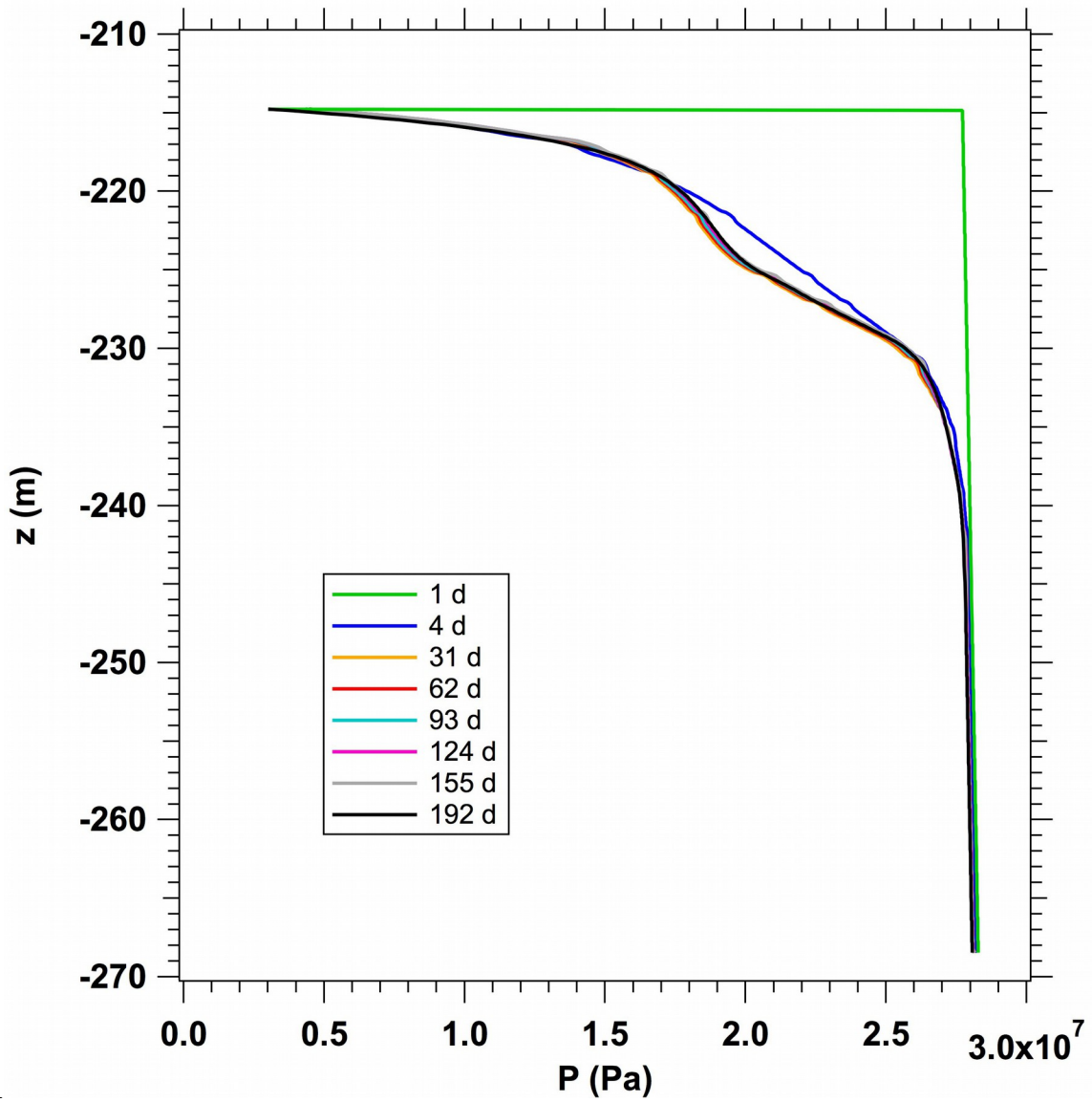
1101
1102
1103
1104**Figure 18.** Case R: Evolution of the pressure distribution with depth at the well during the long-term
1105production test at Site NGHP-02-09 of the KG Basin (P_w = 3 MPa). Note the lack of pressure response
1106below z = -240 m (from the ocean floor), where the thick, highly permeable aquifer horizon "Aqu09" begins.
1107
1108
1109

1110
1111
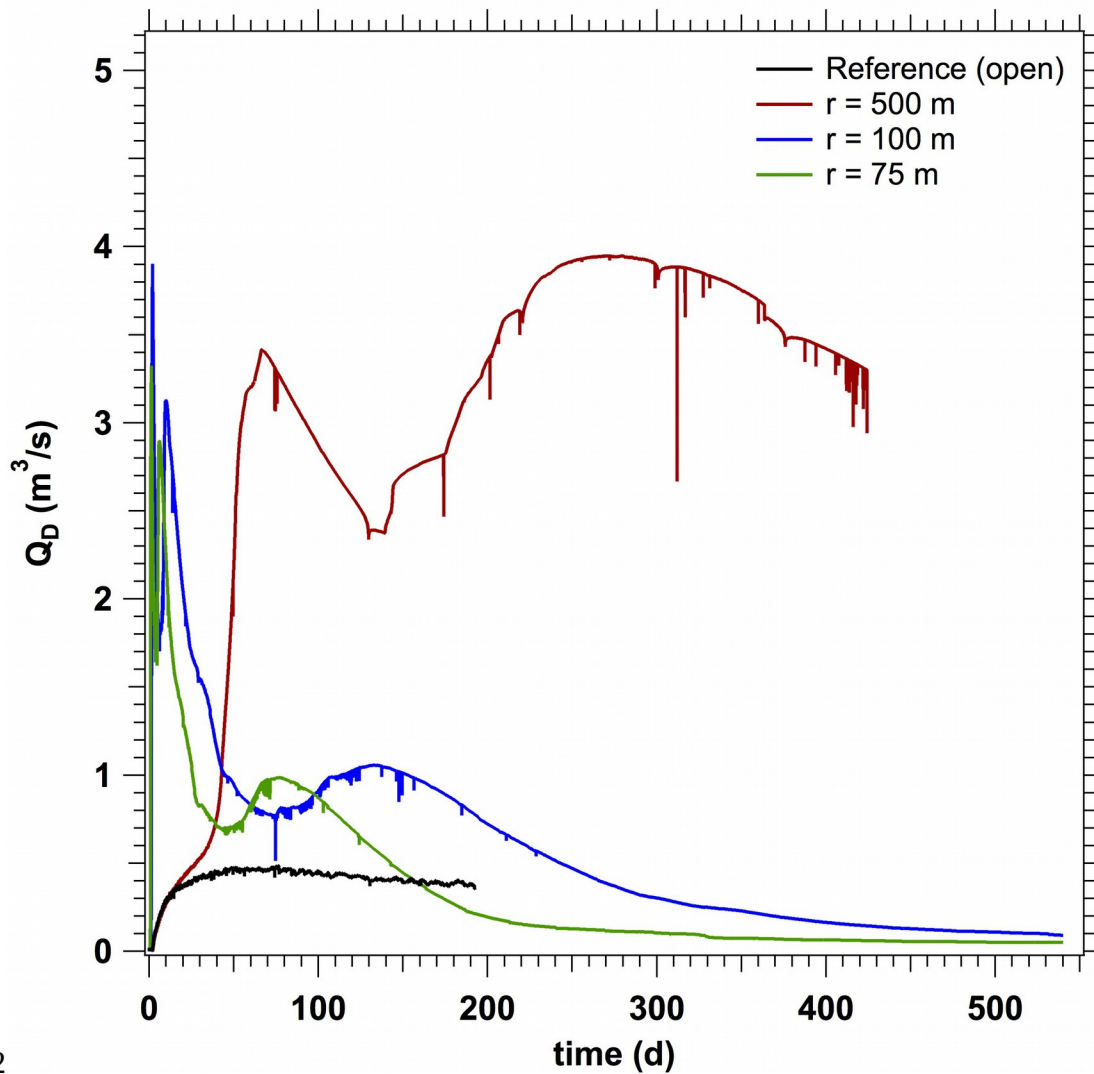
1112
1113
1114
1115
1116**Figure 19.** Cases C1, C2, C3 (closed systems): evolution of the rate of gas release from dissociation (Q_D)
1117over time during multi-well operations at Site NGHP-02-09 of the KG Basin. The Q_D for the reference Case R
1118(open system) is included for comparison.
1119
1120
1121

129

1122
1123
1124
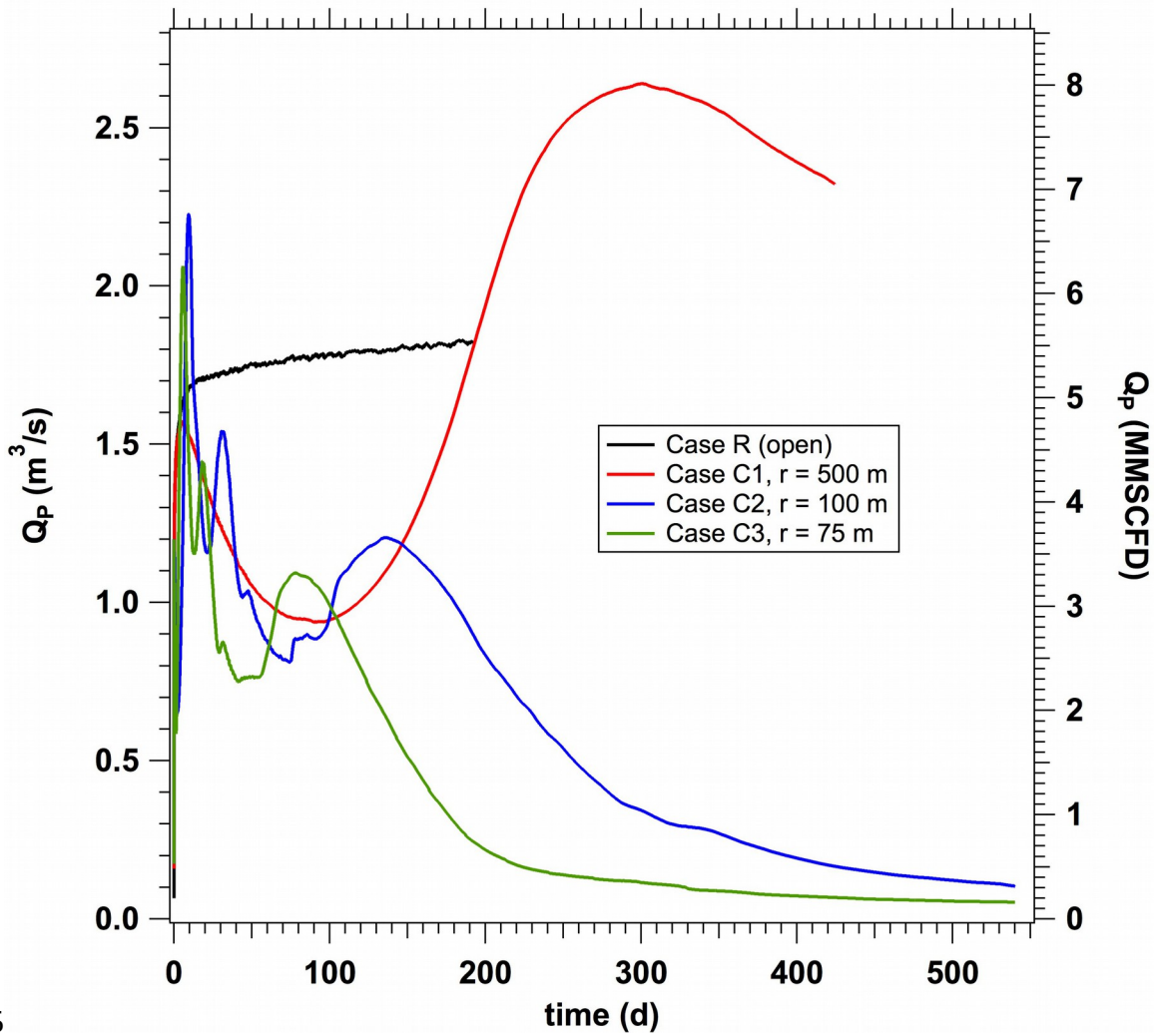
1125
1126
1127
1128**Figure 20.** Cases C1, C2, C3 (closed systems): evolution of the rate of gas production (Q_P) over time during
1129long-term multi-well operations at Site NGHP-02-09 of the KG Basin. The Q_P for the reference Case R (open
1130system) is included for comparison.
1131
1132
1133

130   133
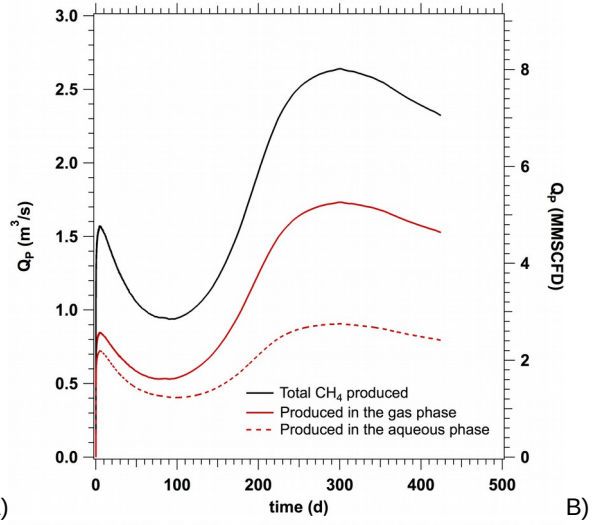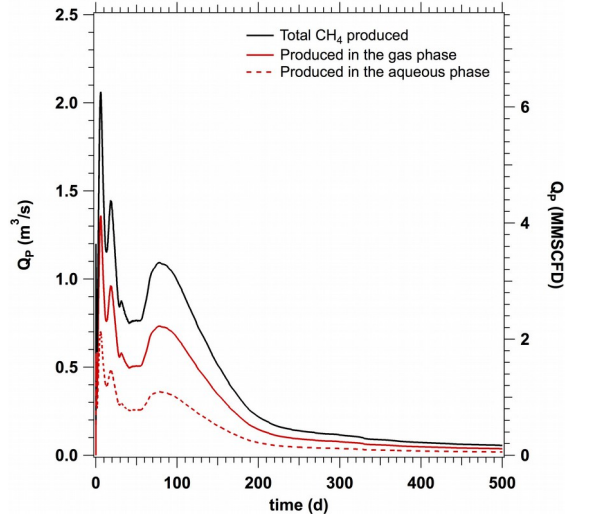
1135
1136
1137**Figure 21.** Provenance of gas in the production rate Q_P in Case C1 (A) and Case C3 (B).
1138
1139

133

1140
1141
1142
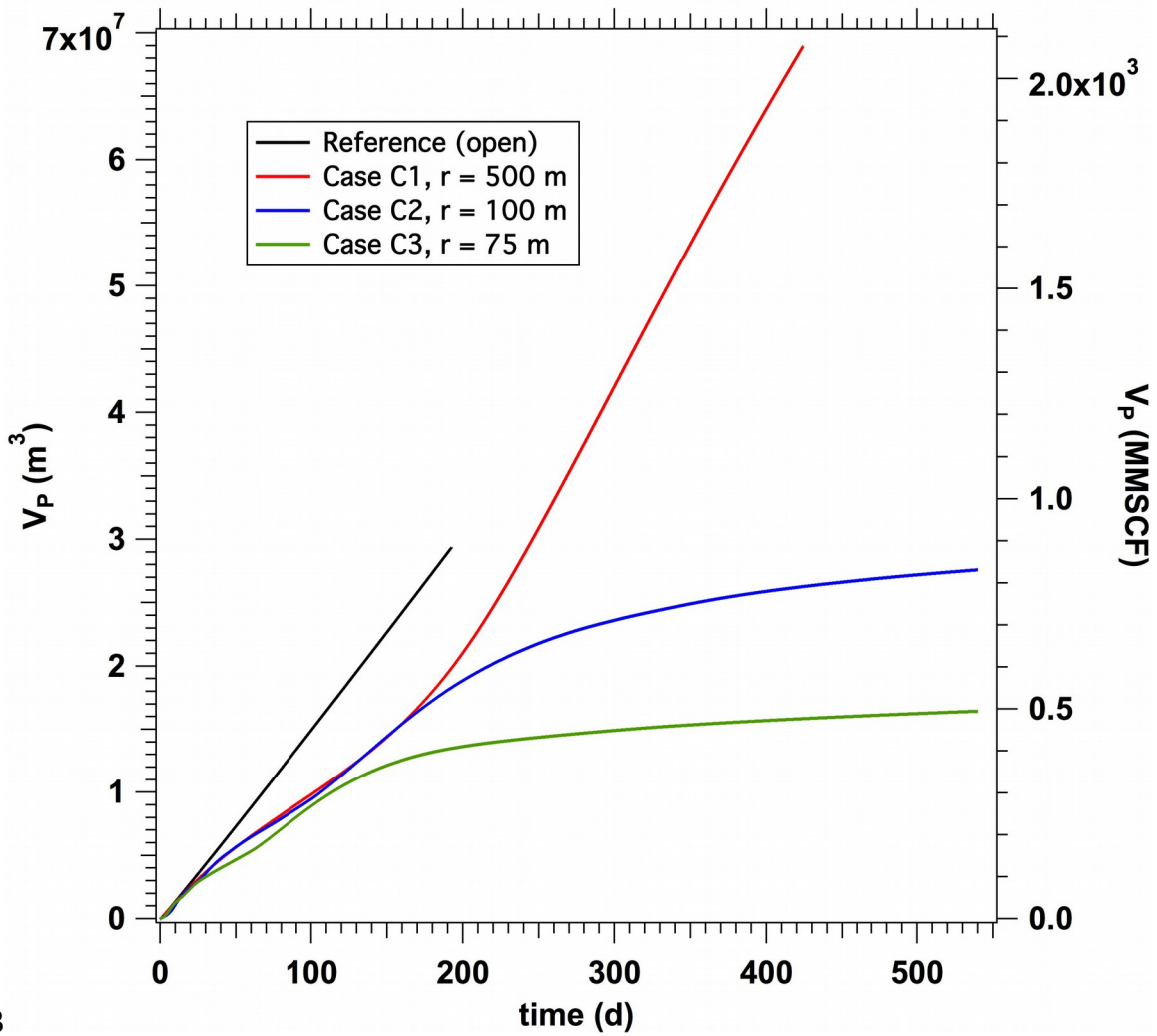
Figure 22. Cases C1, C2, C3 (closed systems): evolution of the volume of produced gas (V_P) over time during multi-well operations at Site NGHP-02-09 of the KG Basin. The V_P for the reference Case R (open system) is included for comparison.

1143
1144
1145
1146
1147
1148
1149
1150
1151

1152
1153
1154
1155
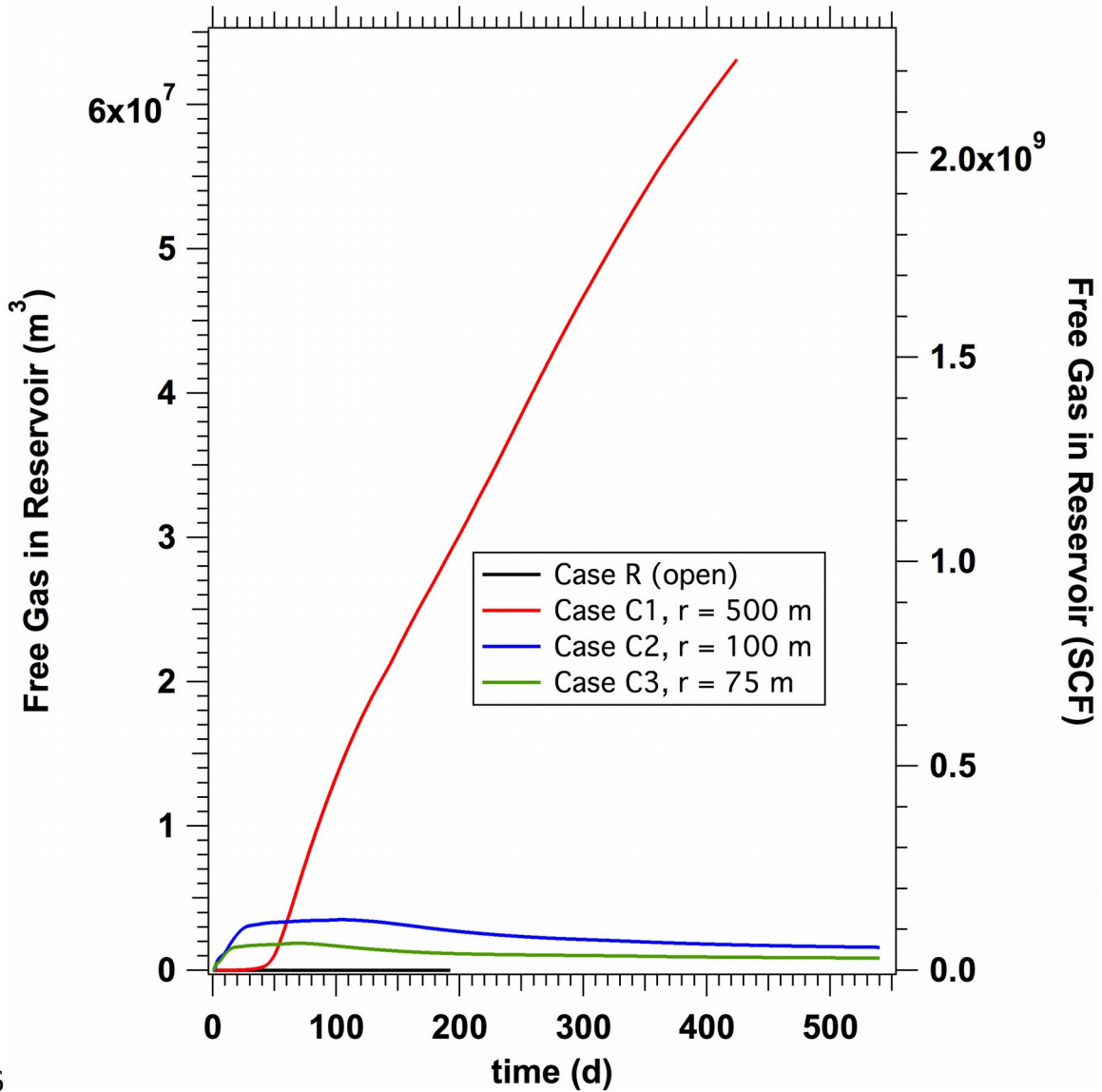
1157
1158**Figure 23.** Cases C1, C2, C3 (closed systems): evolution of the volume of free gas in the reservoir (V_F) over 1159time during multi-well operations at Site NGHP-02-09 of the KG Basin. The V_F for the reference Case R 1160(open system) that is included for comparison is significantly smaller than for any other case.
1161
1162
1163

1164
1165
1166
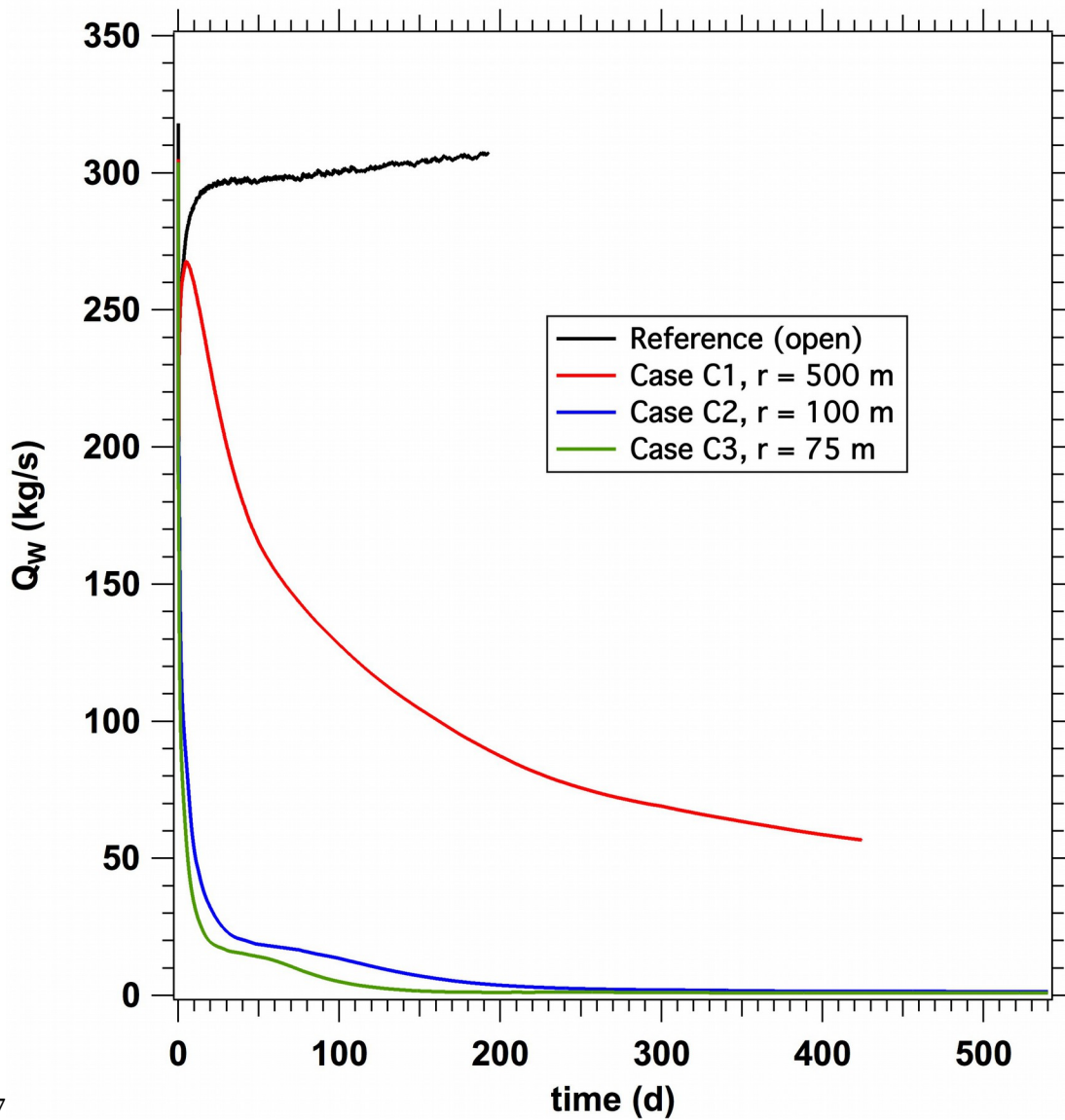
1167
1168
1169
1170**Figure 24.** Cases C1, C2, C3 (closed systems): evolution of the mass rate of water production (Q_w) over
1171time during multi-well operations at Site NGHP-02-09 of the KG Basin. The Q_w for the reference Case R
1172(open system) that is included for comparison has a distinctly different behavior.
1173
1174
1175

1176
1177
1178
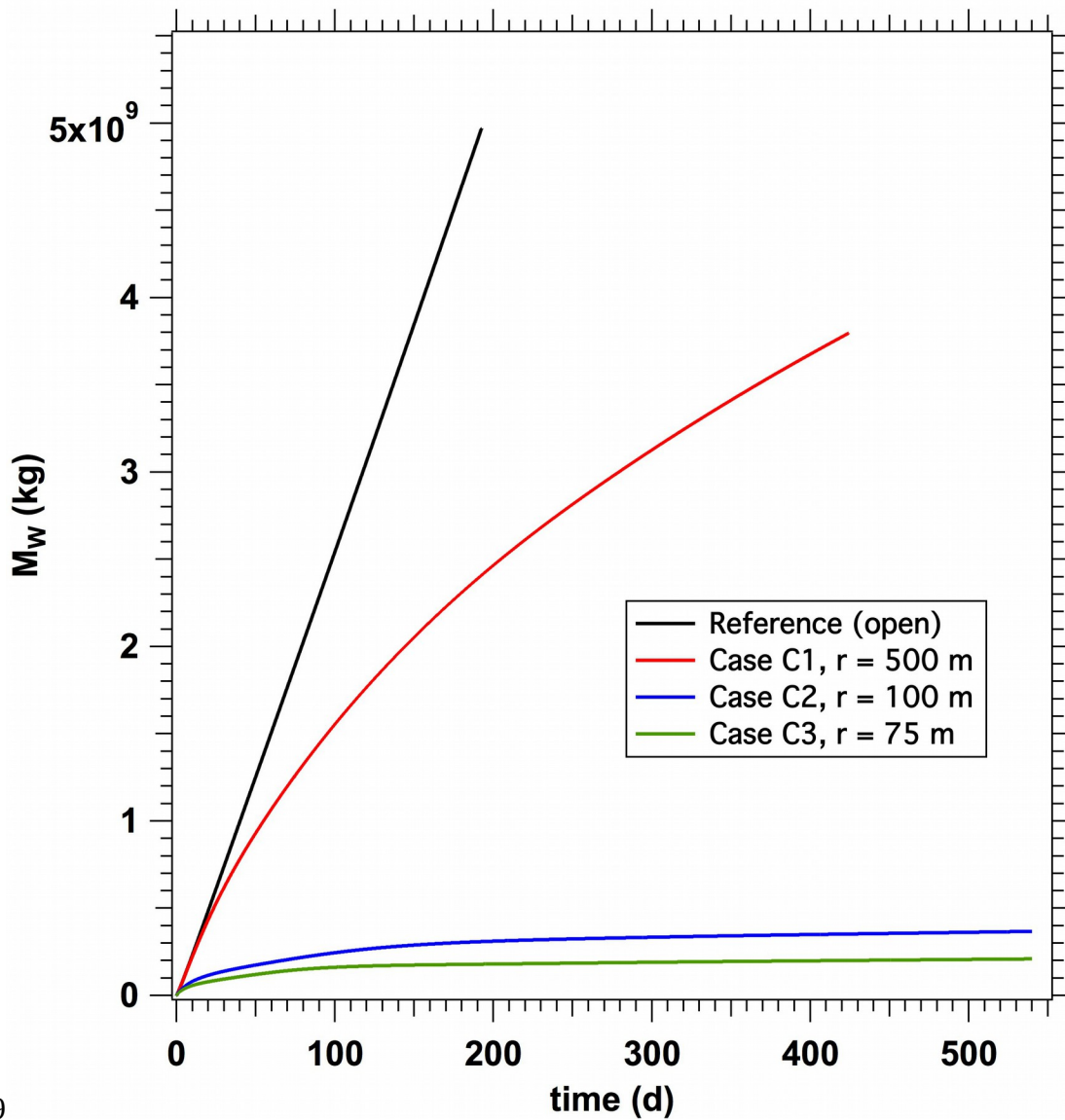
1179
1180
1181
1182**Figure 25.** Cases C1, C2, C3 (closed systems): evolution of the cumulative mass of produced water (M_w)
1183over time during multi-well operations at Site NGHP-02-09 of the KG Basin. The M_w for the reference Case
1184R (open system) that is included for comparison is significantly larger than in any other case.
1185
1186
1187

1188
1189
1190
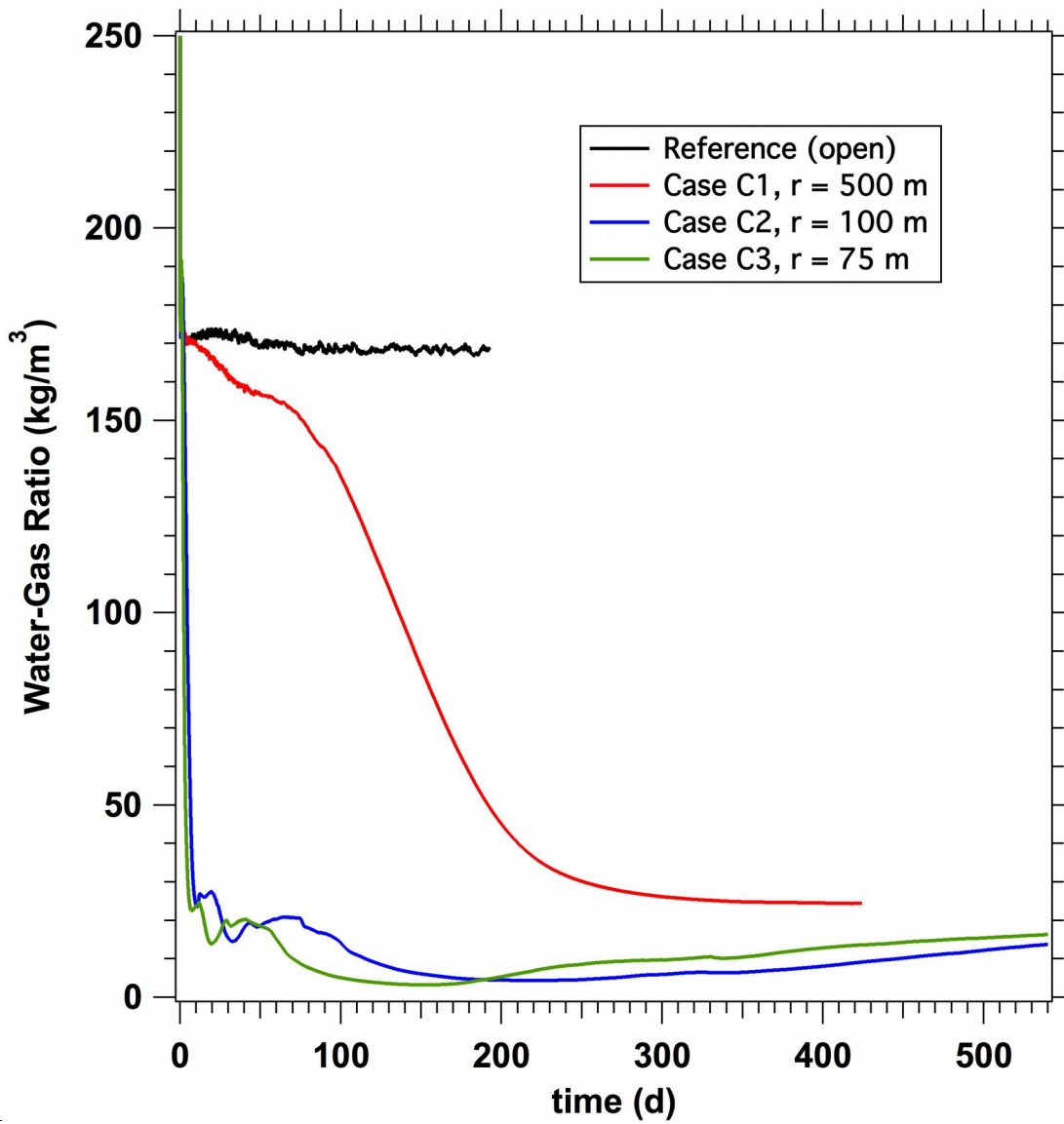
1191
1192
1193
Figure 26. Cases C1, C2, C3 (closed systems): evolution of the water-to-gas ratio (*WGR*) over time during multi-well operations at Site NGHP-02-09 of the KG Basin. Note the different behavior of the *WGR* for the reference Case R (open system) that is included for comparison.

1197
1198
1199

143

1200
1201
1202

3.6x10^{-2}

X$_s$ in produced water (wt%)

Case R (open)
Case C1, r = 500 m
Case C2, r = 100 m
Case C3, r = 75 m
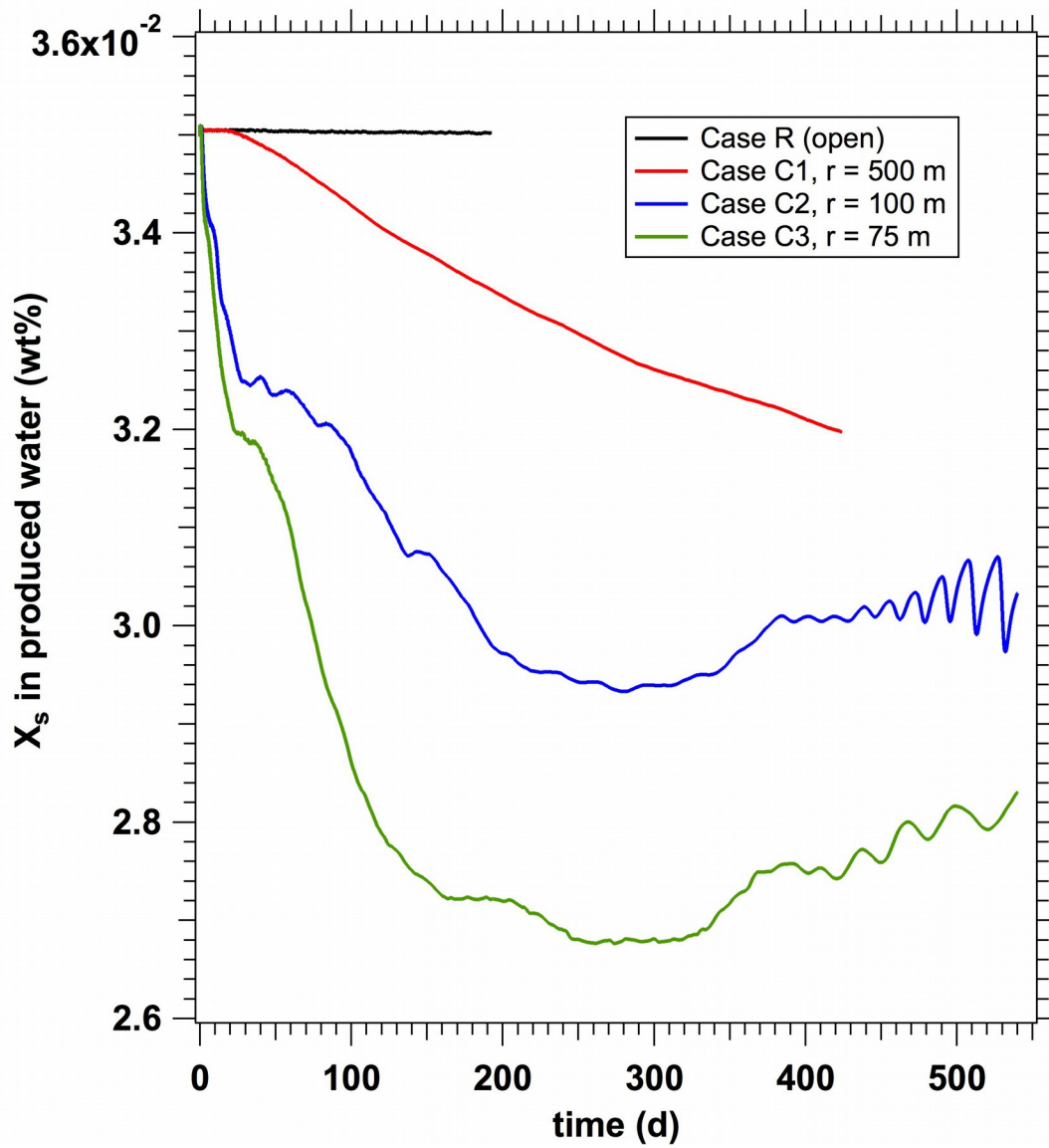
time (d)

1203
1204
1205
1206**Figure 27.** Cases C1, C2, C3 (closed system): evolution of the salt mass fraction in the produced water (X_S)
1207over time during multi-well operations at Site NGHP-02-09 of the KG Basin. Note the different behavior of
1208the X_S in the reference Case R (open system) that is included for comparison.
1209
1210
1211

144   140

1212
1213
1214
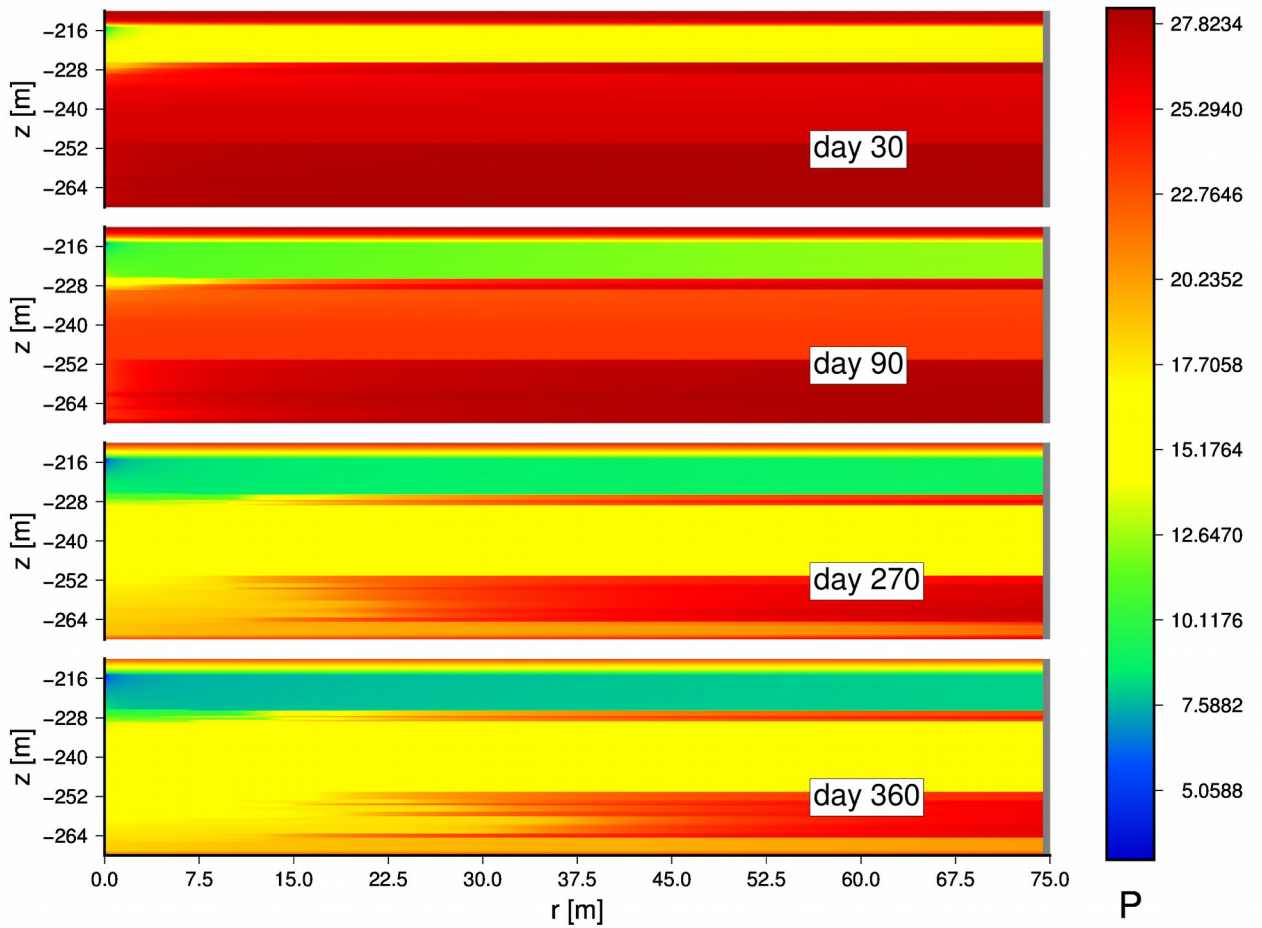
1215
1216
1217
1218**Figure 28.** Case C1: Evolution of pressure (in MPa) distribution in the system during multi-well production
1219operations at Site NGHP-02-09 of the KG Basin (P_w = 3 MPa).
1220
1221
1222

1223
1224
1225
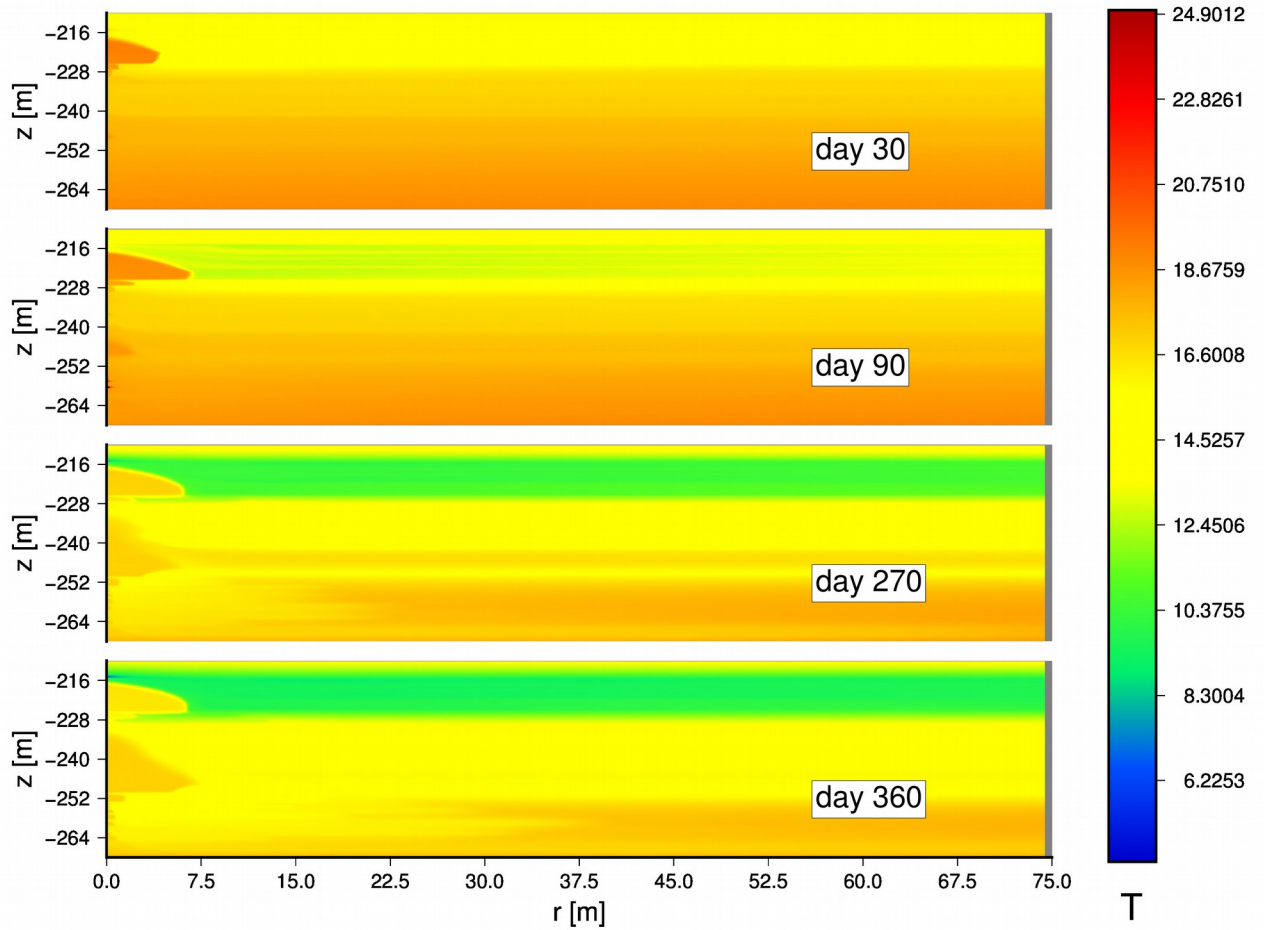
1226
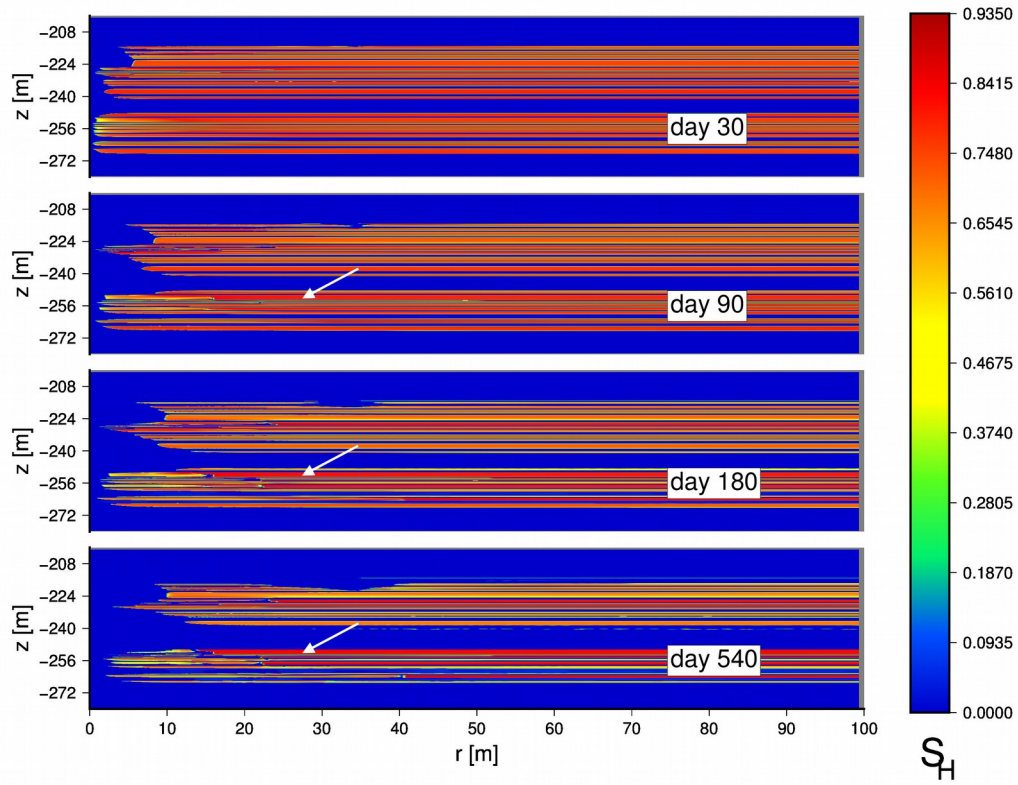1227
1228**Figure 29.** Case C1: Evolution of temperature (in °C) distribution in the system during multi-well production
1229operations at Site NGHP-02-09 of the KG Basin (P_w = 3 MPa).
1230
1231

1232
1233
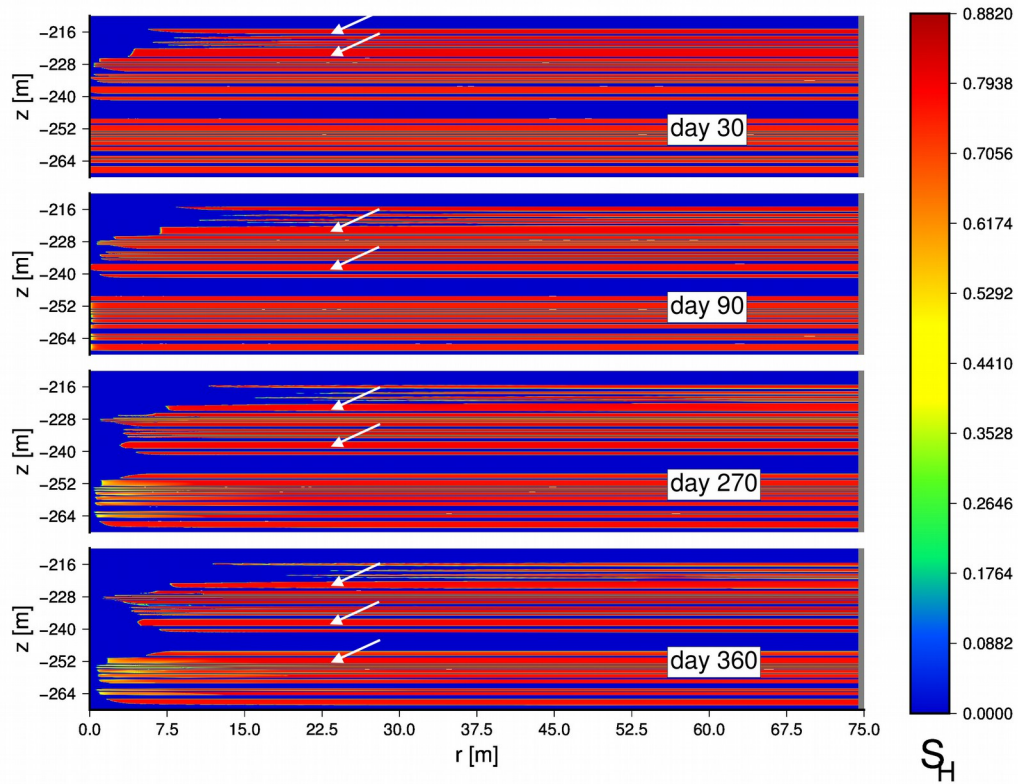
1234
1235
1236
1237**Figure 30.** Case C1: Evolution of the hydrate saturation S_H distribution in the system during multi-well 1238production operations at Site NGHP-02-09 of the KG Basin (P_w = 3 MPa). Arrows indicate hydrate layers 1239with S_H > 0.75.
1240
1241
1242

1243
1244
1245
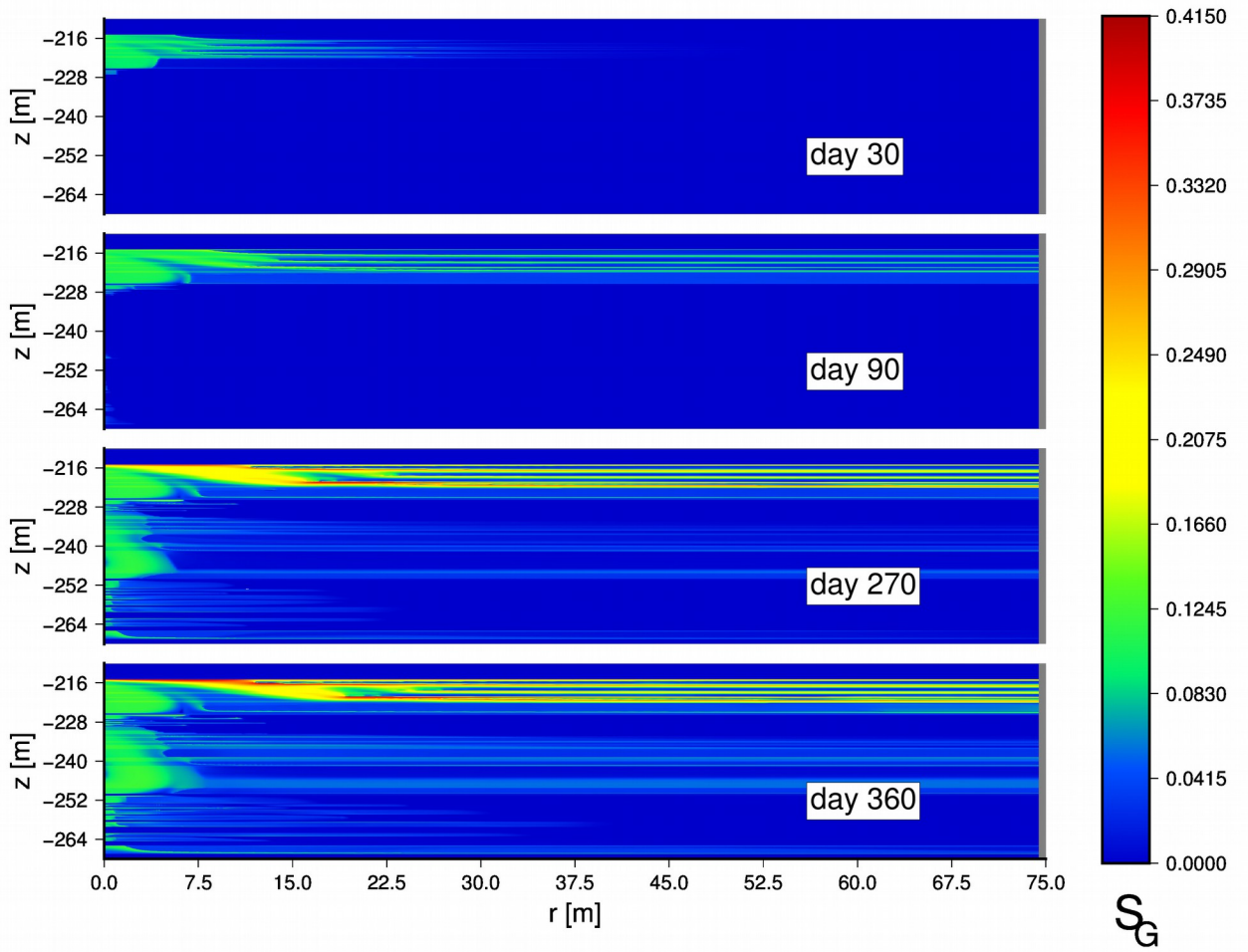
1246
1247
1248**Figure 31.** Case C1: Evolution of the gas saturation S_G distribution in the system during multi-well 1249production operations at Site NGHP-02-09 of the KG Basin (P_w = 3 MPa).

1250
1251
1252

1253
1254
1255
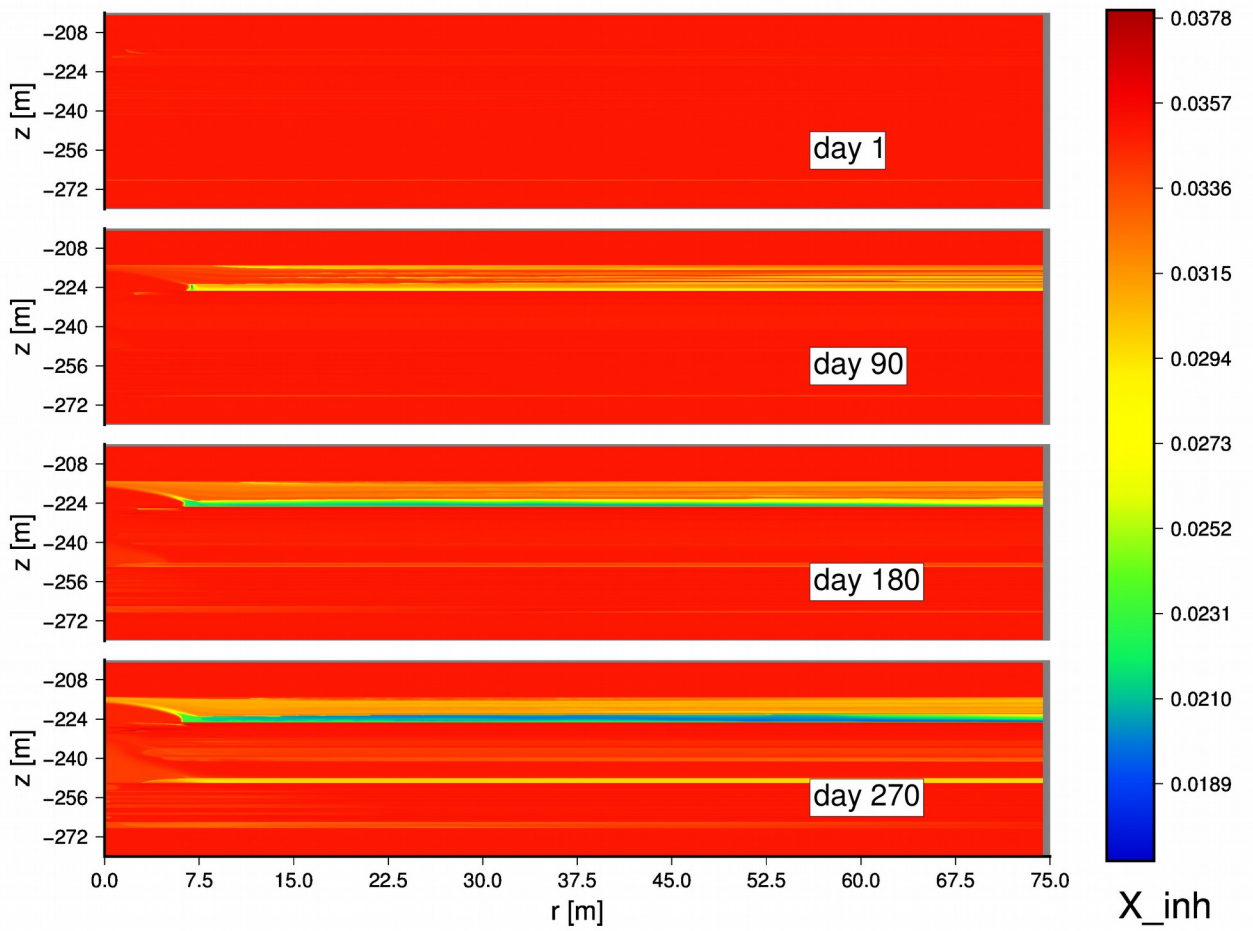
1257
1258**Figure 32.** Case C1: Evolution of the distribution of the salt mass fraction X_S in the aqueous phase of the 1259system during multi-well production operations at Site NGHP-02-09 of the KG Basin (P_w = 3 MPa).
1260

1261
1262
1263
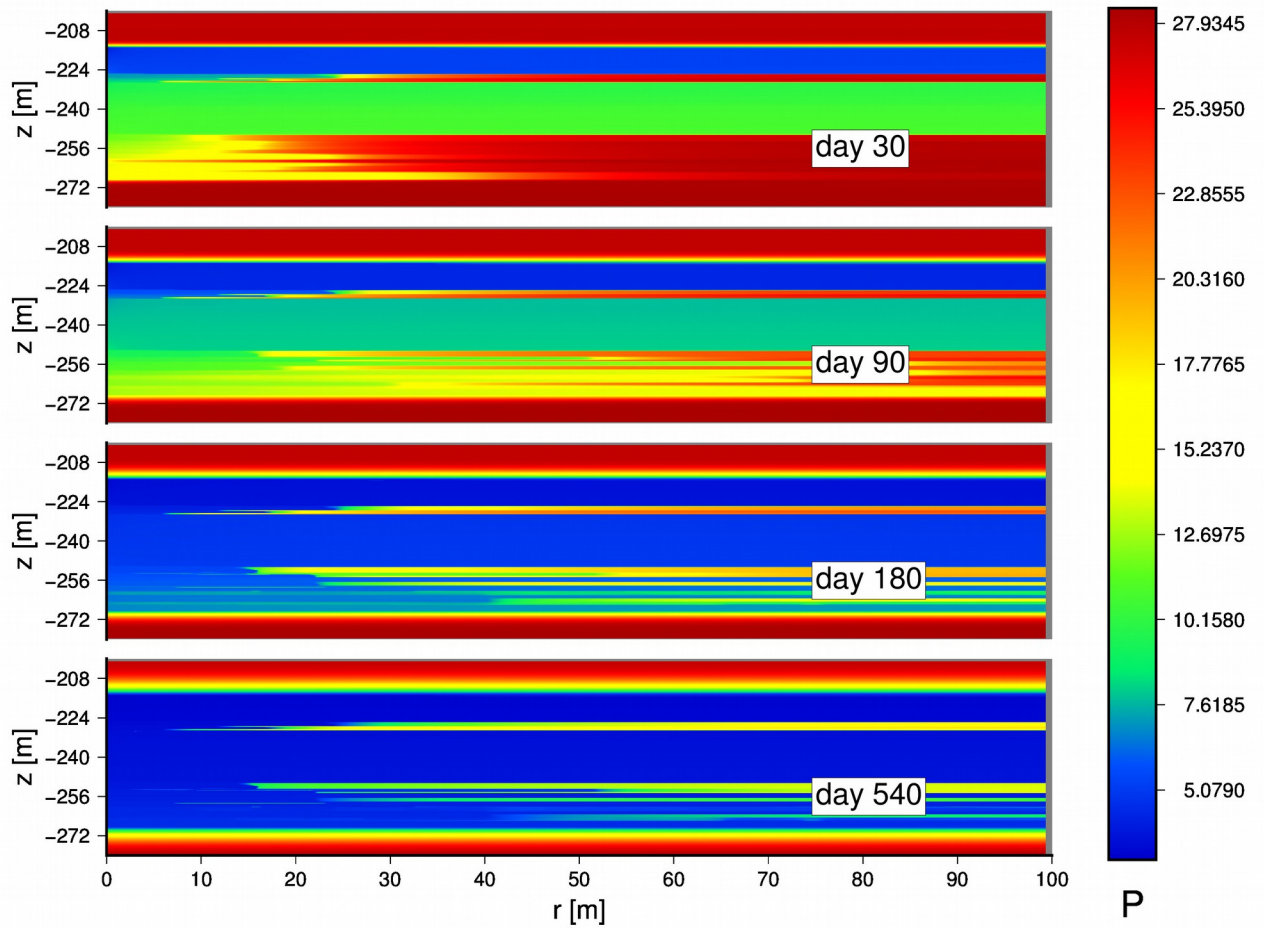
1264
1265

1266**Figure 33.** Case C2: Evolution of pressure (in MPa) distribution in the system during multi-well production
1267operations at Site NGHP-02-09 of the KG Basin (P_w = 3 MPa).

1268
1269
1270

1271
1272
1273
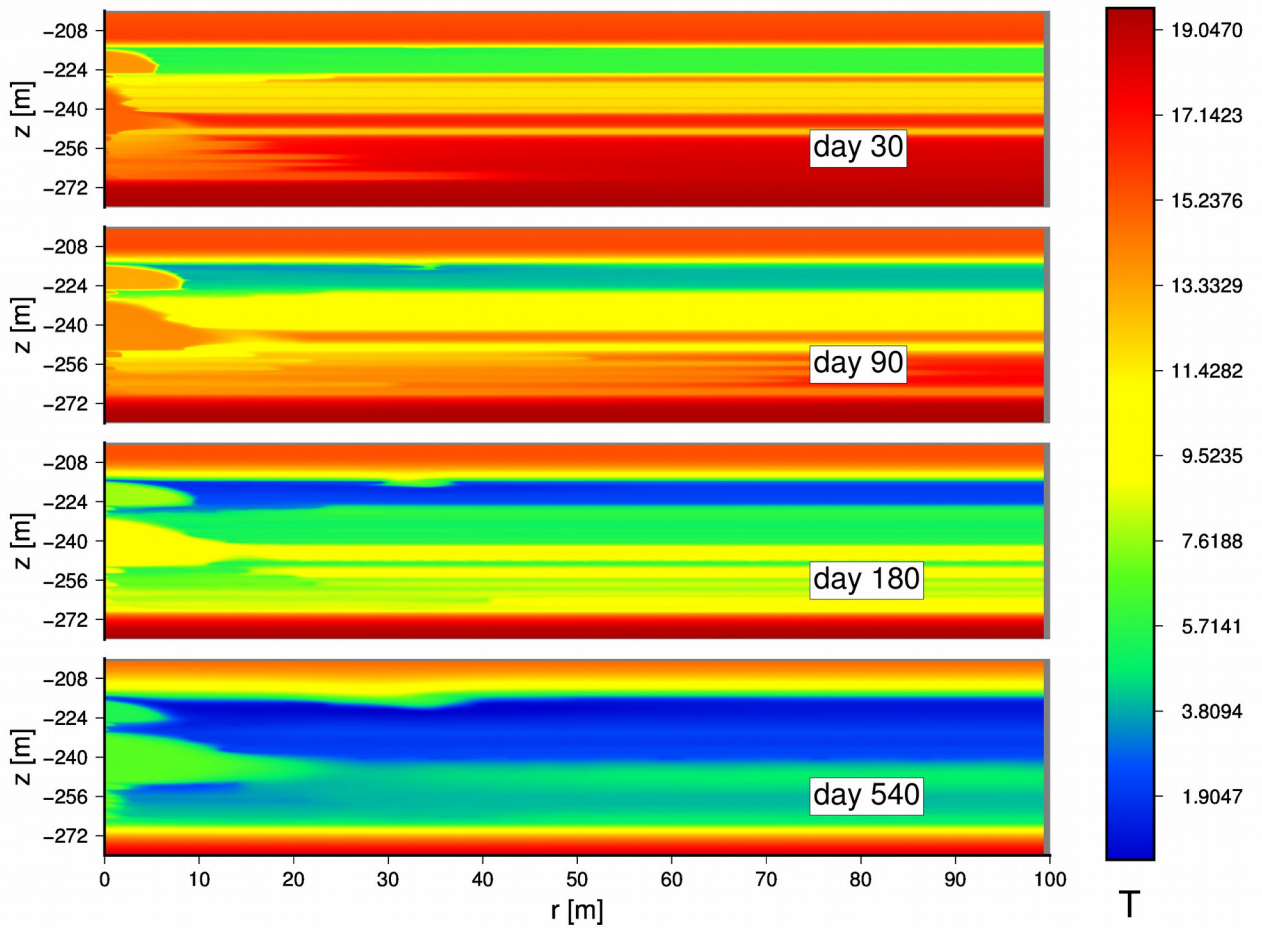
1274
1275
Figure 34. Case C2: Evolution of temperature (in ºC) distribution in the system during multi-well production operations at Site NGHP-02-09 of the KG Basin (P_w = 3 MPa).

1278
1279

1280
1281
1282

1283
1284
1285**Figure 35.** Case C2: Evolution of the hydrate saturation S_H distribution in the system during multi-well
1286production operations at Site NGHP-02-09 of the KG Basin (P_w = 3 MPa). Arrows indicate hydrate layers
1287with S_H > 0.75.

1288
1289
1290
1291

1292
1293
1294
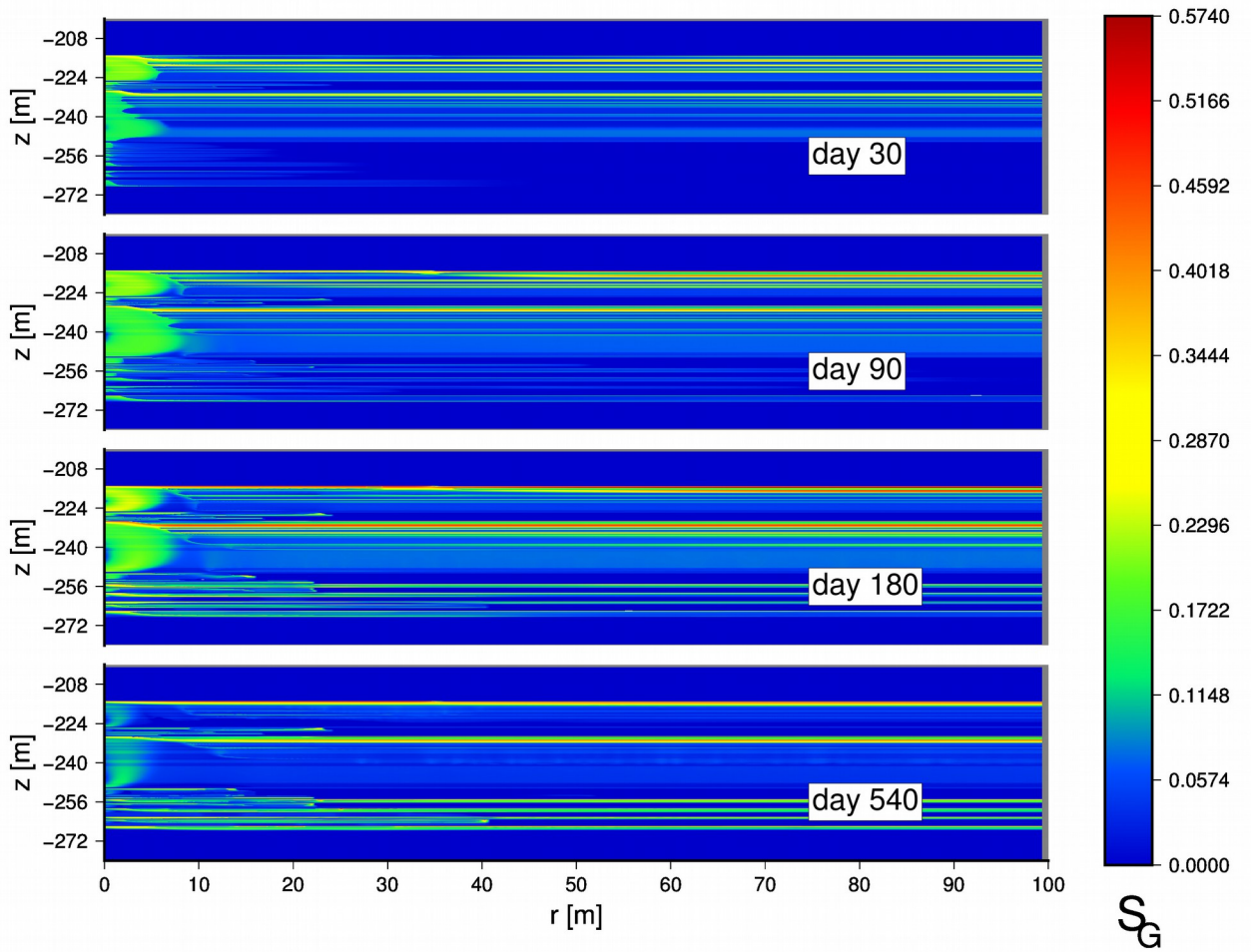
1295
1296
Figure 36. Case C2: Evolution of the gas saturation S_G distribution in the system during multi-well production operations at Site NGHP-02-09 of the KG Basin (P_w = 3 MPa).
1299
1300
1301

1302
1303
1304
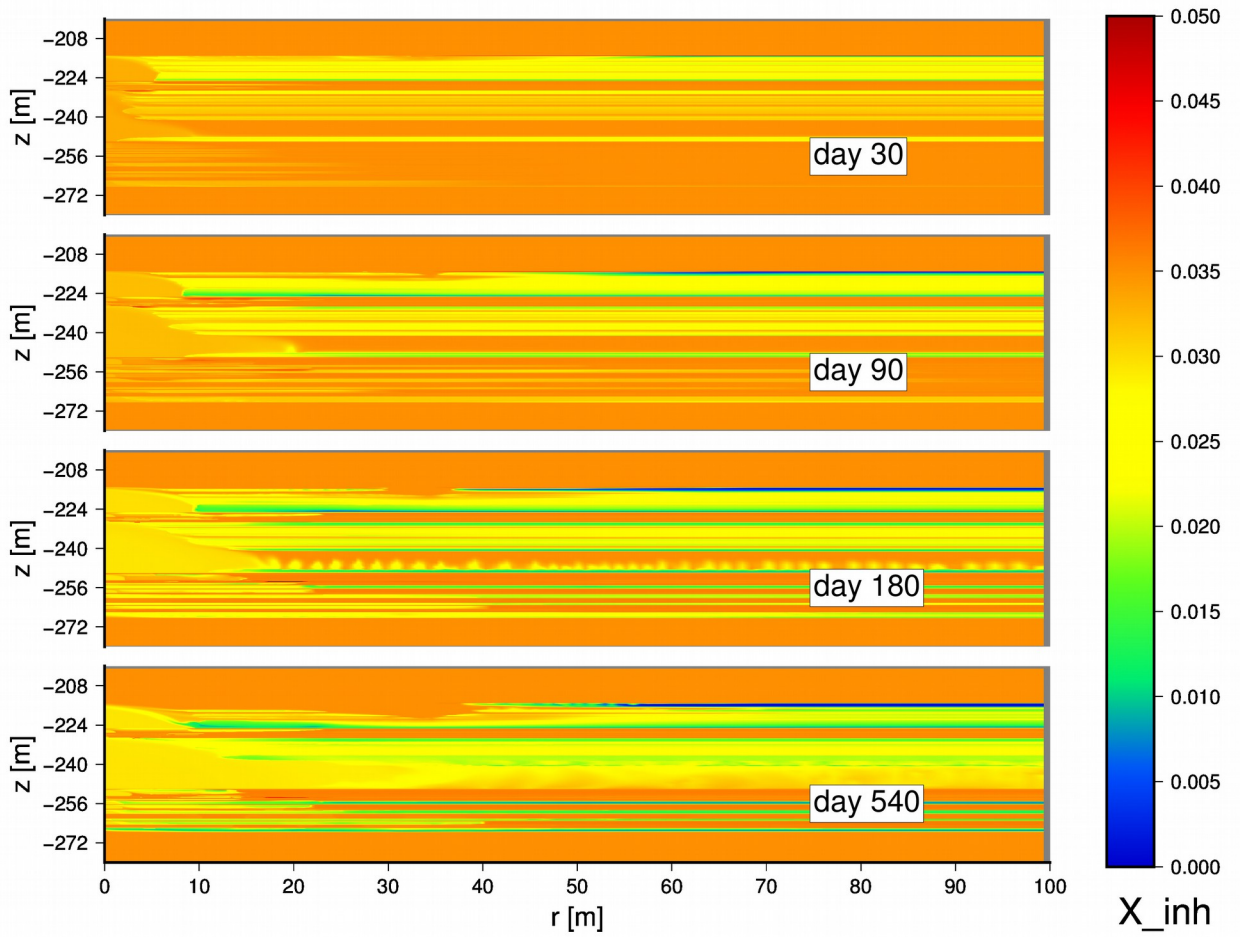
1305
1306
1307**Figure 37.** Case C2: Evolution of the distribution of the salt mass fraction X_S in the aqueous phase of the
1308system during multi-well production operations at Site NGHP-02-09 of the KG Basin (P_w = 3 MPa).
1309

1310

1311
1312
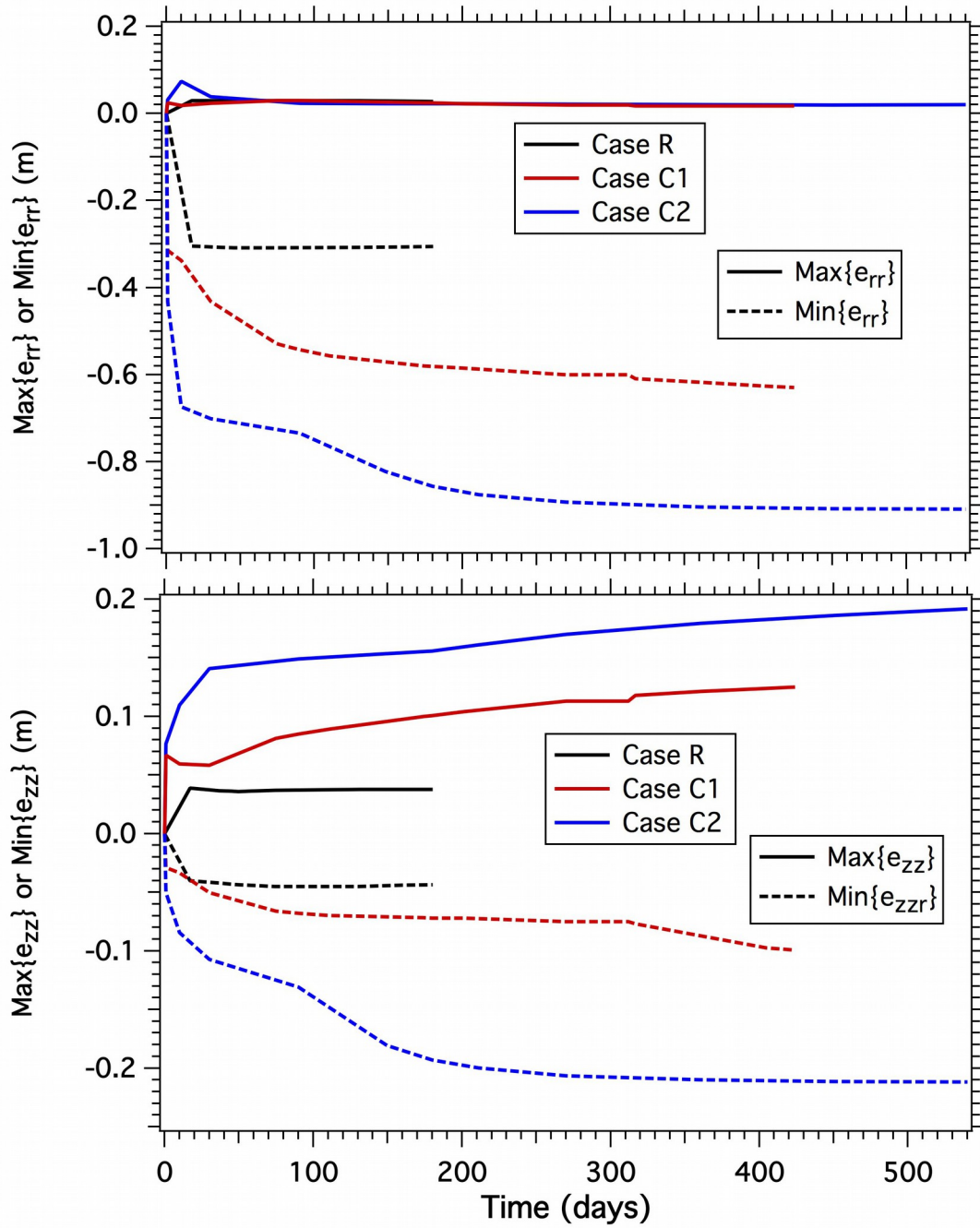
1314 **Figure 38.** Evolution of maximum and minimum strains ε_{zz} and ε_{rr} in the domain in Cases R, C1 and C2.
1315
1316

1317
1318
1319
1320
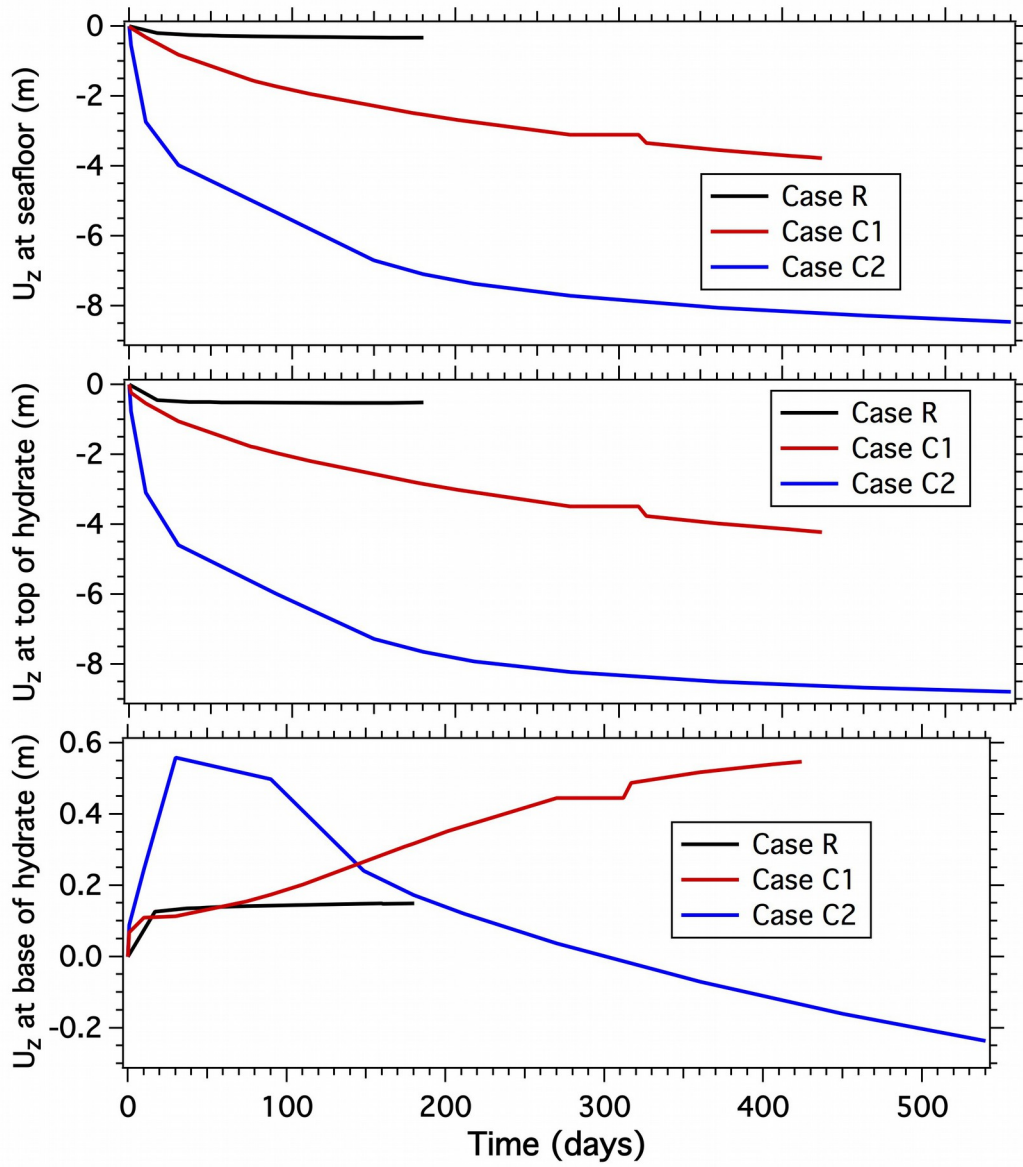
1321
1322**Figure 39.** Evolution of displacements u_z in the vicinity of the well in the domain in Cases R, C1 and C2.
1323
1324
1325
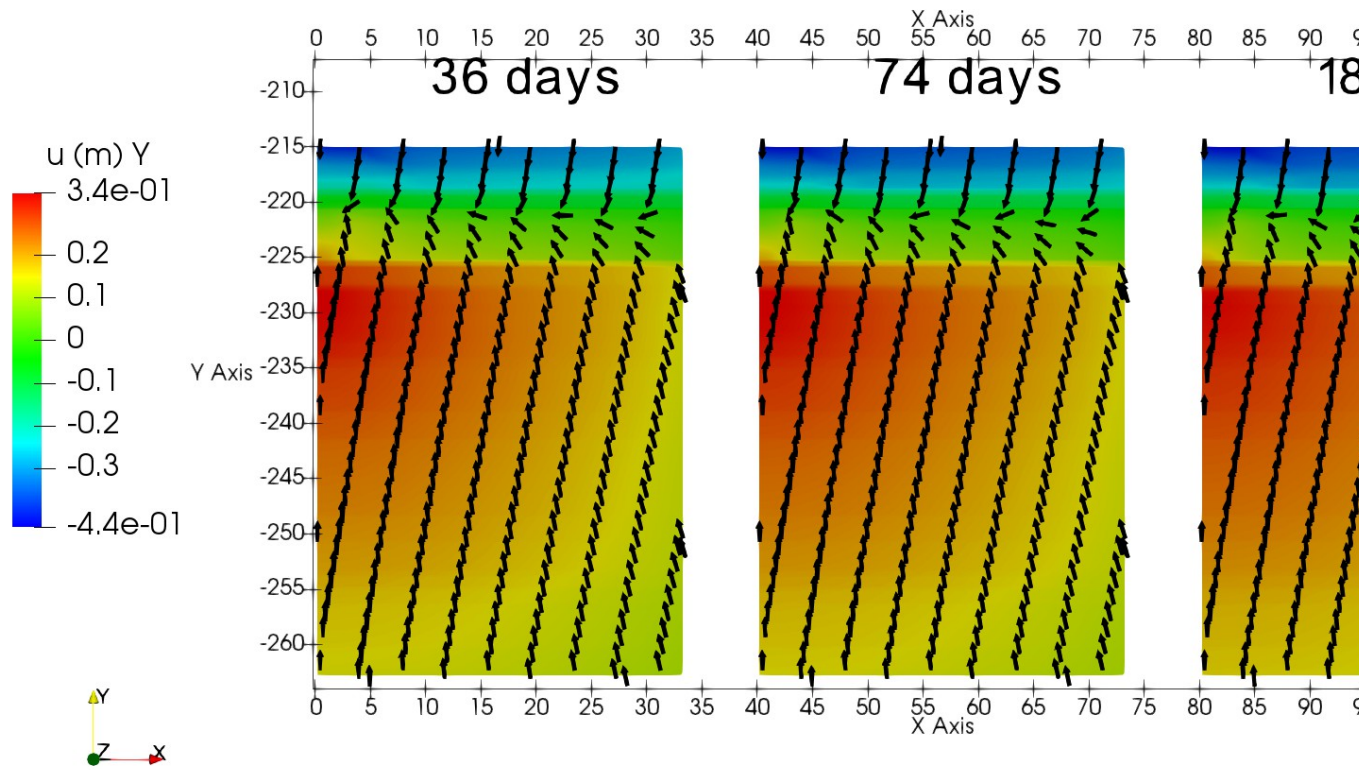
1326
1327Figure 40: Evolution of the z-displacements (u_z) in Case R (open system). The arrows show the direction of
1328the displacement. The z-coordinate (Y in the labels due to the rendering software) represents elevation in
1329meters measured from the ocean floor and the x-coordinate represents the distance from the well. The two
1330right images are offset by 40m and 80 m, respectively.
1331
1332
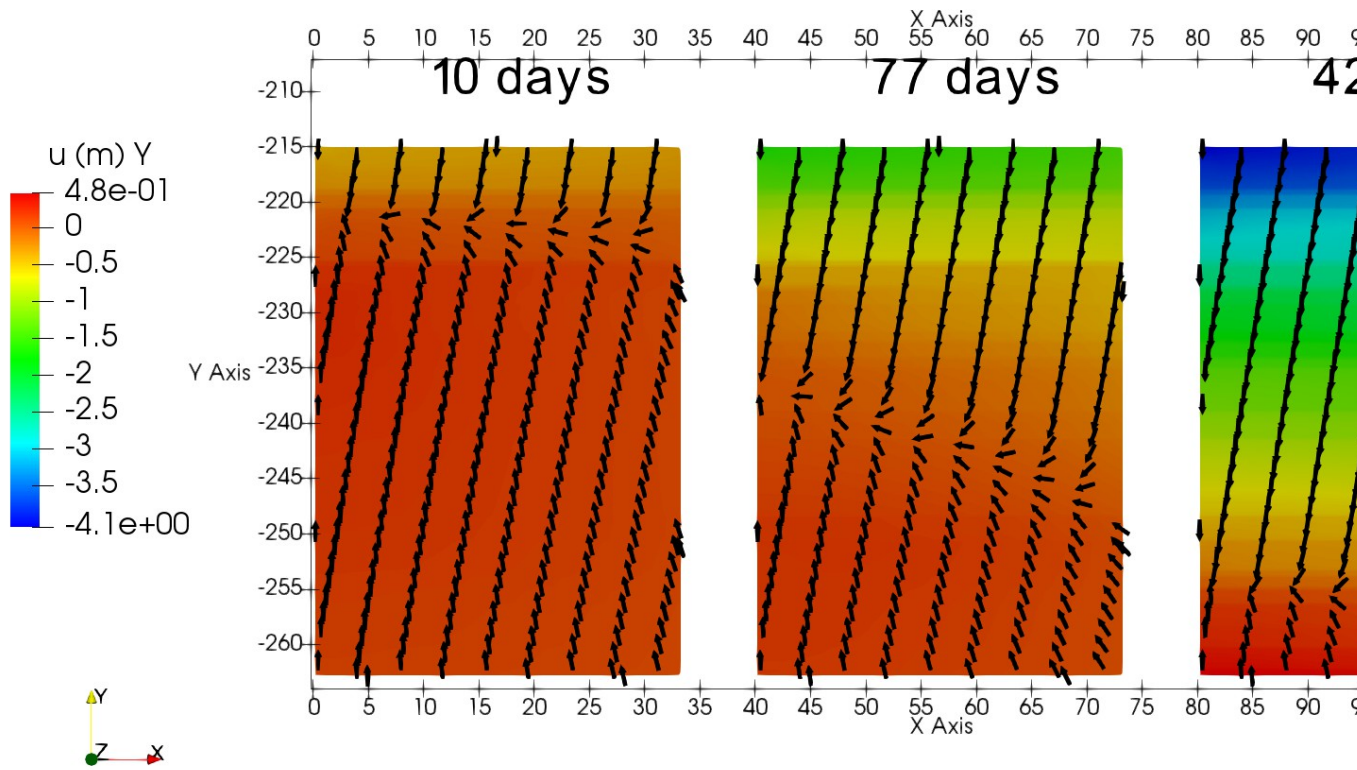
Figure 41: Evolution of the z-displacements (u_z) in Case C1 (closed system, r = 500m). The arrows show the direction of the displacement. The z-coordinate (Y in the labels due to the rendering software) represents elevation in meters measured from the ocean floor and the x-coordinate represents the distance from the well. The two right images are offset by 40m and 80 m, respectively.

1342 Figure 42: Evolution of the z-displacements (u_z) in Case C2 (closed system, r = 100m). The arrows show
1343 the direction of the displacement. The z-coordinate (Y in the labels due to the rendering software) represents
1344 elevation in meters measured from the ocean floor and the x-coordinate represents the distance from the
1345 well. The two right images are offset by 40m and 80 m, respectively.
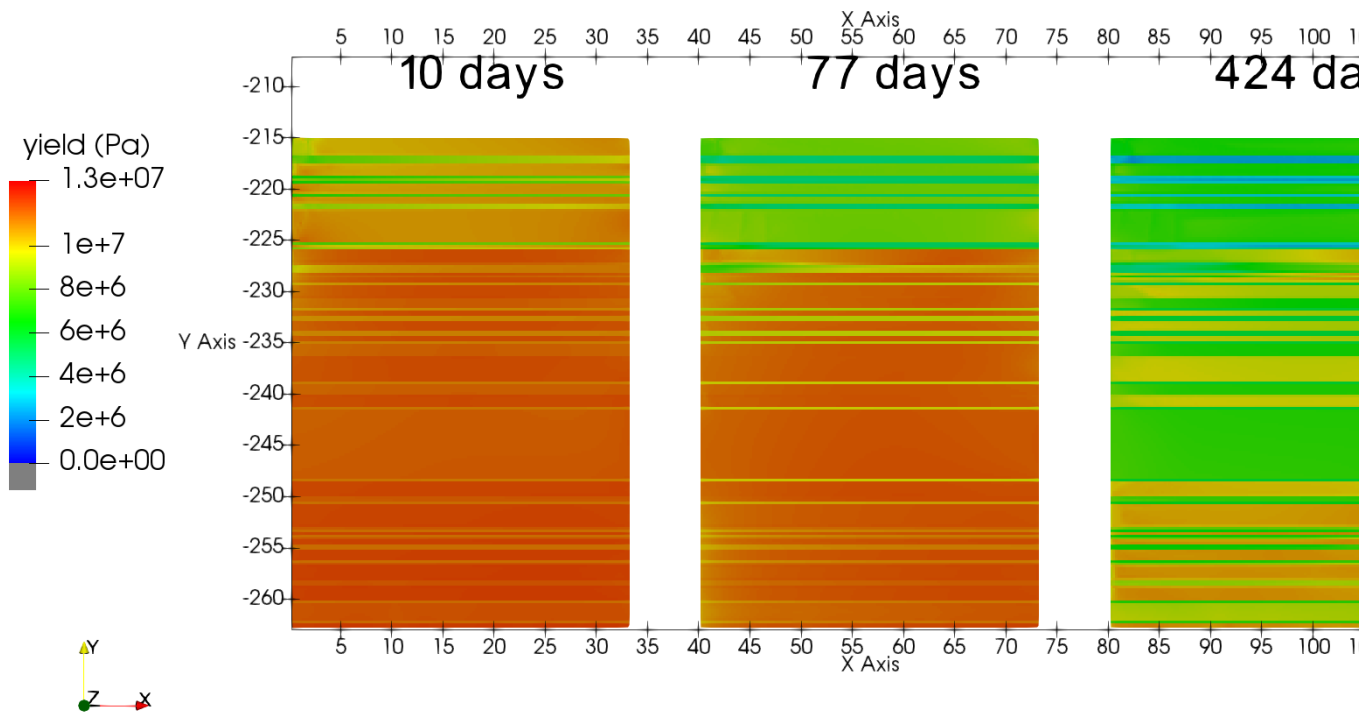
1346
1347
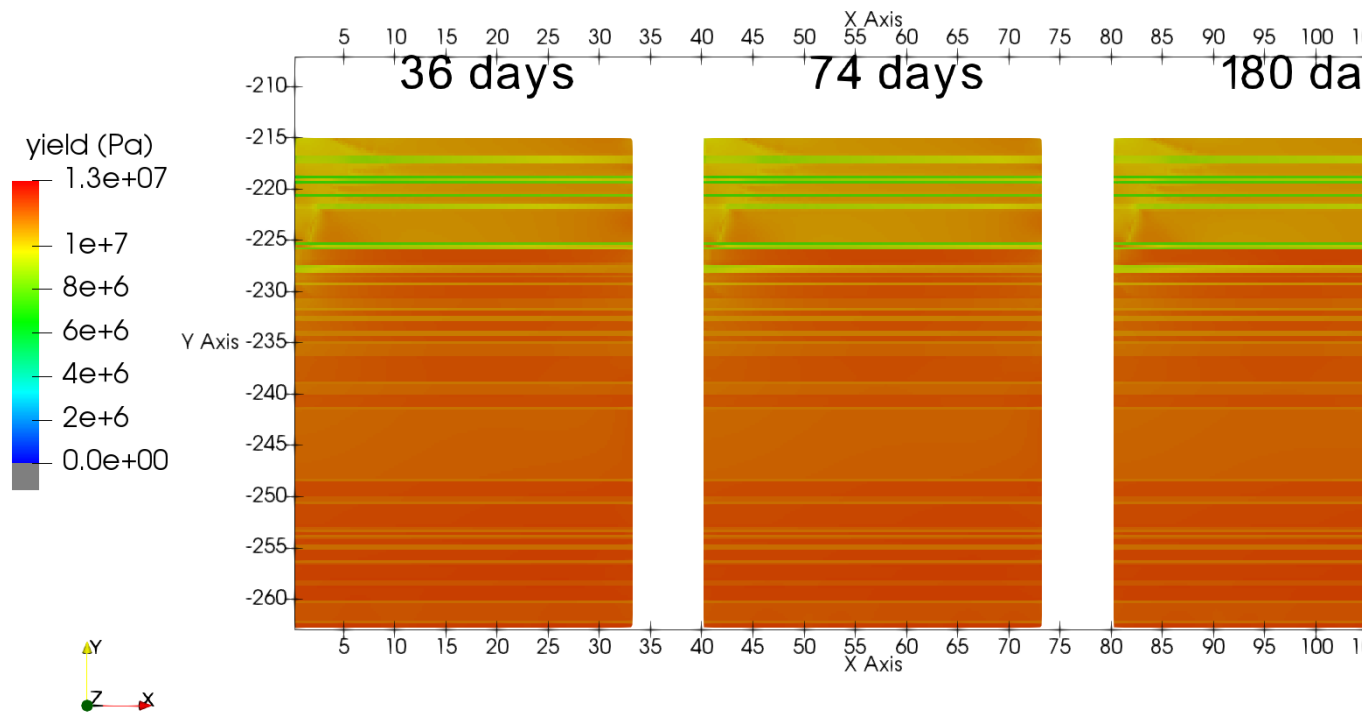
Figure 43: Evolution of the Drucker Prager yield criterion in Case R (open system). The z-coordinate (Y in the labels due to the rendering software) represents elevation in meters measured from the ocean floor and the x-coordinate represents the distance from the well. The two right images are offset by 40m and 80 m, respectively.
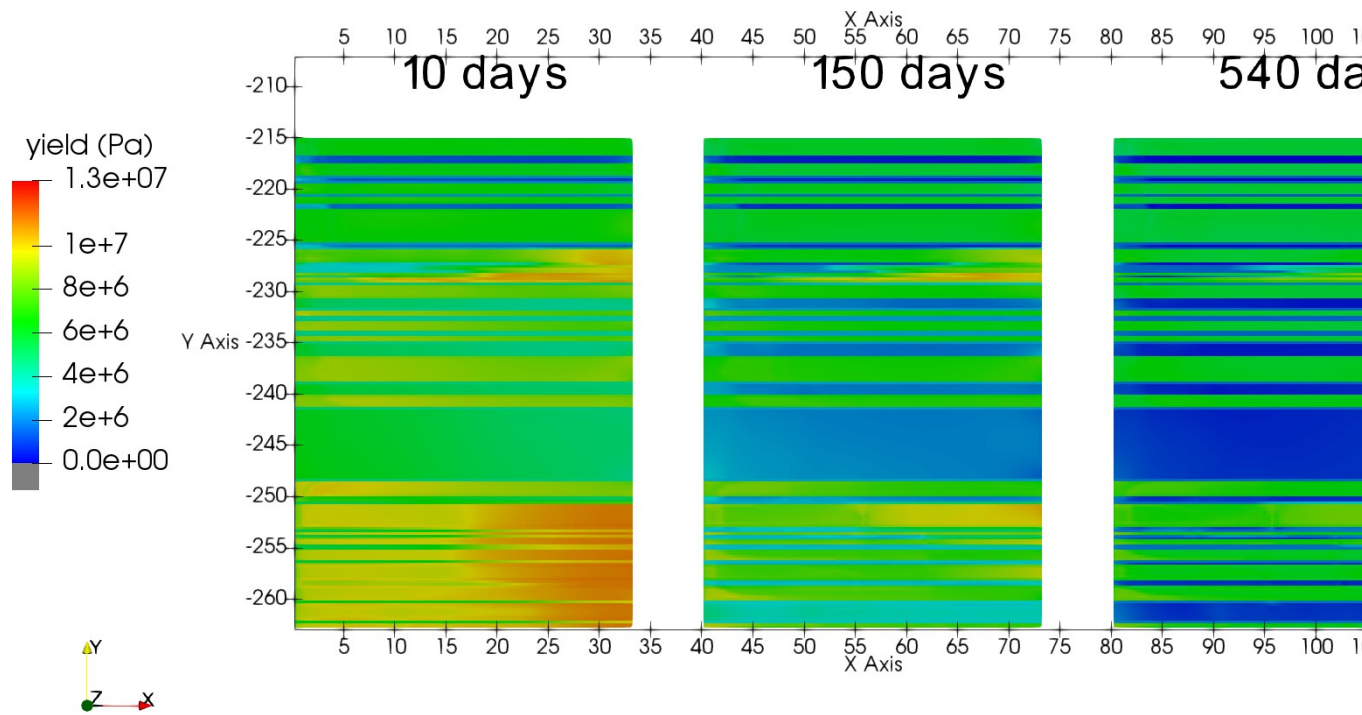
1355
1356Figure 44: Evolution of the Drucker Prager yield criterion in Case C1 (closed system, r = 500m). The z-
1357coordinate (Y in the labels due to the rendering software) represents elevation in meters measured from the
1358ocean floor and the x-coordinate represents the distance from the well. The two right images are offset by
135940m and 80 m, respectively.
1360
1361
1362

6

1363
1364Figure 45: Evolution of the Drucker Prager yield criterion in Case C2 (closed system, r = 100m). The z-
1365coordinate (Y in the labels due to the rendering software) represents elevation in meters measured from the
1366ocean floor and the x-coordinate represents the distance from the well. The two right images are offset by
136740m and 80 m, respectively. In this case, by the end of the simulated production time the yield criterion goes
1368below zero in the region encircled in red and colored by gray in the color range.

1369
1370
1371
1372
1373